

**INFLUENCE OF SUBSTITUTIONS AND  
SINTERING AIDS ON STRUCTURAL AND  
ELECTROMAGNETIC PROPERTIES OF  
NiCuZn FERRITE**

A Thesis Submitted in Partial Fulfillment of the  
Requirements for the Degree of

**DOCTOR OF PHILOSOPHY**

by

**PRADIP KUMAR ROY  
(Roll No: 50408004)**

Supervisor:  
**Dr. JAPES BERA**



**DEPARTMENT OF CERAMIC ENGINEERING  
NATIONAL INSTITUTE OF TECHNOLOGY,  
ROURKELA, ORISSA  
JANUARY, 2009**

DEDICATED TO MY PARENTS:

*Mr. Bechu Ram Roy*



*Mrs. Mira Roy*



NATIONAL INSTITUTE OF TECHNOLOGY  
ROURKELA, INDIA

---

**Dr. Japes Bera**  
Asst. Professor,  
Department of Ceramic Engineering,  
N. I. T. Rourkela,  
Rourkela- 769008, Orissa, India

Date: 12.01.2009

**CERTIFICATE**

This is to certify that the thesis entitled “**Influence of substitutions and sintering aids on structural and electromagnetic properties of NiCuZn ferrite**” being submitted by Mr. Pradip Kumar Roy for the degree of Doctor of Philosophy in Engineering from N. I.T. Rourkela, is a record of bonafied research work carried out by him under my supervision at Department of Ceramic Engineering. In my opinion, this is a fit piece of work for submission for the degree of Doctor of Philosophy. To the best of our knowledge, the work has not been submitted to any other University or Institute for the award of any degree or diploma.

(Dr. J. Bera)

Asst. Professor,  
Department of Ceramic Engineering,  
N. I. T. Rourkela, Rourkela- 769008.

Mail Id: [jbera@nitrkl.ac.in](mailto:jbera@nitrkl.ac.in), [jbera@rediffmail.com](mailto:jbera@rediffmail.com), [japesb@gmail.com](mailto:japesb@gmail.com)

Phone No: +91-661-2462204 (O), +91-661-2463204 (R), +91-9437246159 (M)

## *ACKNOWLEDGEMENTS*

---

With deep regards and profound respect, I avail this opportunity to express my deep sense of gratitude and indebtedness to Prof. Japes Bera, Department of Ceramic Engineering, N. I. T. Rourkela, for introducing the present research topic and for inspiring guidance, constructive criticism and valuable suggestion throughout this research work. It would have not been possible for me to bring out this thesis without his help and constant encouragement. I wish that he will keep in touch with me in future and will continue to give his valuable advice.

I would like to express my gratitude to Prof. Santanu Bhattacharyya, Head of Ceramic Engineering Department, for his cooperation in one way or the other. I wish to record my thanks and gratitude to him for his valuable suggestions and encouragements at various stages of the work.

I am also grateful to Prof. S. K. Pratihari, Department of Ceramic Engineering, whose vast knowledge in the field of science and technology has enlightened me in different areas of this experimental research work. His deep sense of appreciation and dedication to research has been a constant source of inspiration to me.

I sincerely thank to Prof. S. Ghosh of Electrical Engineering Department and Prof. S. Adak of Ceramic Engineering Department for their useful suggestions and help whenever I had asked for it. I am grateful to Prof. B. B. Nayak, Mr. Santanu Behera and Prof. S. Pal of Ceramic Engineering Department for their help to carry out my research work.

It was a nice and memorable association with all the staff of my department. I wish to give them my heartfelt thanks for their constant help.

My special thanks go to few of my endless list of friends, Rana, Kiran, Yogo, Sarat, Arundhati, Madhumita Didi and Parnashree Didi for helping me a lot in every stage of thesis preparation. I must recall my ever best friends Uttam, Abhiram, Gagandeep, Sudip, Santanu and Supriya, Dr. Rajendra Jaiswal. Their friendship is a blessing, my heart will always treasure. I would also like to thank to all my teachers and professors, from academic and nonacademic levels, who inspire me to be wise

and knowledge. I am truly indebted to all who have supported me and brought me so far.

I would like to thank my parents, sister (Nirupa Roy) and other family members, uncles, aunties, brothers for their support for choices in all my life and their love, which has been a constant source of strength for everything I do. I feel a deep sense of gratitude for my father, Mr. Bechu Ram Roy, and mother, Mrs. Mira Roy, who formed a part of my vision and taught me the good things that really matter in life.

I am thanking my beloved Subrata Da, Suhrit Mula Da, Soumya Da and their family for all the hope, true love, affection, caring, concern and constant encouragements. They give me many reasons to smile everyday and to pursue my research work happily. I would like to thank their family members for giving me love and support.

I am happy to acknowledge Department of Science and Technology, New Delhi and N. I. T. Rourkela for sponsoring me.

Above all, I thank our saving Kali Mata for giving me all these people to help and encourage me, and for the skills and opportunity to complete this thesis.

Date: 12.01.2009

(Pradip Kumar Roy)

# ABSTRACT

---

NiCuZn ferrite is the most important magnetic materials used for the manufacturing of multilayer chip inductors. The present work is focused on the influence of substitutions and sintering aids on electromagnetic properties of NiCuZn ferrite.

(Ni<sub>0.8-x</sub>Cu<sub>0.2</sub>Zn<sub>x</sub>)Fe<sub>2</sub>O<sub>4</sub> ferrites with 0.45 ≤ x ≤ 0.60 compositions were studied to optimize Zn concentration. The effects of Mg<sup>2+</sup> substitution for Ni<sup>2+</sup> and La<sup>3+</sup>, Sm<sup>3+</sup> substitutions for Fe<sup>3+</sup> on the electromagnetic properties of optimized NiCuZn ferrite were investigated. The effects of sintering aids like V<sub>2</sub>O<sub>5</sub>, Bi<sub>2</sub>O<sub>3</sub> and MoO<sub>3</sub> on the densification kinetics and electromagnetic properties of the ferrite were also investigated.

Ferrite specimens were synthesized by nitrate-citrate sol-gel auto combustion process. Nanocrystalline ferrite powder was successfully synthesized by self propagating combustion method. The process resulted in the formation of nano-sized (19-22 nm), highly reactive (specific surface area- 40-50 m<sup>2</sup>/gm) and crystalline spinel ferrite powders. The ferrite powders also showed good sinterability at around <950°C.

On the basis of good permeability as well as resistivity, (Ni<sub>0.25</sub>Cu<sub>0.2</sub>Zn<sub>0.55</sub>)Fe<sub>2</sub>O<sub>4</sub> composition was optimized. The composition showed, initial permeability of about 111 and the resistivity of about 8.9 MΩ-cm at 100 kHz with frequency stability up to ~10 MHz.

An improved electromagnetic property of the Mg substituted ferrite was found in (Ni<sub>0.07</sub>Mg<sub>0.18</sub>Cu<sub>0.2</sub>Zn<sub>0.55</sub>)Fe<sub>2</sub>O<sub>4</sub> nominal composition. The initial permeability, saturation magnetization and resistivity were of about 2420, 85 emu/gm and 10 MΩ-cm at 100 kHz respectively in this composition. The improved electromagnetic properties of the composition might be due to the lowering of magnetostriction constant by Mg substitution and partly due to better densification.

La substitution in the ferrite mainly produced grain boundary secondary phase LaFeO<sub>3</sub>. However, bulk density and grain size of the ferrite increased with La

substitution up to 3.75 atom%. A significant increase in initial permeability ( $\sim 424$ ), saturation magnetization ( $\sim 66$  emu/gm) and resistivity ( $\sim 69$  M $\Omega$ -cm at 100 kHz) was found in  $(\text{Ni}_{0.25}\text{Cu}_{0.2}\text{Zn}_{0.55})\text{La}_{0.025}\text{Fe}_{1.975}\text{O}_4$  composition. The increased permeability might be due to the combined effect of increased grain size, increased densification, decreased anisotropy and compressive macro-stresses, etc. The La solubility in the ferrite lattice was very low ( $\sim 0.1$  atom/unit cell).

The Sm substitution showed the formation of secondary phase  $\text{SmFeO}_3$  in the ferrites. Bulk density and grain size of the ferrites increased with increasing Sm substitution up to 2.5 atom%. Electromagnetic properties were maximized in  $(\text{Ni}_{0.25}\text{Cu}_{0.2}\text{Zn}_{0.55})\text{Sm}_{0.05}\text{Fe}_{1.95}\text{O}_4$  composition. An initial permeability of about 312, saturation magnetization of about 70 emu/gm and resistivity of about 54 M $\Omega$ -cm at 100 kHz were measured in the composition.

$\text{V}_2\text{O}_5$  exhibited better densification behavior among all sintering aids with an onset sintering temperature of  $\sim 825^\circ\text{C}$ . The electromagnetic properties of the ferrite were also better in this  $\text{V}_2\text{O}_5$  doped ferrites.

---

***Keywords:***

NiCuZn ferrite; Magnetic ceramics; Sol-gel auto combustion;  $\text{Mg}^{2+}$  ions;  $\text{La}^{3+}$  ions;  $\text{Sm}^{3+}$  ions; Substitution; Sintering aids; Microstructure; Electromagnetic properties.

# CONTENTS

---

	<b>Page No</b>
<i>Acknowledgement</i>	iv
<i>Abstract</i>	vi
<i>Table of Contents</i>	viii
<i>List of Figures</i>	xi
<i>List of Tables</i>	xvii
<i>Nomenclature</i>	xix
<b>1. Introduction</b>	
1.1 Introduction	1
1.2 Organization of the Thesis	5
<b>2. Literature Review</b>	
2.1 Introduction	7
2.2 Synthesis of NiCuZn Ferrites	7
2.3 Effect of Divalent Cation Substitution	8
2.4 Effect of Rare Earth Cation Substitution	15
2.5 Effect of Sintering Aids	20
2.6 Summary and Scope of Work	26
2.7 Objectives of Present Work	27
<b>3. Experimental Work</b>	
3.1 Synthesis of Ferrite Powder	28
3.1.1 Chemical Analysis of Raw Material	28
3.1.2 Sol-Gel Auto Combustion Synthesis	29
3.2 Dried Gel and Powder Characterization	31
3.2.1 Thermal Analysis	31
3.2.2 Phase and Crystallite Size Analysis	32
3.2.3 Surface Area	34
3.2.4 Densification Study	35
3.3 Fabrication and Sintering of Ferrite Parts	36
3.3.1 Fabrication	36
3.3.2 Sintering	37
3.4 Characterization of Sintered Specimens	38



3.4.1 Density and Apparent Porosity	38
3.4.2 Microstructural Analysis	39
3.4.3 Phase Analysis and Structural Refinement	40
3.4.4 Magnetization	42
3.4.5 Inductance and Magnetic Loss	42
3.4.6 Resistivity	44
<b>4. Results and Discussion</b>	
<b>4.1 Optimization of Zn concentration in <math>\text{Ni}_{0.8-x}\text{Cu}_{0.2}\text{Zn}_x\text{Fe}_2\text{O}_4</math> ferrite (<math>0.45 \leq x \leq 0.6</math>)</b>	
4.1.1 Introduction	46
4.1.2 Results and Discussion	46
4.1.2.1 Thermal Decomposition	46
4.1.2.2 Phase Analysis	48
4.1.2.3 Densification and Microstructure	51
4.1.2.4 Electromagnetic Properties	53
4.1.3 Summary	59
<b>4.2 Effect of Mg substitution on structural and electromagnetic properties of <math>(\text{Ni}_{0.25}\text{Cu}_{0.2}\text{Zn}_{0.55})\text{Fe}_2\text{O}_4</math> ferrite</b>	
4.2.1 Introduction	60
4.2.2 Results and Discussion	60
4.2.2.1 Phase Analysis	60
4.2.2.2 Densification and Microstructure	63
4.2.2.3 Electromagnetic Properties	64
4.2.3 Summary	69
<b>4.3 Effect of La substitution on structural and electromagnetic properties of <math>(\text{Ni}_{0.25}\text{Cu}_{0.2}\text{Zn}_{0.55})\text{Fe}_2\text{O}_4</math> ferrite</b>	
4.3.1 Introduction	70
4.3.2 Results and Discussion	70
4.3.2.1 Phase Analysis	70
4.3.2.2 Densification and Microstructure	74
4.3.2.3 Rietveld Analysis	77
4.3.2.4 Electromagnetic Properties	80
4.3.3 Summary	87

<b>4.4 Effect of Sm substitution on structural and electromagnetic properties of <math>(\text{Ni}_{0.25}\text{Cu}_{0.2}\text{Zn}_{0.55})\text{Fe}_2\text{O}_4</math> ferrite</b>	
4.4.1 Introduction	88
4.4.2 Results and Discussion	88
4.4.2.1 Phase Analysis	88
4.4.2.2 Densification and Microstructure	91
4.4.2.3 Electromagnetic Properties	92
4.4.3 Summary	98
<b>4.5 Effect of <math>\text{Bi}_2\text{O}_3</math>-<math>\text{V}_2\text{O}_5</math>-<math>\text{MoO}_3</math> addition on structural, densification behaviors and electromagnetic properties of <math>(\text{Ni}_{0.25}\text{Cu}_{0.2}\text{Zn}_{0.55})\text{Fe}_2\text{O}_4</math> ferrite</b>	
4.5.1 Introduction	100
4.5.2 Results and Discussion	101
4.5.2.1 Phase Analysis	101
4.5.2.2 Densification and Microstructure	103
4.5.2.3 Electromagnetic Properties	106
4.5.3 Summary	111
<b>5. Conclusions and Future Work</b>	
5.1 Conclusions	112
5.2 Scope for Future Work	113
<b>References</b>	115
<b>Publications resulting from the Ph.D. work</b>	122
<b>Curriculum Vitae</b>	124

# LIST OF FIGURES

---

Fig. No	Figure Caption	Page No
<b>Chapter 1</b>		
Fig. 1.1.	Two sub cells of a unit cell of the spinel structure	2
<b>Chapter 2</b>		
Fig. 2.1.	AC resistivity of $(\text{Ni}_{0.5-x}\text{Cu}_x\text{Zn}_{0.5}\text{O})(\text{Fe}_2\text{O}_3)_{0.98}$ sintered at $1000^\circ\text{C}$ as a function of frequency.	10
Fig. 2.2.	Composition dependence of magnetostriction constant $\lambda_{111}$ at 300 K.	15
Fig. 2.3.	Microstructure obtained by SEM after sintering at $1200^\circ\text{C}$ for 2h of $(\text{Ni}_{0.5}\text{Zn}_{0.5})\text{Fe}_{2-x}\text{Sm}_x\text{O}_4$ with x = a) 0.0 and b) 0.1 % mol.	19
Fig. 2.4.	Variation of initial permeability $\mu_i$ with temperature (T) for $(\text{Cu}_{0.5}\text{Zn}_{0.5})\text{Fe}_{2-x}\text{RE}_x\text{O}_4$ ferrites.	20
Fig. 2.5.	Initial permeability of $(\text{Ni}_{0.2}\text{Cu}_{0.2}\text{Zn}_{0.6})_{1.02}(\text{Fe}_2\text{O}_3)_{0.98}$ ferrite with addition of $\text{MoO}_3$ (wt%) sintered at $900^\circ\text{C}$ and $850^\circ\text{C}$ for 5hrs (■: $900^\circ\text{C}$ , ●: $850^\circ\text{C}$ ).	23
<b>Chapter 3</b>		
Fig. 3.1.	Flow diagram for auto combustion synthesis of NiCuZn ferrite powder.	32
Fig. 3.2.	Photograph of (a) nitrate-citrate solution, (b) dry gel, (c) auto combustion reaction and (d) burnt ash powder.	33
Fig. 3.3.	A flow chart of fabrication and characterization for sintered ferrite parts.	36
Fig. 3.4.	A typical sintering profile of ferrite specimens at $900^\circ\text{C}$ for 4 hrs.	37
Fig. 3.5.	Low capacitance winding of six turns on ferrite core.	43
Fig. 3.6.	Schematic electrode arrangement on the sintered pellet sample.	44

## Chapter 4

- Fig. 4.1.** DTA/TG plots for the nitrate-citrate gel with a heating rate of 10°C /min in air atmosphere. 47
- Fig. 4.2.** XRD patterns of as-burnt powder of  $(\text{Ni}_{0.8-x}\text{Cu}_{0.2}\text{Zn}_x)\text{Fe}_2\text{O}_4$  ferrite with different Zn content. 49
- Fig. 4.3.** XRD patterns of (a) as-burnt, (b) calcined and (c) sintered  $(\text{Ni}_{0.2}\text{Cu}_{0.2}\text{Zn}_{0.6})\text{Fe}_2\text{O}_4$  ferrite. 49
- Fig. 4.4.** Crystallite size and lattice parameter of sintered  $(\text{Ni}_{0.8-x}\text{Cu}_{0.2}\text{Zn}_x)\text{Fe}_2\text{O}_4$  ferrite with different Zn content. 50
- Fig. 4.5.** Bulk density and apparent porosity of sintered  $(\text{Ni}_{0.8-x}\text{Cu}_{0.2}\text{Zn}_x)\text{Fe}_2\text{O}_4$  ferrite with different Zn content. 51
- Fig. 4.6.** Shrinkage curve at 5°C/min heating rate in air for  $(\text{Ni}_{0.8-x}\text{Cu}_{0.2}\text{Zn}_x)\text{Fe}_2\text{O}_4$  ferrite with different Zn content. 52
- Fig. 4.7.** SEM microstructures of sintered  $(\text{Ni}_{0.8-x}\text{Cu}_{0.2}\text{Zn}_x)\text{Fe}_2\text{O}_4$  ferrite with (a)  $x=0.45$ , (b)  $x=0.50$ , (c)  $x=0.55$  and (d)  $x=0.60$ . 53
- Fig. 4.8.** Magnetic hysteresis curve for  $(\text{Ni}_{0.8-x}\text{Cu}_{0.2}\text{Zn}_x)\text{Fe}_2\text{O}_4$  ferrite with different Zn content measured by VSM at room temperature. 55
- Fig. 4.9.** Frequency dependency of initial permeability in  $(\text{Ni}_{0.8-x}\text{Cu}_{0.2}\text{Zn}_x)\text{Fe}_2\text{O}_4$  ferrite with different Zn content. 56
- Fig. 4.10.** Relative loss factor as a function of frequency in  $(\text{Ni}_{0.8-x}\text{Cu}_{0.2}\text{Zn}_x)\text{Fe}_2\text{O}_4$  ferrite with different Zn content. 57
- Fig. 4.11.** AC resistivity as a function of frequency in  $(\text{Ni}_{0.8-x}\text{Cu}_{0.2}\text{Zn}_x)\text{Fe}_2\text{O}_4$  ferrite with different Zn content. 58
- Fig. 4.12.** XRD patterns of as-burnt  $(\text{Ni}_{0.25-x}\text{Mg}_x\text{Cu}_{0.2}\text{Zn}_{0.55})\text{Fe}_2\text{O}_4$  ferrites with different Mg content. 61
- Fig. 4.13.** XRD patterns of sintered  $(\text{Ni}_{0.25-x}\text{Mg}_x\text{Cu}_{0.2}\text{Zn}_{0.55})\text{Fe}_2\text{O}_4$  ferrites with different Mg content. 62
- Fig. 4.14.** Bulk density and grain size of sintered  $(\text{Ni}_{0.25-x}\text{Mg}_x\text{Cu}_{0.2}\text{Zn}_{0.55})\text{Fe}_2\text{O}_4$  ferrites with different Mg content. 63

<b>Fig. 4.15.</b>	SEM photographs of sintered $(\text{Ni}_{0.25-x}\text{Mg}_x\text{Cu}_{0.2}\text{Zn}_{0.55})\text{Fe}_2\text{O}_4$ ferrites with (a) $x=0.07$ , (b) $x=0.13$ , (c) $x=0.18$ and (d) $x=0.25$ .	64
<b>Fig. 4.16.</b>	Magnetic hysteresis curve for $(\text{Ni}_{0.25-x}\text{Mg}_x\text{Cu}_{0.2}\text{Zn}_{0.55})\text{Fe}_2\text{O}_4$ ferrites with different Mg content measured by VSM at room temperature.	65
<b>Fig. 4.17.</b>	Initial Permeability as a function of Mg content in $(\text{Ni}_{0.25-x}\text{Mg}_x\text{Cu}_{0.2}\text{Zn}_{0.55})\text{Fe}_2\text{O}_4$ ferrites.	66
<b>Fig. 4.18.</b>	Frequency dependence of initial permeability in $(\text{Ni}_{0.25-x}\text{Mg}_x\text{Cu}_{0.2}\text{Zn}_{0.55})\text{Fe}_2\text{O}_4$ ferrites with different Mg content.	67
<b>Fig. 4.19.</b>	Relative loss factor as a function of frequency in $(\text{Ni}_{0.25-x}\text{Mg}_x\text{Cu}_{0.2}\text{Zn}_{0.55})\text{Fe}_2\text{O}_4$ ferrites with different Mg content.	68
<b>Fig. 4.20.</b>	AC Resistivity as a function of frequency in $(\text{Ni}_{0.25-x}\text{Mg}_x\text{Cu}_{0.2}\text{Zn}_{0.55})\text{Fe}_2\text{O}_4$ ferrites with different Mg content.	69
<b>Fig. 4.21.</b>	XRD patterns of the as-burnt $(\text{Ni}_{0.25}\text{Cu}_{0.2}\text{Zn}_{0.55})\text{La}_x\text{Fe}_{2-x}\text{O}_4$ ferrite with (a) $x = 0.0$ , (b) $x=0.025$ , (c) $x=0.05$ and (d) $x=0.075$ .	71
<b>Fig. 4.22.</b>	XRD patterns of $(\text{Ni}_{0.25}\text{Cu}_{0.2}\text{Zn}_{0.55})\text{La}_x\text{Fe}_{2-x}\text{O}_4$ ferrites with (A) $x=0.025$ , (B) $x=0.075$ and in each (a) as-burnt powder (b) calcined powder and (c) sintered pellets.	72
<b>Fig. 4.23.</b>	XRD patterns of $(\text{Ni}_{0.25}\text{Cu}_{0.2}\text{Zn}_{0.55})\text{La}_x\text{Fe}_{2-x}\text{O}_4$ ferrites (a) undoped calcined powder and sintered pellets of (b) $x = 0.0$ , (c) $x=0.025$ , (d) $x=0.05$ and (e) $x=0.075$ .	73
<b>Fig. 4.24.</b>	SEM photographs of sintered $(\text{Ni}_{0.25}\text{Cu}_{0.2}\text{Zn}_{0.55})\text{La}_x\text{Fe}_{2-x}\text{O}_4$ ferrites with (A) $x=0.0$ , (B) $x=0.025$ , (C) $x=0.05$ and (D) $x=0.075$ .	75
<b>Fig. 4.25.</b>	EDX spectrum obtained from the center of grain boundary of $\text{LaFeO}_3$ phase.	76
<b>Fig. 4.26.</b>	EDX spectrum obtained from the center of La substituted NiCuZn ferrite grains.	76

<b>Fig. 4.27.</b>	Comparison between experimental (+) and calculated (-) X-ray diffraction pattern of $(\text{Ni}_{0.25}\text{Cu}_{0.2}\text{Zn}_{0.55})\text{Fe}_2\text{O}_4$ ferrite fitted for spinel phases. Difference between the observed and the calculated pattern is given in the bar.	77
<b>Fig. 4.28.</b>	Comparison between experimental (+) and calculated (-) X-ray diffraction pattern of $(\text{Ni}_{0.25}\text{Cu}_{0.2}\text{Zn}_{0.55})\text{La}_{0.075}\text{Fe}_{1.925}\text{O}_4$ ferrite fitted for spinel and $\text{LaFeO}_3$ phases. Difference between the observed and the calculated pattern is given in the bar.	78
<b>Fig. 4.29.</b>	Initial Permeability as a function of La substitution in $(\text{Ni}_{0.25}\text{Cu}_{0.2}\text{Zn}_{0.55})\text{La}_x\text{Fe}_{2-x}\text{O}_4$ ferrites.	81
<b>Fig. 4.30.</b>	Frequency dependence of permeability in $(\text{Ni}_{0.25}\text{Cu}_{0.2}\text{Zn}_{0.55})\text{La}_x\text{Fe}_{2-x}\text{O}_4$ ferrites with different La content.	83
<b>Fig. 4.31.</b>	Magnetic hysteresis curve for $(\text{Ni}_{0.25}\text{Cu}_{0.2}\text{Zn}_{0.55})\text{La}_x\text{Fe}_{2-x}\text{O}_4$ ferrites with different La content measured at room temperature.	84
<b>Fig. 4.32.</b>	Temperature dependency of permeability in $(\text{Ni}_{0.25}\text{Cu}_{0.2}\text{Zn}_{0.55})\text{La}_x\text{Fe}_{2-x}\text{O}_4$ ferrites with different La content.	85
<b>Fig. 4.33.</b>	Relative loss factor as a function of frequency in $(\text{Ni}_{0.25}\text{Cu}_{0.2}\text{Zn}_{0.55})\text{La}_x\text{Fe}_{2-x}\text{O}_4$ ferrites with different La content.	86
<b>Fig. 4.34.</b>	XRD patterns of the as-burnt $(\text{Ni}_{0.25}\text{Cu}_{0.2}\text{Zn}_{0.55})\text{Sm}_x\text{Fe}_{2-x}\text{O}_4$ ferrites with (a) $x = 0.0$ , (b) $x = 0.025$ , (c) $x = 0.05$ and (d) $x = 0.075$ .	89
<b>Fig. 4.35.</b>	XRD patterns of sintered $(\text{Ni}_{0.25}\text{Cu}_{0.2}\text{Zn}_{0.55})\text{Sm}_x\text{Fe}_{2-x}\text{O}_4$ ferrites with different Sm content (a) $x = 0.0$ , (b) $x = 0.025$ , (c) $x = 0.05$ and (d) $x = 0.075$ .	90
<b>Fig. 4.36.</b>	Bulk density and grain size of sintered $(\text{Ni}_{0.25}\text{Cu}_{0.2}\text{Zn}_{0.55})\text{Sm}_x\text{Fe}_{2-x}\text{O}_4$ ferrites with different Sm content.	91

<b>Fig. 4.37.</b>	SEM images of sintered $(\text{Ni}_{0.25}\text{Cu}_{0.2}\text{Zn}_{0.55})\text{Sm}_x\text{Fe}_{2-x}\text{O}_4$ ferrites with different Sm-content (A) $x=0.0$ , (B) $x=0.025$ , (C) $x=0.05$ and (D) $x=0.075$ .	93
<b>Fig. 4.38.</b>	EDX spectrum obtained from the center of grain boundary of $\text{SmFeO}_3$ phase.	93
<b>Fig. 4.39.</b>	Permeability as a function of Sm-substitution in $(\text{Ni}_{0.25}\text{Cu}_{0.2}\text{Zn}_{0.55})\text{Sm}_x\text{Fe}_{2-x}\text{O}_4$ ferrites.	94
<b>Fig. 4.40.</b>	Frequency dependency of permeability in $(\text{Ni}_{0.25}\text{Cu}_{0.2}\text{Zn}_{0.55})\text{Sm}_x\text{Fe}_{2-x}\text{O}_4$ ferrites with different Sm-content.	95
<b>Fig. 4.41.</b>	Magnetic hysteresis loop for $(\text{Ni}_{0.25}\text{Cu}_{0.2}\text{Zn}_{0.55})\text{Sm}_x\text{Fe}_{2-x}\text{O}_4$ ferrites with different Sm-content measured at room temperature.	96
<b>Fig. 4.42.</b>	Relative loss factor as a function of frequency in $(\text{Ni}_{0.25}\text{Cu}_{0.2}\text{Zn}_{0.55})\text{Sm}_x\text{Fe}_{2-x}\text{O}_4$ ferrites with different Sm-content.	97
<b>Fig. 4.43.</b>	Temperature dependency of permeability in $(\text{Ni}_{0.25}\text{Cu}_{0.2}\text{Zn}_{0.55})\text{Sm}_x\text{Fe}_{2-x}\text{O}_4$ ferrites with different Sm-content.	97
<b>Fig. 4.44.</b>	AC Resistivity as a function of frequency in $(\text{Ni}_{0.25}\text{Cu}_{0.2}\text{Zn}_{0.55})\text{Sm}_x\text{Fe}_{2-x}\text{O}_4$ ferrites with different Sm-content.	98
<b>Fig. 4.45.</b>	XRD patterns of the a) sintered $(\text{Ni}_{0.25}\text{Cu}_{0.2}\text{Zn}_{0.55})\text{Fe}_2\text{O}_4$ ferrite and that added with sintering additives like b) $\text{V}_2\text{O}_5$ , c) $\text{Bi}_2\text{O}_3$ , d) $\text{MoO}_3$ , e) $\text{V}_2\text{O}_5$ plus $\text{Bi}_2\text{O}_3$ , f) $\text{V}_2\text{O}_5$ plus $\text{MoO}_3$ , g) $\text{Bi}_2\text{O}_3$ plus $\text{MoO}_3$ and h) $\text{V}_2\text{O}_5$ plus $\text{Bi}_2\text{O}_3$ plus $\text{MoO}_3$ .	102
<b>Fig. 4.46.</b>	Shrinkage curves for $(\text{Ni}_{0.25}\text{Cu}_{0.2}\text{Zn}_{0.55})\text{Fe}_2\text{O}_4$ ferrites those modified with different additives. Shrinkage was measured at a heating rate of $5^\circ\text{C}/\text{min}$ in air.	103
<b>Fig. 4.47.</b>	Bulk densities of the sintered $(\text{Ni}_{0.25}\text{Cu}_{0.2}\text{Zn}_{0.55})\text{Fe}_2\text{O}_4$ ferrites with different additives and sintered at different temperatures.	104

<b>Fig. 4.48.</b>	Variation of porosity with sintering temperature of $(\text{Ni}_{0.25}\text{Cu}_{0.2}\text{Zn}_{0.55})\text{Fe}_2\text{O}_4$ ferrites having different additives.	105
<b>Fig. 4.49.</b>	SEM photographs of sintered $(\text{Ni}_{0.25}\text{Cu}_{0.2}\text{Zn}_{0.55})\text{Fe}_2\text{O}_4$ ferrite a) undoped and doped with sintering additives like b) $\text{V}_2\text{O}_5$ , c) $\text{Bi}_2\text{O}_3$ and d) $\text{MoO}_3$ .	107
<b>Fig. 4.50.</b>	SEM photographs of sintered $(\text{Ni}_{0.25}\text{Cu}_{0.2}\text{Zn}_{0.55})\text{Fe}_2\text{O}_4$ ferrite doped with sintering additives like e) $\text{V}_2\text{O}_5$ plus $\text{Bi}_2\text{O}_3$ , f) $\text{V}_2\text{O}_5$ plus $\text{MoO}_3$ , g) $\text{Bi}_2\text{O}_3$ plus $\text{MoO}_3$ and h) $\text{V}_2\text{O}_5$ plus $\text{Bi}_2\text{O}_3$ plus $\text{MoO}_3$ .	108
<b>Fig. 4.51.</b>	Variation of permeability with sintering temperature of different additives modified $(\text{Ni}_{0.25}\text{Cu}_{0.2}\text{Zn}_{0.55})\text{Fe}_2\text{O}_4$ ferrites.	109
<b>Fig. 4.52.</b>	Magnetic hysteresis loop of $(\text{Ni}_{0.25}\text{Cu}_{0.2}\text{Zn}_{0.55})\text{Fe}_2\text{O}_4$ ferrite sintered at $950^\circ\text{C}$ with different additives.	109
<b>Fig. 4.53.</b>	AC resistivity as a function of frequency in $(\text{Ni}_{0.25}\text{Cu}_{0.20}\text{Zn}_{0.55})\text{Fe}_2\text{O}_4$ ferrite (Sintered at $950^\circ\text{C}$ for 4 hrs) with different additives.	110
<b>Fig. 4.54.</b>	Magnetic loss as a function of frequency in $(\text{Ni}_{0.25}\text{Cu}_{0.20}\text{Zn}_{0.55})\text{Fe}_2\text{O}_4$ ferrite (Sintered at $950^\circ\text{C}$ for 4 hrs) with different additives.	111



## *LIST OF TABLES*

<b>Table No</b>	<b>Table Caption</b>	<b>Page No</b>
<b>Table 4.1</b>	Crystallite size, lattice parameter, bulk density, apparent porosity and grain size of sintered $(\text{Ni}_{0.80-x}\text{Cu}_{0.2}\text{Zn}_x)\text{Fe}_2\text{O}_4$ with different Zn content.	50
<b>Table 4.2</b>	Permeability, saturation magnetization and resistivity of sintered $(\text{Ni}_{0.80-x}\text{Cu}_{0.2}\text{Zn}_x)\text{Fe}_2\text{O}_4$ with different Zn content (measured at room temperature).	54
<b>Table 4.3</b>	Crystallite size, lattice parameter, bulk density, apparent porosity, percent closed porosity and grain size for sintered $(\text{Ni}_{0.25-x}\text{Mg}_x\text{Cu}_{0.2}\text{Zn}_{0.55})\text{Fe}_2\text{O}_4$ ferrites with different Mg content.	62
<b>Table 4.4</b>	Saturation magnetization, permeability and resistivity for sintered $(\text{Ni}_{0.25-x}\text{Mg}_x\text{Cu}_{0.2}\text{Zn}_{0.55})\text{Fe}_2\text{O}_4$ ferrites with different Mg content (measured at room temperature).	65
<b>Table 4.5</b>	Bulk density, apparent porosity and grain size, of sintered $(\text{Ni}_{0.25}\text{Cu}_{0.2}\text{Zn}_{0.55})\text{La}_x\text{Fe}_{2-x}\text{O}_4$ ferrites with different La content.	74
<b>Table 4.6</b>	Refined cell parameter, crystallite size, micro-strain, macro-stress, % $\text{LaFeO}_3$ phase content, agreement factors (R-factors) and goodness of fit (G.O.F.) obtained from Rietveld fits for $(\text{Ni}_{0.25}\text{Cu}_{0.2}\text{Zn}_{0.55})\text{La}_x\text{Fe}_{2-x}\text{O}_4$ ferrites with $x=0.0$ , $x=0.025$ , $x=0.05$ and $x=0.075$ .	79
<b>Table 4.7</b>	Permeability, wall permeability ( $\mu_w$ ), rotational permeability ( $\mu_{rk}$ ), anisotropy field ( $H_a$ ) and saturation magnetization ( $M_s$ ) of $(\text{Ni}_{0.25}\text{Cu}_{0.2}\text{Zn}_{0.55})\text{La}_x\text{Fe}_{2-x}\text{O}_4$ ferrite with different La content.	81
<b>Table 4.8</b>	Coercive field ( $H_c$ ), Curie temperature and resistivity of $(\text{Ni}_{0.25}\text{Cu}_{0.2}\text{Zn}_{0.55})\text{La}_x\text{Fe}_{2-x}\text{O}_4$ ferrites with different La content.	85

<b>Table 4.9</b>	Crystallite size, lattice parameter, bulk density, apparent porosity, and grain size of sintered $(\text{Ni}_{0.25}\text{Cu}_{0.2}\text{Zn}_{0.55})\text{Sm}_x\text{Fe}_{2-x}\text{O}_4$ ferrites with different Sm content.	91
<b>Table 4.10</b>	Permeability, saturation magnetization, Curie temperature and resistivity of sintered $(\text{Ni}_{0.25}\text{Cu}_{0.2}\text{Zn}_{0.55})\text{Sm}_x\text{Fe}_{2-x}\text{O}_4$ ferrites with different Sm-content.	94
<b>Table 4.11</b>	Weight percent of different sintering additives used in $(\text{Ni}_{0.25}\text{Cu}_{0.2}\text{Zn}_{0.55})\text{Fe}_2\text{O}_4$ ferrite.	101
<b>Table 4.12</b>	Crystallite size of pure and different sintering additives modified $(\text{Ni}_{0.25}\text{Cu}_{0.2}\text{Zn}_{0.55})\text{Fe}_2\text{O}_4$ ferrite sintered at different temperatures.	102
<b>Table 4.13</b>	Onset temperature of shrinkage curve of $(\text{Ni}_{0.25}\text{Cu}_{0.2}\text{Zn}_{0.55})\text{Fe}_2\text{O}_4$ ferrite with different sintering additives.	104
<b>Table 4.14</b>	Resistivities of $(\text{Ni}_{0.25}\text{Cu}_{0.2}\text{Zn}_{0.55})\text{Fe}_2\text{O}_4$ ferrite with sintering temperature 900°C for different additives modified specimens.	110

## NOMENCLATURE

---

$\lambda$	X-ray wavelength
$\rho$	AC resistivity
$\sigma$	Moment/gm
$\theta$	Bragg's angle
$\gamma_w$	Domain wall energy
$\epsilon_0$	Permittivity of free space
$\epsilon'$	Dielectric constant
$\phi_e$	Elemental stoichiometric coefficient
$\varphi_{ac}$	AC electrical conductivity
$k'$	Relative dielectric constant
$\zeta$	Inner stress
$\eta$	Magnetostriction constant
$\mu_i$	Initial permeability
$\mu_0$	Permeability of free space
$\mu_r$	Relative permeability
$\mu_{rk}$	Rotational permeability
$\mu_w$	Wall permeability
$\omega$	Angular frequency
$\omega_i$	Relaxation frequency
$^{\circ}\text{C}$	Degree celsius
$(hkl)$	Miller index
$a$	Lattice parameter
A	Tetrahedral site
A	Area
$A_w$	Atomic weight
$P_{APP}$	Apparent porosity
$b$	X-ray density
B	Octahedral site
$B$	Full width at half maximum of XRD peak
$B_m$	Induction magnetization

$B_r$	Remnant magnetization
$C$	Capacitance
$C$	Cation
$d$	Lattice spacing
$D_{in}$	Inner Diameter
$D_{od}$	Outer Diameter
$D_{Bulk}$	Bulk density
$D$	Average grain size
DTA	Differential thermal analysis
EDTA	Ethylene di-amine tetra acetic acid
EDX	Energy dispersive X-ray analysis
EMI	Electromagnetic interference
$f$	Frequency
$G$	Goodness of fit
$H$	Magnetic field
$H_a$	Anisotropy field
$H_c$	Coercive field strength
$H_t$	Height
$I$	Current
$I$	Intensity
JCPDS	Joint committee on powder diffraction standards
$K$	Crystal magnetic anisotropy
$L$	Inductance
LC	Inductor and capacitor
$M$	Magnetization
MAUD	Materials Analysis Using Diffraction
MLFCI	Multilayer ferrite chip inductor
$M_s$	Saturation magnetization
$M_w$	Molecular weight
$N$	Avogadro's number
$N_a$	Number of turn
(N)	Normality of the Solution
NiCuZn	Nickel-copper-zinc

O	Oxygen
ppm	Parts per million
PVA	Polyvinyl alcohol
$Q$	Quality factor
RE	Rare earth
RLF	Relative loss factor
s	Second
SEM	Scanning Electron Microscope
T	Absolute temperature in K
TD	Theoretical density
$\tan\delta$	Dissipation factor
t	Thickness
$t$	Crystallite size
$T_c$	Curie temperature
TGA	Thermo gravimetric analysis
TMA	Thermo mechanical analysis
$V$	Volume
VSM	Vibrating sample magnetometer
$V_{pi}$	Volume fraction occupied by pores
XRD	X-ray diffraction

# *Chapter I*

## *Introduction*

## 1.1 Introduction

Ferrites are magnetic ceramics containing iron oxide as a major constituent in it. It is now some 70 years since ferrites debuted as an important new category of magnetic materials. These are now very well established group of magnetic materials. Today ferrites are employed in a truly wide range of applications, and have contributed materially to the advances in electronics. In the area of new materials, ferrites with permeabilities up to 30,000 and power ferrites for frequencies up to 10 MHz have been made available commercially [1]. Even though, improvements and innovations continue to take place; many new applications, theories and preparation technologies are currently under development in field of ferrites.

The miniaturization trends of electronic devices result in the development of new device multilayer ferrite chip inductor (MLFCI) components. The traditional wire wound inductors can only be miniaturized to a certain limit and lack of magnetic shielding of this wire wound component leads to the development of MLFCI. Ferrite chip inductors are one of the important components for the latest electronics products such as cellular phones, video cameras, notebook computers, hard and floppy drives [2] etc.

The chip inductor is fabricated by laminating ferrite layers and internal metallic conductors alternately and then co-firing to form the monolithic structure [3]. In general, Ag, Pd metal or Ag/Pd alloy are used as an internal conductor. Ag is preferred among them due to its low cost, oxidative resistibility and low electrical resistivity resulting in components with high quality factor. Since the melting temperature of Ag is 961°C, the ferrite ceramics are required to be sintered at temperatures below 950°C to prevent Ag diffusion into the ferrite that would damage the insulation resistivity of ferrite [4-8].

Presently, NiCuZn ferrites have been the dominant materials for MLFCI due to its low sintering temperature (<950°C) and good electromagnetic properties [9-10]. In addition, NiCuZn ferrites have better high frequency properties compared to that of MnZn ferrite and low densification temperatures than NiZn ferrites [9, 11]. Since, the work is related to NiCuZn ferrite, a brief description about it is illustrated below.

NiCuZn ferrite is a spinel ferrite. Magnetic spinels have the general formula  $MO.Fe_2O_3$  or  $MFe_2O_4$  where, M is divalent metal ion. NiCuZn ferrite in spinel notation can be represented as  $(NiCuZn)_1Fe_2O_4$ . The spinel lattice is composed of a closed-packed oxygen arrangement in which 32 oxygen ions form a unit cell. There are two kinds of interstices in between the closed-packed anions as shown in Fig. 1.1; a) tetrahedrally coordinated interstices (called 'A' site) which are surrounded by 4 nearest neighboring oxygen ions and b) octahedrally coordinated interstices (called 'B' site) which are coordinated by 6 nearest neighboring oxygen ions. Structurally spinel can be represented as  $AB_2O_4$ . One unit cell of it contains eight formula units of  $AB_2O_4$ , where, out of 64 'A' sites 8 and out of 32 'B' sites 16 are occupied by cations.

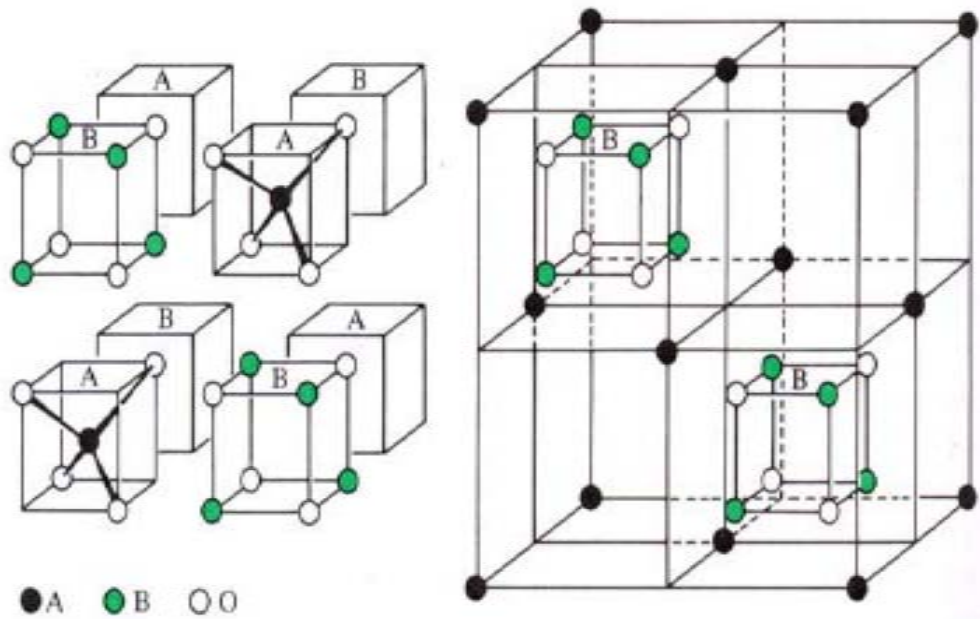


**Fig. 1.1.** Two sub cells of a unit cell of the spinel structure [1].

Depending on the cation distribution in interstices, the spinel is broadly divided into two groups: a) normal spinel and b) inverse spinel. In normal spinel ferrite  $MFe_2O_4$ , the divalent ions are all in 'A' sites and the  $Fe^{3+}$  ions occupy 'B' sites. Typical example of normal spinel is  $ZnFe_2O_4$ . In inverse spinel the divalent ions occupy some of the 'B' sites and the  $Fe^{3+}$  ions are divided equally between 'A' and 'B' sites. Most of the magnetic spinels are inverse type like  $NiFe_2O_4$ ,  $CuFe_2O_4$  and  $MnFe_2O_4$  etc.



NiCuZn ferrite is a solid solution of inverse NiFe<sub>2</sub>O<sub>4</sub>, CuFe<sub>2</sub>O<sub>4</sub> and normal ZnFe<sub>2</sub>O<sub>4</sub> ferrites. Due to the favorable fit of charge distribution, Ni<sup>2+</sup> and Cu<sup>2+</sup> ions show strong preference to ‘B’ sites. Zn<sup>2+</sup> ions show a strong preference for ‘A’ sites due to its electronic configuration. The structural formula can be represented by:



where, first bracket is represented by tetrahedral ‘A’ site and third bracket is represented by octahedral ‘B’ site.

Magnetism originates from the spin of unpaired electrons. Cations in ferrite lattice are separated by oxygen anions. O<sup>2-</sup> has no magnetic moment since it has completely filled shells, with p-type outer most orbitals. Ni<sup>2+</sup> (d<sup>8</sup>), Cu<sup>2+</sup> (d<sup>9</sup>), Zn<sup>2+</sup> (d<sup>10</sup>) and Fe<sup>3+</sup> (d<sup>5</sup>) cations of the ferrite have 2, 1, 0, and 5 unpaired electrons respectively. So divalent Ni, Cu and trivalent Fe have magnetic moments due to unfilled 3d sub-shell. Zn<sup>2+</sup> by contrast, is diamagnetic because the outer sub-shell of it is completely filled.

Since cations are separated by oxygen, cation-cation direct (ferromagnetic) interactions are negligible. When cations are bonded covalently to the O<sup>2-</sup>, p-orbital of oxygen interact with d-orbital of cations with; C-↑-↓-O-↑-↓-C (where C represents cation and O represents oxygen) anti-parallel spins of cations. This mechanism of indirect interaction is called super-exchange. There may be three types of interactions like A-O-B, B-O-B and A-O-A. Among them A-O-B interaction is the strongest one. As the number of unpaired electrons in different cations is not same, the resultant magnetization (moment/unit volume) is thus the difference between the magnetic moments of the octahedral lattice and that of the tetrahedral lattice. This type of magnetism is called ferrimagnetism and NiCuZn ferrite is a ferrimagnetic material.

The magnetic properties of the ferrites can be modified by distribution of cations in ‘A’ and ‘B’ sites through substitution. Typical example is the substitution of Ni by Zn. NiCu ferrite is inverse spinel where, half of the Fe<sup>3+</sup> are in ‘A’ sites; remaining half and Ni, Cu share ‘B’ sites. When Zn is substituted for Ni, Zn preferentially enters into the ‘A’ sites by displacing a proportionate number of Fe<sup>3+</sup> from ‘A’ to ‘B’ sites with a cation

distribution as stated in equation (1.1). The net effect is the significant increase in magnetic moments in octahedral site as well as in the unit cell.

Permeability and resistivity are the most important parameters used in evaluating magnetic materials. The electromagnetic properties of NiCuZn ferrites are highly sensitive to the processing parameters especially sintering conditions and the amount of constituent metal oxides in their composition [12-13].

In the recent years, there has been an increased interest in the application of NiCuZn ferrite for the production of MLFCI components. The applications of the chip inductors include [14-16], a) combined with capacitors to form inductor-capacitor (LC) filters, b) as Electromagnetic Interference (EMI) filters, c) as an AC choke for active devices (e.g. transistors), d) used in matching circuits, etc. Apart from this, ferrites are used in audio and visual equipments such as liquid crystal TV set headphone stereos, computer and telecommunication devices such as personal wireless communication systems and automobile telephones [17] etc.

Several studies have been conducted to enhance the properties of NiCuZn ferrite. Important approaches adopted are: (a) the reduction of the particle size to improve densification, (b) using sintering aids for better densification and (c) substitutions at tetrahedral and octahedral crystallographic site in the spinel ferrite to improve electromagnetic properties.

Various compositions in the system  $(\text{Ni}_{1-x-y}\text{Zn}_x\text{Cu}_y)\text{Fe}_2\text{O}_4$  were investigated. Cu is used in this ferrite to decrease the sintering temperature so that it can be co-fired with Ag internal electrode. However, Cu decreases the resistivity of the ferrite, which is not desirable for its high frequency applications. So, optimization of Cu content with respect to densification and resistivity of the ferrite is very important. Different ranges of electromagnetic properties have been reported with various Zn concentrations in NiCuZn ferrites. Optimization of Zn concentration with respect to Ni and Cu is essential to achieve desirable electromagnetic properties in the ferrites where, Zn enters into the 'A' sites (Fig 1.1) by displacing a proportionate number of  $\text{Fe}^{3+}$  from 'A' to 'B' sites.

One of the key parameters to increase the permeability in spinel ferrite is lowering the magnetostriction constant. As the magnetostriction constant of MgCuZn ferrite is lower than NiCuZn ferrite, Mg can be substituted for Ni to increase the permeability in  $(\text{Ni}_{1-x-y-z}\text{Mg}_x\text{Cu}_y\text{Zn}_z)\text{Fe}_2\text{O}_4$  ferrite where, Mg enters into the ‘B’ sites (Fig 1.1) by displacing a proportionate number of  $\text{Ni}^{2+}$ . Mg containing compositions were also preferred to avoid the presence of divalent iron (to obtain high resistivity) and to avoid the tendency of discontinuous grain growth.

Influence of rare earths on the properties of different ferrites has been reported by many investigators. Rare earth ions can improve densification and increase permeability and resistivity in  $(\text{Ni}_{1-x-y}\text{Zn}_x\text{Cu}_y)\text{RE}_z\text{Fe}_{2-z}\text{O}_4$  ferrites where, RE enters into the ‘B’ sites (Fig 1.1) by displacing a proportionate number of  $\text{Fe}^{3+}$  from ‘B’ to ‘A’ sites.  $\text{V}_2\text{O}_3$ ,  $\text{MoO}_3$  and  $\text{Bi}_2\text{O}_3$  were reported to be the most widely used sintering additives for the ferrites. Further research is needed on the mixed sintering additives in the system  $\text{V}_2\text{O}_5$ ,  $\text{Bi}_2\text{O}_3$  and  $\text{MoO}_3$  for the ferrites.

The objectives of the present study are, (a) optimization of  $\text{Zn}^{2+}$  concentration in  $(\text{Ni}_{0.8-x}\text{Cu}_{0.2}\text{Zn}_x)\text{Fe}_2\text{O}_4$  ferrite ( $0.45 \geq x \leq 0.6$ ), (b) study the effect of  $\text{Mg}^{2+}$  substitution for  $\text{Ni}^{2+}$  and (c) effect of  $\text{La}^{3+}$  and  $\text{Sm}^{3+}$  substitutions for  $\text{Fe}^{3+}$  on structural and electromagnetic properties of the optimized NiCuZn ferrites and (d) study the effect of sintering aids namely,  $\text{Bi}_2\text{O}_3$ ,  $\text{MoO}_3$  and  $\text{V}_2\text{O}_5$  on densification and electromagnetic properties in optimized NiCuZn ferrites.

## 1.2 Organization of the Thesis

The thesis has been divided into five chapters:

**Chapter–I** presents a brief introduction of NiCuZn ferrite and organization of thesis.

**Chapter–II** deals with detailed literature review. Attempts have been made to systematically classify the available information under different sections. This chapter incorporates background information to assist in understanding the aims and objectives of this investigation, and also reviews recent reports by other investigators with which these results can be compared.

**Chapter–III** enunciates with the detail experimental process related to this research work.

**Chapter–IV** describes the results and discussion, which has been divided into 5 sections, where, **(Section 1)** describes about the optimization of Zn concentration in  $(\text{Ni}_{0.8-x}\text{Cu}_{0.2}\text{Zn}_x)\text{Fe}_2\text{O}_4$  ferrite, **(Section 2)** explains about the effect of Mg substitution on electromagnetic properties of optimized NiCuZn ferrite, **(Section 3)** describes about the effect of La substitution on electromagnetic properties of NiCuZn ferrite, **(Section 4)** narrates about the effect of Sm substitution on electromagnetic properties of NiCuZn ferrite and finally **(Section 5)** deals with the effect of sintering aids like  $\text{Bi}_2\text{O}_3$ ,  $\text{V}_2\text{O}_5$  and  $\text{MoO}_3$  on densification behaviors and electromagnetic properties of NiCuZn ferrite.

**Chapter–V** contains the concluding remarks and the scope of future work.

A complete list of references has been given towards the end of the thesis. Finally, a concise list of publications in-peer reviewed international journals related to present research work has been presented at the end.

# *Chapter II*

## *Literature Review*

## 2.1 Introduction

In this chapter, an attempt is made to provide a review on the synthesis of NiCuZn ferrites, effect of substitutions and sintering aids on the properties of these ferrites.

## 2.2 Synthesis of NiCuZn Ferrites

Spinel ferrites are prepared through various methods like solid state, co-precipitation, hydrothermal, sol–gel, auto combustion etc.

NiCuZn ferrite has been synthesized through solid state method by many investigators [9, 10, 12, 18-22]. In this method, different metal oxides are mixed and calcined to get ferrite powders. However, mechanical mixing of different oxides is hardly intimate and homogeneous and hence it results in composition fluctuation at every stage of processing that also persists after sintering [23]. Solid state process requires calcination temperature more than 750°C for phase formation and sintering temperature more than 1000°C to achieve better densification. At this high sintering temperature, evaporation of Zn leads to the formation of chemically inhomogeneous material [24]. Chemical methods overcome the limitations of the method.

Co-precipitation process was used to synthesis of NiCuZn ferrites by many researchers [25-27]. *Hsu et al.* [25] obtained crystalline ferrite particles with particle size of about 30 nm. *Rahman et al.* [26] reported that the average crystallite size of as dried ferrite powder was 10 nm and crystallite size influenced the coercivity. *Modak et al.* [27] reported that the coercive field for the ferrite with particle size 12 nm was interestingly low (87 Am<sup>-1</sup>) and the saturation magnetization was moderately high (~ 50 Am<sup>2</sup>kg<sup>-1</sup>).

Co-precipitation method using microwave–hydrothermal reaction system was used by *Krishnaveni et al.* [2] to synthesize (Ni<sub>0.53</sub>Zn<sub>0.35</sub>Cu<sub>0.12</sub>)Fe<sub>2</sub>O<sub>4</sub> ferrite nano powders. The particle size of the synthesized powder was 10-30 nm. *Ghodake et al.* [28] reported the synthesis of (Ni<sub>x</sub>Zn<sub>t</sub>Cu<sub>[(1-t)-x]</sub>)Fe<sub>2</sub>O<sub>4</sub> ferrites by co-precipitation technique using oxalate precursors. Sol-gel method was used to synthesis the ferrite by *Zahi et al.*, *Yan et al.* and *Nam et al.* [29-31]. *Nam et al.* [31] observed nano-sized spherical NiCuZn ferrite having particle size 10-20 nm by this method.

These chemical methods have some disadvantages. They, have multiple step pathways that are time consuming, require expensive alkoxide precursor material and are highly pH sensitive which require special attention for complex systems like NiCuZn ferrites [32]. The auto combustion method has the advantages of using inexpensive precursors and low external energy consumption and resulting nano-sized, homogeneous, highly reactive powder.

Several researchers prepared NiCuZn ferrite [30, 33-36] including various other ferrites like MgCuZn [37], MgCu [38] and NiZn [39-40] by auto combustion method to produce nano precursor. Generally, metal nitrate salts are used as reactant and glycine [41], urea [40] and citric acid [33] are used as fuel in auto combustion method. Citric acid is preferred because both glycine and urea contains  $N_2$  and releases extra amount of pollutant  $N_2$  gas during combustion reaction.

Auto combustion process has been proved to be a simple and economic way to prepare nano scale ferrite powders [33]. Nano-structured materials offer novel properties. It decreases the free energy during sintering due to increasing surface area which is the main driving force for lowering the sintering temperature of particles. By proper tuning of the particle size, it is possible to optimize the desired properties like electrical, magnetic, optical, thermal, mechanical etc [42].

### **2.3 Effect of Divalent Cation Substitution**

Many investigators have focused their attention on the improvement of electromagnetic properties of the ferrite by divalent ions substitution. Generally, the divalent metal ions ( $M^{2+}$ ); Ni, Zn, Cu, Mg, Mn, Co or mixtures of these are substituted in different spinel ferrites.

These substitutes have different sitting preferences for the two sites ('A' and 'B') in the spinel structure and can change many properties as an effect of modified cation distribution in the ferrite. On the basis of site distribution of  $M^{2+}$  ions and the strength of the exchange interaction among magnetic ions, the influence of  $M^{2+}$  substitutions on

electromagnetic properties can be explained. The effect of different divalent cations in NiCuZn ferrite, along with some other spinel ferrites is reviewed below.

$Zn^{2+}$  is used to improve electromagnetic properties as well as densification in the ferrite. It is substituted in spinel ferrite to improve magnetization [43]. It also lowers magnetostriction and anisotropy in ferrites [1]. *Goey et al.* [22] stated that initial permeability increased and hysteresis loss decreased with increasing Zn concentration in  $(Ni_{0.85-y}Cu_{0.15}Zn_y)Fe_2O_4$  ferrite. Both saturation and remanence magnetization had maximum at  $y = 0.4$ . An improved electromagnetic properties were obtained by *Low et al.* [44] at high Zn content of  $(Ni_{0.02x}Cu_{0.02y}Zn_{0.02z})Fe_2O_4$ ; where  $x+y+z = 50$ .

*Ahmed et al.* [45] investigated the influence of zinc ion substitution on densification in NiZn ferrite. They found rapid densification with increased  $Zn^{2+}$  concentration. *Sun et al.* [46] reported the initial permeability and relative loss factor increased while the cut off frequency decreased with increasing Zn content in  $(Ni_{1-x}Zn_x)Fe_2O_4$  ferrite. Zn substituted  $(Cu_{1-x}Zn_x)Fe_2O_4$  ferrite had been prepared by *Ajmal et al.* [47]. They found that sintered density increased with increasing Zn concentration. Both saturation magnetization and magnetic moment increased with increasing Zn concentration up to  $x = 0.2$  and then decreased with further addition of Zn.

*Jadhav* [48] worked on the structural and magnetic properties of Zn substituted LiCu ferrites having composition  $(Li_xCu_{0.4}Zn_{0.6-2x})Fe_{2+x}O_4$  and found that the magnetic moment increased with increasing zinc content up to  $x = 0.15$  and then decreased with further addition of Zn. *Shaikh et al.* [49] investigated the electrical resistivity and Curie temperature of Zn substituted  $(Li_xMg_{0.4}Zn_{0.6-2x})Fe_{2+x}O_4$  ferrites and found that the resistivity initially decreased with Zn content up to 0.15 and then increased with further increasing Zn content. The Curie temperature was also found to decrease linearly with the addition of Zn. At high level of Zn substitution, the 'A' site magnetic ion became so diluted that the coupling between the two lattices was lost and the saturation magnetization dropped. An additional consequence of the weakening magnetic interactions was that the spin coupling could more easily be moved out of alignment by thermal energy vibrations so that, the Curie temperature decreased with Zn substitution.



Cu is conventionally used in NiCuZn ferrite to improve densification as well as electromagnetic properties [27]. The beneficial effect of copper ions on the densification of ferrite can be reasonably explained by possible sintering mechanisms that take place through a high atomic mobility of Cu ions at relatively low temperature. The increase of the lattice diffusion usually increases the diffusion path leading to an increase of the rate of cation inter diffusion in the solid solution, which is in agreement with the lattice diffusion mechanism proposed by Gupta and Coble [50, 51]. During sintering grain boundary diffusion [52] may play an important role in the grain growth because the activation energy for lattice diffusion is higher than that for grain boundary.

*Nam et al.* [5] investigated the effect of Cu substitution on the electromagnetic properties of  $(\text{Ni}_{0.5-x}\text{Zn}_{0.50}\text{Cu}_x)(\text{Fe}_2\text{O}_4)_{0.98}$  ferrite and found that electrical resistivity was maximum at  $x = 0.2$  as shown in Fig. 2.1. They also reported that saturation magnetization was maximum at  $x = 0.2$  in  $(\text{Ni}_{0.2}\text{Cu}_x\text{Zn}_{0.80-x})\text{Fe}_2\text{O}_4$  ferrite [31].

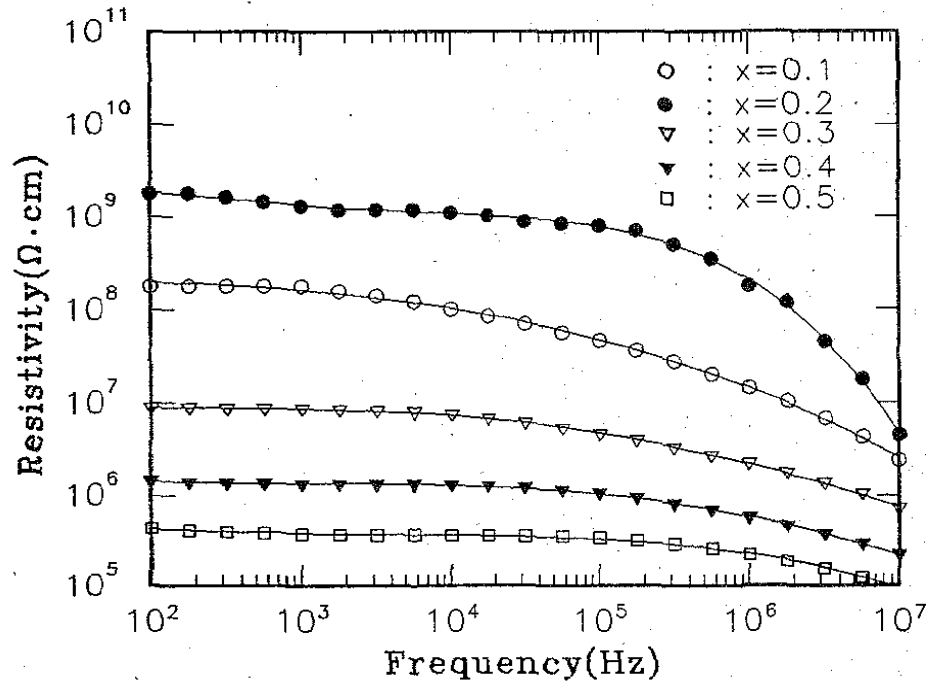


**Fig. 2.1.** AC resistivity of  $(\text{Ni}_{0.5-x}\text{Cu}_x\text{Zn}_{0.5}\text{O})(\text{Fe}_2\text{O}_3)_{0.98}$  sintered at 1000°C as a function of frequency [5].

*Shrotri et al.* [53] reported the effect of Cu substitution on the electromagnetic properties of  $(\text{Ni}_{0.8-x}\text{Cu}_x\text{Zn}_{0.2})\text{Fe}_2\text{O}_4$  ferrite and found that the bulk density, electrical resistivity and initial permeability increased considerably with the copper concentration up to  $x = 0.2$ . Saturation magnetization and Curie temperature decreased with Cu addition. *Caltun et al.* [54] also found improved electromagnetic properties at  $x = 0.2$  and suggested that the specific amount of Cu substitution ( $x = 0.2$ ) was favorable for the grain growth of  $(\text{NiZn})_{0.8-x}\text{Cu}_x\text{Zn}_{0.2}\text{Fe}_2\text{O}_4$  ferrite.

Further, *Rahman et al.* [26] worked in the same composition range and stated that the partial substitution of  $\text{Ni}^{2+}$  with  $\text{Cu}^{2+}$  (up to  $x = 0.25$ ) influenced the magnetic parameters due to the modification by cation re-distribution. It was found that the maximum coercivity dependent on average crystallite size. The saturation moment decreased linearly with the decrease in  $\text{Ni}^{2+}$  content replaced by  $\text{Cu}^{2+}$  ions at lower concentrations. At higher concentration deviation from this trend was found and magnetization increased with increasing Cu content.

The same property was found by *Hsu et al.* [25]. They reported that Cu substitution for Ni in NiZn ferrite would enhance the densification of the ferrite and subsequently increased the permeability value as well as saturation magnetization value and decreased the coercivity of the sintered ferrite. *Su et al.* [20] stated that the presence of Cu ion up to 4 mol% activated the sintering process leading to increase in density and decrease in magnetocrystalline anisotropy constant of NiCuZn ferrite.

*Yan et al.* [55] worked on the effect of CuO and  $\text{V}_2\text{O}_5$  additions on the microstructure and relative permeability of low temperature fired NiCuZn ferrite. They found high relative permeability value of  $\sim 1417$  at 10 mol% CuO and 0.20 mol%  $\text{V}_2\text{O}_5$  addition. *Low et al.* [44] reported that the increase in Cu content caused a decrease in the dissociation temperature and was beneficial to the electromagnetic properties of NiCuZn ferrite as a result of grain growth and better densification. The range of critical CuO content was determined to be 12-20 mol%.

*Dimri et al.* [56] studied the effect of compositional variation on structural, dielectric and magnetic properties of the Cu substituted  $(\text{Ni}_{0.6-x}\text{Cu}_x\text{Zn}_{0.4})\text{Fe}_2\text{O}_4$  ferrite. The results showed that the addition of copper promoted grain growth, resulting increase in grain size. However, Curie temperature was understandably lowered with the increase in Cu content. A saturation magnetization value of 92 emu/gm was obtained for the composition  $x = 0.2$ . Ferrite with Cu concentration of  $x = 0.4$  showed the highest initial permeability.

Cu is also used in other ferrites as divalent cation for improving electromagnetic properties and for lowering the sintering temperature. *Yue et al.* [37] worked on the effect of copper on the electromagnetic properties of  $(\text{Mg}_{0.5-x}\text{Cu}_x\text{Zn}_{0.5})\text{O}(\text{Fe}_2\text{O}_3)_{0.98}$  ferrites and found that the density, grain size, permeability, Curie temperature increased, resistivity decreased with Cu content up to  $x = 0.40$ . *Rezlescu et al.* [57] reported the effect of Cu substitution on the physical properties of  $(\text{Mg}_{0.5-x}\text{Cu}_x\text{Zn}_{0.5})\text{Fe}_2\text{O}_4 + 0.5\text{MgO}$  ferrites. They found that the density increased up to  $x = 0.30$  whereas, resistivity increased up to  $x = 0.10$  and permeability increased with Cu content as well. They [58] also reported that the sintered density and resistivity of  $(\text{Mg}_{0.5-x}\text{Cu}_x\text{Zn}_{0.5}\text{O})\text{Fe}_2\text{O}_3$  ferrite increased up to  $x = 0.3$  whereas, permeability increased up to  $x = 0.4$ .

*Hoque et al.* [59] reported that the maximization of initial permeability and saturation magnetization at  $x = 0.2$  in  $(\text{Ni}_{1-x}\text{Cu}_x)\text{Fe}_2\text{O}_4$  ferrite, which could be attributed to the maximum sintered density obtained for this composition. *Haque et al.* [60] worked on Cu substituted MgZn ferrites. They found a remarkable increase in the bulk density with increasing Cu substitution for Mg. By incorporating CuO, the initial permeabilities of the samples increased. Saturation magnetization increased slightly with increasing copper content upto  $x \leq 0.30$  and then it decreased for  $x = 0.35$ . Cu substitution is also used in hard ferrites for improving properties [61].

Other interesting divalent cation is  $\text{Mn}^{2+}$ . *Yue et al.* [62] first worked on Mn substituted  $(\text{Ni}_{0.25-x}\text{Mn}_x\text{Cu}_{0.25}\text{Zn}_{0.5})\text{O}(\text{Fe}_2\text{O}_3)_{0.98}$  ferrites and found that the resonant frequency and the Curie temperature decreased with increasing Mn content whereas, the  $\mu'_i$  increased up to  $x = 0.06$ . The same group reported [34] on effect of Mn substitution on

electromagnetic properties of  $(\text{Ni}_{0.2}\text{Cu}_{0.2}\text{Zn}_{0.6})\text{O}(\text{Fe}_{2-x}\text{Mn}_x\text{O}_3)_{0.98}$  ferrites. It was found that Mn content in formulations largely affected the grain size and electromagnetic properties of sintered NiCuZn ferrites. With increasing Mn content, the initial permeability was significantly increased, while the electrical resistivity and quality factor decreased.

Further, *Li et al.* [63] investigated the effect of Mn doping on the magnetic properties and microstructure of the  $(\text{Ni}_{0.2}\text{Cu}_{0.2}\text{Zn}_{0.6})_{1.03}(\text{Fe}_2\text{O}_3)_{0.97}+0.97x\text{MnO}_2$  ferrites. They found that the initial permeability increased with Mn-content, but  $\text{Mn} \geq 0.4$  resulted in the formation of a second phase. The high Mn-content increased the grain size of NiCuZn ferrites that reduced the fraction of grain boundary with high resistance thereby, lowering the resistivity. *Chu et al.* [64] studied the magnetic properties of low Mn-doped NiCuZn ferrites. The results showed that with the increasing  $\text{Mn}^{2+}$  content up to  $x = 0.02$ , saturation magnetization ( $M_s$ ) of the powder samples decreased. The real part of the permeability of the toroidal specimens increased up to  $x = 0.01$ .

This cation is also used in other ferrite where, *Qi et al.* [65] prepared Mn substituted  $(\text{Mg}_{0.2}\text{Cu}_{0.2}\text{Zn}_{0.6})\text{O}(\text{Fe}_{2-x}\text{Mn}_x\text{O}_3)_{0.97}$  ferrites. They found that Mn induced higher initial permeability and lowered grain size. It also decreased magnetostriction constant in MgCuZn ferrites. *Bhaskar et al.* [66] worked on Mn substituted  $(\text{Mg}_{0.456-x}\text{Cu}_{0.144}\text{Mn}_x\text{Zn}_{0.4})\text{Fe}_2\text{O}_4$  ferrites. They found that the initial permeability and resistivity increased while magnetostriction constant decreased with Mn-content. *Bueno et al.* [67] investigated the effect of Mn-substitution on the microstructure and magnetic properties of  $(\text{Ni}_{0.50-x}\text{Zn}_{0.50-x}\text{Mn}_{2x})\text{Fe}_2\text{O}_4$  ferrites. The results indicated that Mn-substitution increased induction magnetization ( $B_m$ ) and remnant magnetization ( $B_r$ ). The lattice parameter was found to increase with increasing Mn-substitution as well. The addition of Mn enhanced the material's densification.

$\text{Co}^{2+}$  is used to improve electromagnetic properties in ferrites. *Groenou et al.* [68] prepared Co-substituted  $(\text{Ni}_{0.78}\text{Zn}_{0.22})\text{Fe}_2\text{O}_4$  ferrite. The results showed that  $\text{Co}^{2+}$  was the anisotropic ion responsible for the magnetic response time. The  $\text{Co}^{3+}$  ions and presumable cation vacancies in association with  $\text{Co}^{3+}$  provide the means whereby,  $\text{Co}^{2+}$  was transported through the lattice. *Byun et al.* [69] investigated the electromagnetic

properties of  $(\text{Ni}_{0.2}\text{Cu}_{0.2}\text{Zn}_{0.6})_{1.02-x}\text{Co}_x\text{Fe}_{1.98}\text{O}_4$  ferrites. The results showed that the grain size and sintered density changed a little. It also showed the concentration of cation vacancies increased with Co content and the increase in induced anisotropy results in the decrease of initial permeability. The magnetostriction of cobalt ferrite is many times higher than that of NiZn ferrites.

*Kulikowski et al.* [70] worked on magnetostrictive properties of  $\text{Co}_x(\text{NiZn})_{1-x}\text{Fe}_2\text{O}_4$  ferrites and shown that the magnetostrictive effect of a core was the result of the effects of the sum of the magnetostrictions of all magnetic domains. *Xiang et al.* [71] reported Co substituted  $(\text{Mn}_{0.4}\text{Zn}_{0.6-x}\text{Co}_x)\text{Fe}_2\text{O}_4$  ferrites. The results showed that the grain size, saturation magnetization and coercivity increased with increasing Co-content. *Rezlescu et al.* [72] investigated Co-substituted  $(\text{Ni}_{0.5}\text{Zn}_{0.5})\text{Fe}_2\text{O}_4$  ferrites and found that  $\text{Co}^{2+}$  ions increased the electrical resistivity due to the change in the valence state.

*Kaiser* [73] investigated Ni substitution in  $(\text{Cu}_{0.8-x}\text{Zn}_{0.2}\text{Ni}_x)\text{Fe}_2\text{O}_4$  ferrites. The results revealed that the transition (metallic to semiconductor) temperature increased with an increasing Ni concentration. *Zhong et al.* [74] reported the effects of NiO on microstructure and magnetic properties of  $(\text{Zn}_{0.32}\text{Mn}_{0.60-x}\text{Ni}_x)\text{Fe}_{2.08}\text{O}_4$  ferrites. The results showed that Ni substitution could cause the lattice constant to decline, grain size to decrease, grain structure to be more compact and porosity to decrease.

Many researchers had worked on Mg substitution in different ferrite systems and found Mg substitution has a significant effect on the structural, electrical and magnetic properties. MgO is a very stable oxide that can be used in a large range of technological applications [75]. Mg containing composition is preferred to avoid the presence of divalent iron to obtain high resistivity. With increasing Mg content only octahedral  $\text{Fe}^{2+}$  ions are substituted by  $\text{Mg}^{2+}$  and it decreased with increasing Mg content as shown in Fig. 2.2. [76]. In the iron-deficient ferrites, the dominant conduction mechanism is due to hole-hopping. At high concentration of  $\text{Mg}^{2+}$  ions, the conductivity is low due to the obstruction of  $\text{Mg}^{2+}$  ions to the hopping process between iron ions [77].

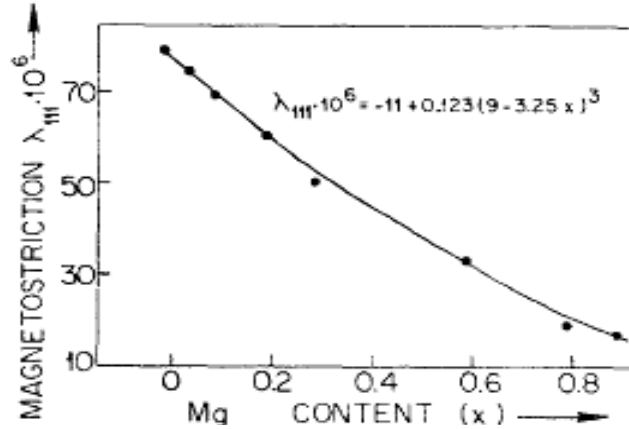


**Fig. 2.2.** Composition dependence of magnetostriction constant  $\lambda_{111}$  at 300 K [76].

Mg is also preferred to increase the rate of densification and to avoid the tendency of discontinuous grain growth [78]. It is believed that increase of initial permeability can be obtained by decreasing magnetostriction constant. Magnetostriction constant of MgCuZn ferrites is lower than that of NiCuZn ferrites [79]. MgO has low dielectric loss and low dielectric constant. It is doped with ferroelectric material for high frequency device application [80]. So, Mg containing ferrites would obtain higher magnetic properties.

*Bhosale et al.* [81] investigated the effect of Mg in MgCuZn ferrite and found that density increased and permeability decreased with  $Mg^{2+}$  content. But later they [82] reported the ferritization temperature of this system varies with increasing  $Mg^{2+}$ . It was also been found that lattice parameter decreased and density, initial permeability increased with increase  $Mg^{2+}$  content up to  $x = 0.20$  in  $(Mg_xCu_{0.5-x}Zn_{0.5})Fe_2O_4$  ferrites. *Hiti* [83] studied the effect of frequency, temperature and composition on the dielectric behavior of  $(Mg_xZn_{1-x})Fe_2O_4$  ferrites. The relaxation frequency was found to be shifted to higher values as the temperature increased.

## 2.4 Effect of Rare Earth Cation Substitution

The rare earth substituted different ferrites are becoming the promising materials for different applications. Addition of small amount of rare earth ions to ferrite samples

produces a change in their magnetic and electrical as well as structural properties depending upon the type and the amount of rare earth elements used.

Rare earth ions can be divided into two categories: one with the radius closes to Fe ions; while the other with ionic radius larger than Fe ions [84]. The difference in their ionic radii will lead to micro strains, which may cause domain wall motion resulting in deformation of the spinel structure [85]. It has been stated that the rare earth ions commonly reside at the octahedral sites by replacing  $\text{Fe}^{3+}$  ions and have limited solubility in the spinel lattice due to their large ionic radii [86].

Ferrimagnetism in ferrite is largely governed by Fe-Fe interaction (the spin coupling of the 3d electrons). If the rare earth ions enter the spinel lattice, the RE-Fe interactions also appears (4f-3d coupling), which can lead to changes in the magnetization and Curie temperature [87].

The rare earth oxides are good electrical insulators and have resistivities at room temperature greater than  $10^6 \Omega\text{-cm}$  [88]. Rare earth ion forms the orthoferrite phase ( $\text{REFeO}_3$ ). The occupation of RE ions on 'B' sites impedes the motion of  $\text{Fe}^{2+}$  in the conduction process in ferrite, thus causing an increase in resistivity [46].

Many investigations have been carried out on the influence of different rare earth atoms (La, Sm, Gd, Nd, Dy, Tb, Ce, Th, Y, Eu) on the properties of ferrites. The results of these researches show that different rare earth atoms behave differently in spinel ferrite. The effect of different rare earth cations in NiCuZn ferrite along with some different ferrites is reviewed below.

*Rezlescu et al.* [89] investigated the effect of Fe replacement by RE (Yb, Er, Sm, Tb, Gd, Dy and Ce) ions on the properties of  $(\text{Ni}_{0.7}\text{Zn}_{0.3})\text{Fe}_2\text{O}_4$  ferrite. The results showed that the electrical resistivity of a ferrite increased by substituting a small quantity of  $\text{Fe}_2\text{O}_3$  with  $\text{RE}_2\text{O}_3$ . *Sun et al.* [46] investigated the effects of rare earth ions on the properties of  $(\text{Ni}_{0.5}\text{Zn}_{0.5})\text{Fe}_{1.98}\text{RE}_{0.02}\text{O}_4$  (RE = Y, Eu or Gd) nominal compositions. The partial substitution of  $\text{Fe}^{3+}$  with a small amount of RE ions increased the electrical resistivity and relative loss factor, whereas, it slightly decreased the Curie temperature.

Results had shown that Y and Eu substitution tend to decrease  $\mu_i$  while Gd did not reduce  $\mu_i$ .

*Jacobo et al.* [90] worked on  $(\text{Zn}_{0.5}\text{Ni}_{0.5})\text{RE}_{0.02}\text{Fe}_{1.98}\text{O}_4$  ferrites, with RE = Y, Gd and Eu. The results showed a small increase in the hyperfine field parameters and a strong decrease of the total resonant area with respect to the pure NiZn ferrite. Curie temperatures decreased and coercive fields increased with substitution. By adding much large ionic radii rare earth ions resulted in local distortion and disorder, enough to induce a softening of the network (s electron density).

*Zhao et al.* [91] reported influence of Gd on magnetic properties of  $(\text{Ni}_{0.7}\text{Mn}_{0.3})\text{Gd}_x\text{Fe}_{2-x}\text{O}_4$  ferrites. It was found the crystallite sizes decreased when Gd ions were doped into NiMn ferrites. With Gd-substitution, when  $x > 0.06$  all Gd ions could not enter into the ferrite lattice but resided at the grain boundary. The maximum content of  $\text{Gd}^{3+}$  ions in ferrite lattices was substituted when  $x = 0.06$ . The values of  $H_c$  and  $M_s$  were zero for all the samples calcined at  $600^\circ\text{C}$ . In addition, the  $H_c$  and  $M_s$  values of the samples calcined at  $800^\circ\text{C}$  were larger than those sintered at  $850^\circ\text{C}$ , with Gd contents less than 0.08. Whereas, when the Gd contents at  $x = 0.08$  and  $x = 0.10$ , the  $H_c$  and  $M_s$  values of the samples increased with the calcination temperatures.

*Zhao et al.* [92] worked on the effect of substitution of  $\text{Fe}^{3+}$  by  $\text{Nd}^{3+}$  ions on structure and magnetic properties of  $\text{CoFe}_{2-x}\text{Nd}_x\text{O}_4$  ferrites. It was stated that the value of saturation magnetization for  $\text{Nd}^{3+}$  doped samples was less than that of the pure cobalt ferrite whereas, the coercivity increased with  $\text{Nd}^{3+}$  content.

*Rezlescu et al.* [93] investigated the influence of rare earth ions like Yb, Er, Dy, Tb, Gd, Sm substitution on structure, magnetic and electrical properties of  $(\text{Li}_{0.3}\text{Zn}_{0.4})\text{Fe}_{1.96}\text{RE}_{0.04}\text{O}_4$  ferrites. They found that  $\text{RE}_2\text{O}_3$  facilitated the formation of secondary phases at grain boundary which suppressed the grain growth. The results also showed that the Curie point shifted to lower temperature and increased the electrical resistivity.



*Ahmed et al.* [94] reported the electrical properties of  $(\text{Mg}_{1-x}\text{Ti}_x)\text{RE}_y\text{Fe}_{2-2x-y}\text{O}_4$  ferrites doped with rare earth ions like Er, Ce and Nd. They found that the resistivity increased by introducing rare earth ions into ferrite structure. *Ahmed et al.* [45] worked on  $(\text{Ni}_{1-x}\text{Zn}_x)\text{La}_y\text{Fe}_{2-y}\text{O}_4$  ferrite system and reported  $\text{La}^{3+}$  could not enter into the octahedral site but form small aggregates on the grain boundary.

*Sun et al.* [95] reported the effect of Fe substitution by La and Gd on the structure, magnetic, and dielectric properties of  $(\text{Ni}_{0.5}\text{Zn}_{0.5}\text{Fe}_{2-x})\text{RE}_x\text{O}_4$  ferrites. It was found that the relative density of sintered bodies decreased and the lattice parameter increased with increasing RE ion substitution. La and Gd both tend to increase the cut-off frequency, decrease the initial permeability and magnetic loss tangent ( $\tan\delta$ ) which could be explained by a combination of low density, small grain size, secondary phase ( $\text{REFeO}_3$ ) formation, and more lattice defects. The low  $\tan\delta$  values resulted mainly from the reduction in eddy current loss due to the higher electrical resistivity with increasing RE ion.

*Ahmed et al.* [87] reported the effect of rare earth ions on the structural, magnetic and electrical properties of  $(\text{Mn}_{0.5}\text{Zn}_{0.5})\text{RE}_{0.05}\text{Fe}_{1.95}\text{O}_4$  ferrites where RE = Tb, La, Ce and Th. Rare earth ion formed orthoferrite ( $\text{REFeO}_3$ ) phase and the formation of these secondary phases in ferrite during sintering process was governed by the type and the amount of  $\text{RE}^{3+}$  ion used. It was found that the molar magnetic susceptibilities for rare earth substituted samples were smaller than pure ferrite. The Curie temperature and electrical resistivity increased with increasing rare earth ions in MnZn ferrites.

*Rezlescu et al.* [38] worked on  $(\text{Mg}_{0.5}\text{Cu}_{0.5})\text{Fe}_{2-x}\text{RE}_x\text{O}_4$  ferrites, in which RE = La, Gd, Y and  $x = 0$  and  $0.2$ , respectively. XRD analysis evidenced that the compounds containing  $\text{Y}^{3+}$  and  $\text{La}^{3+}$  ions are pluri-phasic whereas, the others are mono-phasic. The electrical resistivity decreased by La and Y incorporation and increased by Gd incorporation.

*Costa et al.* [96] investigated the effect of samarium on the microstructure, relative density and magnetic properties of  $(\text{Ni}_{0.5}\text{Zn}_{0.5})\text{Sm}_x\text{Fe}_{2-x}\text{O}_4$  ferrites. Results

showed that the increased relative density and decreased average grain size with rare earth substitutions. It also showed the increase in coercive field and decrease in permeability with rare earth substitution. They also stated about the formation of secondary phase. Fig. 2.3 (a) shows a monophasic and homogeneous microstructure whereas, Fig. 2.3 (b) shows a bi-phasic microstructure constituted of a matrix of dark grains and a second phase (SmFeO<sub>3</sub>).

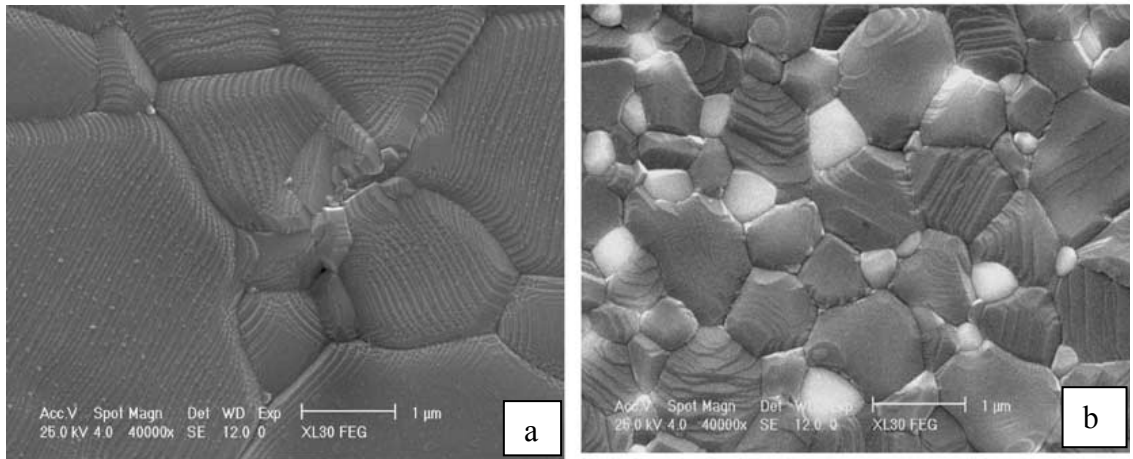


**Fig. 2.3.** Microstructure obtained by SEM after sintering at 1200°C for 2h of (Ni<sub>0.5</sub>Zn<sub>0.5</sub>)Fe<sub>2-x</sub>Sm<sub>x</sub>O<sub>4</sub> with x = a) 0.0 and b) 0.1 % mol [96].

*Sattar et al.* [97] investigated CuZn ferrites doped with rare earth ions like La, Sm, Nd, Gd, and Dy. They found that all samples were of high relative density and low porosity. The magnetization of the samples (Fig. 2.4) with Sm and La were higher than that of undoped. On the other hand, samples with Gd and Dy had lower values than that of the undoped ones. The magnetization values of the sample with Nd may be higher or lower than that of the undoped ones depending on the applied magnetizing field. The samples with La, Sm and Nd had higher values of  $\mu_r$  than that of undoped samples while those with Gd and Dy had lower values of  $\mu_r$  than that of the undoped ones. The most important result was that the relative permeability has increased by about 60%, 35.5% and 25%, in case of Sm, La and Nd, respectively.

*Mahmoud et al.* [98] studied the cation distribution and spin canting angles variation in (Cu<sub>0.5</sub>Zn<sub>0.5</sub>)Fe<sub>2</sub>O<sub>4</sub> ferrites substituted with Sm and Nd using Mossbauer

spectroscopy. They observed slight decrease in saturation magnetization  $M_s$  of the specimen doped with Nd and significant increase in  $M_s$  for the specimen doped with Sm.

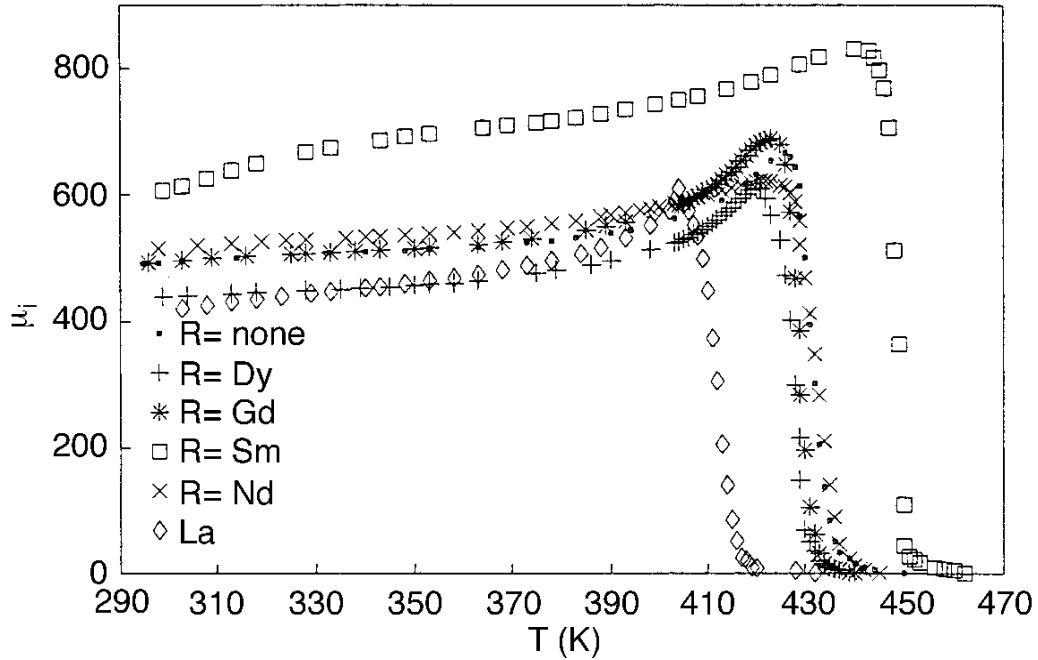


**Fig. 2.4.** Variation of initial permeability  $\mu_i$  with temperature (T) for  $(\text{Cu}_{0.5}\text{Zn}_{0.5})\text{Fe}_{2-x}\text{RE}_x\text{O}_4$  ferrites [97].

## 2.5 Effect of Sintering Aids

The sintering temperature of ferrites can be lowered by using sintering aids [99]. These additives form liquid phase which either due to the melting of the additives or eutectic liquid phase formation between the additives and ferrites. Amount of liquid phase increases with increasing amount of sintering aids those results in increased densification. But excessive amount of sintering additives will deteriorate magnetic properties of ferrites.

In addition, serving as a liquid phase to promote the densification, it is important to recognize that the additives components may also play an important role in the contribution to the magnetic properties of the sintered ferrites. Flux-sintered ferrite may not always result in the desired magnetic properties. This is primarily true if the permeability is diluted by the presence of a continuous low permeability grain boundary

phase. The chemical interaction between ferrite and additives may be detrimental to the quality factor ( $Q$ ) [100].

To obtain materials with high permeability as well as high  $Q$ , a key step is to tailor the additives composition to produce densification with limited grain growth. During the grain growth, the dissolution of the additive into the ceramic is assisted by solution re-precipitation process, which reduces the volume fraction of intergranular phases. Therefore, the compositions of the additives, melting temperature, reactions between the additives and ferrites, and microstructural evolution during the liquid-phase sintering are all very important parameters to characterize and understand any attempt to precisely control the magnetic properties [101-102].

Several researchers worked on different additives ( $V_2O_5$ ,  $MoO_3$ ,  $Bi_2O_3$ ,  $WO_3$ , Glass and  $PbO$ ) in different spinel ferrite systems to investigate the effect on lowering the sintering temperature and improving electromagnetic properties. A review on this subject is presented below.

One of the most effective additives is  $V_2O_5$ . *Hsu et al.* [99] introduced  $V_2O_5$  as sintering aids in NiCuZn ferrite to reduce the sintering temperature. They found that  $V_2O_5$  content up to 0.25 mol% improved the magnetic properties. However, a small amount of  $V^{5+}$  cations entered the crystal lattice of the ferrite and higher amount of  $V_2O_5$  deteriorated the magnetic properties. 0.5 mol% of  $V_2O_5$  was required to form the liquid phase for enhancing the densification of this composition at around 875°C.

*Yan et al.* [55] investigated the effect of CuO and  $V_2O_5$  addition on the microstructure and relative permeability of NiCuZn ferrite. They found that these additives contributed to the grain growth and densification of matrix in the sintering process. 10 mol% CuO and 0.20 mol%  $V_2O_5$  compositions showed the highest initial permeability.

*Lebourgeois et al.* [103] worked on the effect of  $V_2O_5$  on the densification of  $Ni_{0.24}Cu_{0.2}Zn_{0.55}Co_{0.02}Fe_{1.99}O_4$  ferrite. They found that with small amount of  $V_2O_5$  (0.6–1.2 wt%) as a sintering aid was enough for densification at around 850°C. EDX analyses

showed the presence of vanadium inside the ferrite grains. Magnetic properties were deteriorated with increasing the  $V_2O_5$  content. The permeability decreased and the core losses increased for  $V_2O_5$  content higher than 0.6 wt%. It was shown that  $V_2O_5$  content 0.20-0.25 mol% (~0.15-0.20 wt%) improved electromagnetic properties in NiCuZn ferrite.

*Mirzaee et al.* [104] investigated the influence of  $V_2O_5$  on the microstructure development and magnetic properties of  $(Ni_{0.64}Zn_{0.36})Fe_2O_4$  ferrites. The results showed that the permeability, relative density and grain size initially increased up to 1.6 wt% and then decreased with further addition. The specific resistivity increased continuously. The Curie temperature and saturation magnetization showed peak values at 0.8 wt% and 1.2 wt% of  $V_2O_5$ , respectively. *Mirzaee et al.* [105] also worked on the influence of  $MoO_3$  and  $V_2O_5$  co-doping on the magnetic properties and microstructure of NiZn ferrites. The results showed that 0.05 wt% of  $MoO_3$  in addition to 0.2 wt% of  $V_2O_5$  increased grain size and sintered density and also decreased power loss noticeably.

Another important sintering aid is  $MoO_3$ . *Seo et al.* [106] focused on the effect of  $MoO_3$  addition on the sintering behavior and magnetic properties of  $(Ni_{0.2}Cu_{0.2}Zn_{0.6})_{1.02}(Fe_2O_3)_{0.98}$  ferrite. Results showed that  $MoO_3$  addition reduced the sintering temperature and magnetic loss of NiCuZn ferrite and it also increased the bulk density and initial permeability (Fig. 2.5) up to the additives content of 0.2 wt %.

*Su et al.* [20] was investigated on the amount of CuO contained in NiZn ferrite and a small additive of  $MoO_3$  added in  $(Ni_{0.29}Cu_{0.08}Zn_{0.62})(Fe_2O_3)_{1.01}$  ferrite. Results showed that the initial permeability of the core increased but the Curie temperature decreased a little with 4 mol% CuO content. The highest initial permeability  $\approx 2480$  and relatively higher Curie temperature  $\approx 118^\circ C$  could be obtained at 0.12 wt%  $MoO_3$  additive in NiCuZn ferrite.

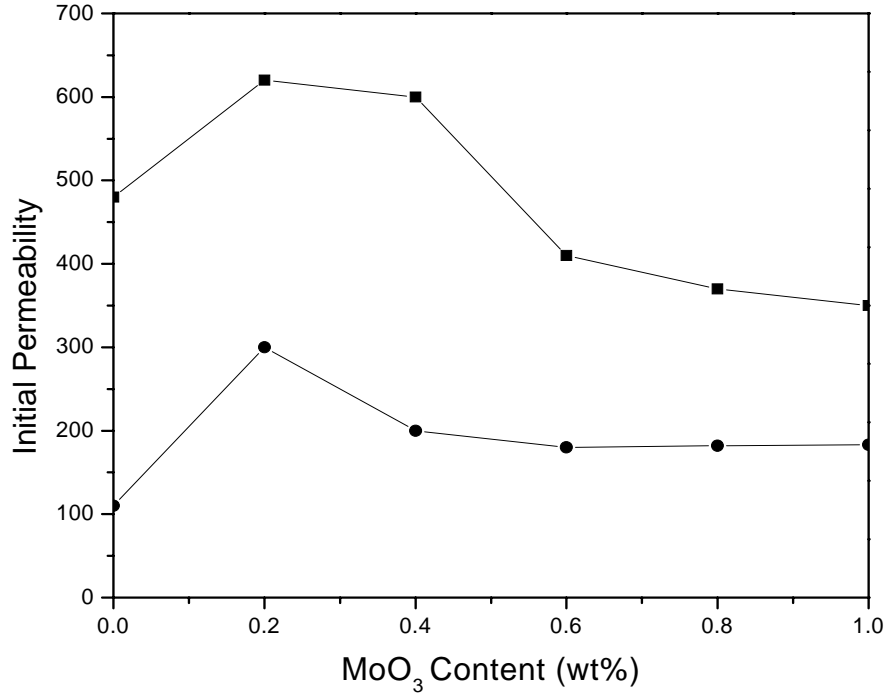


**Fig. 2.5.** Initial permeability of  $(\text{Ni}_{0.2}\text{Cu}_{0.2}\text{Zn}_{0.6})_{1.02}(\text{Fe}_2\text{O}_3)_{0.98}$  ferrite with addition of  $\text{MoO}_3$  (wt %) sintered at  $900^\circ\text{C}$  and  $850^\circ\text{C}$  for 5hrs (■:  $900^\circ\text{C}$ , ●:  $850^\circ\text{C}$ ) [106].

*Gu et al.* [107] reported the effect of  $\text{MoO}_3$  and  $\text{TiO}_2$  additions on the magnetic properties of MnZn ferrite. It was found that the magnetic properties of MnZn power ferrites fluctuate with the increase of  $\text{MoO}_3$  content and could be considerably improved with suitable amount of  $\text{MoO}_3$  addition. The sample doped with 600 ppm  $\text{MoO}_3$  had a decreased power loss of 13.5%, and increased initial permeability of 7.2% than undoped samples.

Another most interesting sintering aid is  $\text{Bi}_2\text{O}_3$ . *Hsu et al.* [13] reported  $\text{Bi}_2\text{O}_3$  and lead glass as sintering aids for NiCuZn ferrite. Results showed that both additives formed liquid phases in the grain boundaries during the sintering process to enhance the densification. But  $\text{Bi}_2\text{O}_3$  exhibited better effect than the lead glass to lower the sintering temperature.

*Wang et al.* [108] worked on the mixing of  $(\text{Ni}_{0.38}\text{Cu}_{0.12}\text{Zn}_{0.50})\text{Fe}_2\text{O}_4$  powders with  $\text{Bi}_2\text{O}_3$  using the solid-state mixing as well as wet chemical coating processes such as ammonia precipitation coating, urea precipitation coating, and solution coating. Ferrites

prepared from the wet chemical coating processes could be densified at a lower sintering temperature without significant impact on the micro structural evolution compared with that prepared by solid-state mixing. In addition, samples prepared from the wet chemical coating process have a higher  $B_r$  and  $B_m$  and a lower  $H_c$  compared with that from the solid-state mixing process. Considering both effects of sintering temperature and sintered density (>95% theoretical density), ferrites with 1.5 wt%  $\text{Bi}_2\text{O}_3$  addition by ammonia precipitation coating process followed by sintering at around 900°C could provide the best permeability and quality factor.

*Jeong et al.* [109] investigated the effect of  $\text{Bi}_2\text{O}_3$  addition on the microstructure and electromagnetic properties of NiCuZn ferrites. The grain size and bulk density gradually increased with the increase in  $\text{Bi}_2\text{O}_3$  content. Above 0.5 wt%  $\text{Bi}_2\text{O}_3$ , abnormal grain growth was observed. Specimen with 0.25 wt% of  $\text{Bi}_2\text{O}_3$  showed the highest initial permeability with good quality factor and a uniform microstructure.

*Su et al.* [110] investigated the effects of mixed  $\text{Bi}_2\text{O}_3$ – $\text{WO}_3$  additives. The results showed that appropriate additives of mixed  $\text{Bi}_2\text{O}_3$ – $\text{WO}_3$  could enhance densification of the specimens, improve the initial permeability and the  $Q$ -factor of NiCuZn ferrites. The maximum initial permeability was achieved with 1.5 wt%  $\text{Bi}_2\text{O}_3$  and 0.3 wt%  $\text{WO}_3$  additives.

*K. Kawano et al.* [111] fabricated Bi, Si oxides-doped NiZnCu ferrite composite materials. Analysis showed that the composite materials has mainly NiCuZn ferrite and  $\text{Bi}_4(\text{SiO}_4)_3$  phases. The optimum percentage of  $\text{Bi}_2\text{O}_3$  content to improve the electromagnetic properties in NiCuZn ferrite is 0.25 wt%. *Kong et al.* [112] reported the effects of concentration of  $\text{Bi}_2\text{O}_3$  on  $\text{MgFe}_{1.98}\text{O}_4$  ferrite. It was found that 3 wt%  $\text{Bi}_2\text{O}_3$  could result in fully sintered ferrite. Low concentration of  $\text{Bi}_2\text{O}_3$  increased the static permeability of the ferrite owing to the improved densification and grain growth, while too high concentration led to decrease in permeability owing to the incorporation of the non-magnetic component ( $\text{Bi}_2\text{O}_3$ ) and retarded grain growth.

A few authors also worked on  $\text{WO}_3$  as sintering aid. Earlier, *Park et al.* [113] investigated the effect of  $\text{WO}_3$  addition on the magnetic properties of NiCuZn ferrites. The results showed that enhanced electrical and magnetic properties obtained from  $\text{WO}_3$  addition upto 0.6 wt% into NiCuZn ferrites. Later, *Su et al.* [110] reported that appropriate  $\text{WO}_3$  additive could improve grain size of the specimen and removed closed pores.

Recently, *Su et al.* [114] studied the effects of  $\text{WO}_3$  addition on properties of NiCuZn ferrites. The results showed that to obtain a single-phase spinel ferrite  $\text{WO}_3$  addition should be less than 0.28 wt%. With proper  $\text{WO}_3$  addition, the average grain size and the initial permeability of the ferrites increased. The maximum initial permeability was observed at a  $\text{WO}_3$  content of 0.16 wt%.

Lead oxide and glass also act as sintering aid in NiCuZn ferrites. Earlier, *Jean et al.* [9] investigated the effect of PbO addition on the densification, microstructural properties of NiCuZn ferrites. Results showed that with a small amount of PbO (0.5-2 wt%) in NiCuZn ferrite increased the densification rate and final sintered density when the activation energy of densification was significantly reduced. However, interfacial reaction causes segregation of CuO onto the grain boundary and dissolution of PbO into the ferrite grains, yielding a reduction in initial permeability.

Later, *Wang et al.* [115] used PbO-SiO<sub>2</sub>, PbO-B<sub>2</sub>O<sub>3</sub> and Bi<sub>2</sub>O<sub>3</sub> flux systems to lower the sintering temperature of (Ni<sub>0.38</sub>Cu<sub>0.12</sub>Zn<sub>0.50</sub>)Fe<sub>2</sub>O<sub>4</sub> ferrite and found that the PbO-SiO<sub>2</sub> glass system to be the most effective additive to obstruct the grain boundary movement and prevent the exaggerated grain growth among these flux systems. Ferrites sintered with PbO-SiO<sub>2</sub> possess higher resistivity, higher  $Q$  and higher  $H_c$  compared with those obtained using other systems. The results also showed that the addition of Bi<sub>2</sub>O<sub>3</sub> considerably deteriorated the quality factor of NiCuZn ferrites, though benefited the densification and permeability.



## 2.6 Summery and Scope of Work

The extensive literature survey reveals that the synthesis of nano-crystalline NiCuZn ferrite powder through sol-gel auto combustion method has been attempted by number of researchers. The temperature at which the ferrite is sintered critically depends on the chemical composition. The electromagnetic properties such as permeability and resistivity are dependant on the densification and microstructure of the ferrite. Substitutions and addition of sintering aids in ferrites have been used as attractive approaches to enhance the electromagnetic properties.

Various compositions in the system  $(\text{Ni}_{1-x-y}\text{Zn}_x\text{Cu}_y)\text{Fe}_2\text{O}_4$  were investigated. Cu is used in this ferrite to decrease the sintering temperature so that it can be co-fired with Ag internal electrode. However, Cu decreases the resistivity of the ferrite, which is not desirable for its high frequency applications. So, optimization of Cu content with respect to densification and resistivity of the ferrite is very important. Many reports are available on the effect of Cu in NiCuZn ferrites [5, 53-54]. *Nam et al.* [5] reported an optimum Cu content (10 mol%) at which the resistivity of NiCuZn ferrite was maximum. This optimum Cu content was used by various other researchers for the NiCuZn ferrites.

Different ranges of electromagnetic properties have been reported with various Zn concentrations in NiCuZn ferrites [22, 44]. Optimization of Zn concentration with respect to Ni and Cu is essential to achieve desirable electromagnetic properties in the ferrites.

One of the key parameters to increase the permeability in spinel ferrite is lowering the magnetostriction constant. As the magnetostriction constant of MgCuZn ferrite is lower than NiCuZn ferrite [79] and decreased with increasing Mg content [76]. Mg can be substituted for Ni to increase the permeability in NiCuZn ferrite. Mg containing compositions were also preferred to avoid the presence of divalent iron (to obtain high resistivity) and to avoid the tendency of discontinuous grain growth [78]. All these suggest that, the Mg substitution may improve the electromagnetic properties in NiCuZn ferrite.

Influence of rare earths on the properties of different ferrites has been reported [38, 89-98]. The investigations showed an improved densification in NiZn [96] and increased permeability in CuZn ferrite [97] by Sm substitution. La substitutions showed an improved resistivity in NiZn ferrites [95]. Similarly, these substitutions may improve the electromagnetic properties in NiCuZn ferrites.

$V_2O_3$ ,  $MoO_3$  and  $Bi_2O_3$  were reported to be the most widely used sintering additives for the ferrites [99, 106 and 109]. *Su et al.* [110] and *Mirzaee et al.* [105] reported that  $Bi_2O_3$ - $WO_3$  and  $V_2O_5$ - $MoO_3$  mixed additives were better than the individual additives in NiCuZn ferrite, respectively. Further research is needed on the mixed sintering additives in the system  $V_2O_5$ ,  $Bi_2O_3$  and  $MoO_3$  for the ferrites.

## 2.7 Objectives of Present Work

The general observations are; (a) the Cu concentration of the ferrite will be fixed at composition  $(Ni_{0.8-x}Cu_{0.2}Zn_x)Fe_2O_4$  and (b) the ferrite materials will be synthesized through auto-combustion method. The influence of substitutions and sintering aids on electromagnetic properties of the ferrite will be studied with following objectives.

The objectives of the present study are:

- a) Optimization of  $Zn^{2+}$  concentration in  $(Ni_{0.8-x}Cu_{0.2}Zn_x)Fe_2O_4$  ferrite ( $0.45 \leq x \leq 0.6$ ).
- b) Study the effect of  $Mg^{2+}$  substitution for  $Ni^{2+}$  on electromagnetic properties of the optimized NiCuZn ferrite that obtained in objective (a).
- c) Analyze the effects of  $La^{3+}$  and  $Sm^{3+}$  substitutions for  $Fe^{3+}$  on electromagnetic properties of the optimized NiCuZn ferrite.
- d) Study the effect of sintering aids namely,  $Bi_2O_3$ ,  $MoO_3$  and  $V_2O_5$  on densification and electromagnetic properties in optimized NiCuZn ferrite.

# *Chapter III*

## *Experimental Work*

### 3.1 Synthesis of Ferrite Powder

Ferrite powders were prepared by sol-gel auto combustion method. Analytical grade Nickel Nitrate  $[\text{Ni}(\text{NO}_3)_2 \cdot 6\text{H}_2\text{O}]$ , Magnesium Nitrate  $[\text{Mg}(\text{NO}_3)_2 \cdot 6\text{H}_2\text{O}]$ , Zinc Nitrate  $[\text{Zn}(\text{NO}_3)_2 \cdot 6\text{H}_2\text{O}]$ , Copper Nitrate  $[\text{Cu}(\text{NO}_3)_2 \cdot 3\text{H}_2\text{O}]$ , Iron Nitrate  $[\text{Fe}(\text{NO}_3)_3 \cdot 9\text{H}_2\text{O}]$ , Citric Acid  $[\text{C}_6\text{H}_8\text{O}_7 \cdot \text{H}_2\text{O}]$  were used as raw materials in auto combustion method. All the chemicals were from E-mark, India (GR grade with 99.9% purity). 0.5 M metal nitrate solution of each nitrate salt was prepared and kept separately. Before synthesis, chemical analyses of solutions were carried out to see the actual metal ion concentration. Each analysis is described below.

#### 3.1.1 Chemical Analysis of Raw Material

##### Nickel Nitrate:

10 ml 0.5 M nickel nitrate solution was taken into a 250 ml conical flask. 5 ml (Borax- $\text{NH}_4\text{Cl}$ ) buffer solution and a pinch of Muroxide Indicator were added into that solution. The mixture was shaken well to get a yellow solution. Then the solution was titrated against standard ethylene di-amine tetra acetic acid (EDTA) solution to perfect violet end point.

Amount of  $\text{Ni}^{2+}$  (gm/ml):

$$\frac{\text{Volume of EDTA} * \text{Zn equivalent of EDTA} * \text{Atomic weight of Ni}}{\text{Volume of test solution} * \text{Atomic weight of Zinc}} \quad (3.1)$$

##### Copper Nitrate:

10 ml (N/10) Mohr solution (ferrous ammonium sulfate), 20 ml water and 5 ml 40%  $\text{NH}_4(\text{SCN})$  solution were taken in a 250 ml conical flask. The colour of the mixture was red. This red colour was discharged by careful addition of  $\text{Hg}_2(\text{NO}_3)_2$  solution. 10 ml 0.5 M copper nitrate solution was added into it; as a result the solution was red in colour again. This red colour was titrated against standard  $\text{Hg}_2(\text{NO}_3)_2$  solution to become colourless end point.

Amount of  $\text{Cu}^{2+}$  (gm/ml):

$$\frac{\text{Volume of } \text{Hg}_2(\text{NO}_3)_2 * \text{Strength of } \text{Hg}_2(\text{NO}_3)_2 * \text{Atomic weight of Cu}}{\text{Volume of test solution}} \quad (3.2)$$

**Iron Nitrate:**

10 ml 0.5 M iron nitrate solution was taken in 5 ml 40% NH<sub>4</sub>(SCN) solution. The colour of the mixture was blood red. Then standard Hg<sub>2</sub>(NO<sub>3</sub>)<sub>2</sub> solution was added slowly with constant stirring. Near the end point Hg<sub>2</sub>(NO<sub>3</sub>)<sub>2</sub> was added very carefully to avoid over titration upto a end point when the dark red color become colorless due to the reduction of Fe<sup>3+</sup> to Fe<sup>2+</sup>.

Amount of Fe<sup>3+</sup> (gm/ml):

$$\frac{\text{Volume of Hg}_2(\text{NO}_3)_2 * \text{Strength of Hg}_2(\text{NO}_3)_2 * \text{Atomic weight of Fe}}{\text{Volume of test solution} * \text{Atomic weight of Zinc}} \quad (3.3)$$

**Zinc Nitrate:**

Two test tubes deionized water was taken in a 250 ml conical flask. 10 ml (NH<sub>4</sub>OH+NH<sub>4</sub>Cl) buffer solution and a pinch of Solochrome Black-T indicator were added into that solution. The colour of the solution was not perfectly blue. The EDTA solution was added drop wise up to perfect blue colour. 10 ml 0.5 M zinc nitrate solution was added and the colour of the solution became wine red. This red solution was titrated with standard EDTA solution to perfect blue end point.

Amount of Zn<sup>2+</sup> (gm/ml):

$$\frac{\text{Volume of EDTA} * \text{Zn equivalent of EDTA} * \text{Atomic weight of cation}}{\text{Volume of test solution} * \text{Atomic weight of Zinc}} \quad (3.4)$$

**Magnesium Nitrate:**

Magnesium nitrate was also analyzed as zinc nitrate.

**3.1.2 Sol-Gel Auto Combustion Synthesis**

The sol gel auto combustion synthesis process was used to syntheses pure and substituted NiCuZn ferrites. This process has the advantages of inexpensive precursors, low external energy consumption, a simple preparation method as well as simple equipment requirement that result into nano-sized, homogeneous, highly reactive powders [33]. Auto combustion synthesis, also called self-propagating synthesis, was initially developed in Russia by Merzhanov and had been successfully used to speed up the synthesis of complex oxide material such as ferrites and high temperature superconductors [116].

Combustion synthesis offers a unique synthesis route via a highly exothermic redox reaction between metal nitrates and an organic fuel to produce multi-element oxides. Instead of using a high temperature furnace to supply the energy needed to react the component oxides, the auto combustion reaction itself supplies the energy. Metal nitrates and an organic fuel are mixed in water to form an aqueous solution, a method that maximizes molecular mixing of the components. The solution is then heated to transform into gel.

Upon ignition, the dried gel burns in a self-propagating combustion manner until all gels are completely burnt out. The reaction is self-propagating and is able to sustain this from 1 to 5 seconds typically, to form the desired product. This technique produces a homogenous product in a short amount of time without the use of expensive high temperature furnaces. A combustion synthesis reaction can be influenced by parameters such as the type of fuel, the fuel-to-oxidizer ratio (f/o), the water content of the precursor mixture and the ignition temperature. The fuel to oxidizer ratio also plays a critical role in influencing the reaction. A way to control the flame temperature of the reaction is by varying the amount of fuel to oxidizer.

The elemental stoichiometric coefficient,  $\phi_e$ , is used to control the ratio of fuel to oxidizer in the reaction and is expressed as [117]:

$$\phi_e = \frac{\sum \text{Total valencies of oxidizing elements in the nitrates and fuel}}{(-1)\sum \text{Total valencies of reducing elements in the nitrates and fuel}} \quad (3.5)$$

$\phi_e$  represents the ratio between the oxidizing and reducing components of the metal-nitrate/fuel mixture. When  $\phi_e = 1$ , the reaction is stoichiometric. When  $\phi_e < 1$ , the metal-nitrate/fuel mixture is fuel rich where as if  $\phi_e > 1$ , the mixture is fuel lean and the mixture does not have enough fuel for the reaction to go to completion.

Fig. 3.1 shows the auto combustion synthesis flow diagram that was used for the synthesis of the ferrite powders. Ferrite powder was synthesized by an amount of 20 gm per batch. Briefly to prepare 20 gm  $(\text{Ni}_{0.25}\text{Cu}_{0.2}\text{Zn}_{0.55})\text{Fe}_2\text{O}_4$  ferrite, 0.0208 mol nickel nitrate, 0.0166 mol copper nitrate, 0.0460 mol zinc nitrate and 0.1672 mol iron nitrate were taken. Total metal mol present in solution was 0.2506

mol. Equal molar citric acid i.e. 0.2506 mol was added into that solution after complete mixing of all metal nitrates solutions (Fig. 3.2 (a)).

In Mg, La, Sm substituted NiCuZn ferrites, required amount of substituents were added before citric acid addition in solution. The mixture, placed in a glass beaker, was homogenized by continuous stirring. The pH of the solution was adjusted to 7 using ammonia solution and then heated on a hot plate at 80°C. With continuous heating it initially transformed into sol than gel (Fig. 3.2 (b)).

The dried gel was placed in a hot plate at 200°C. Upon ignition, dried gel burnt in a self-propagating combustion manner until all gels were completely burnt out to form a fluffy loose structure as shown in Fig. 3.2 (c). The fluffy material was ground to get ferrite powder (Fig. 3.2 (d)). The as-burnt ash was calcined at 700°C for 2 hrs to get better crystallization and homogeneous cation distribution in the spinel and finally ground to get NiCuZn ferrite powders.

## **3.2 Dried Gel and Powder Characterization**

### **3.2.1 Thermal Analysis**

The dried gel was characterized by differential thermal analysis (DTA) and thermo gravimetric analysis (TGA) using NETZSCH STA (Model No 409C). This technique is excellent for determining the presence and quantity of hydrated water, to get an idea about decomposition behavior, phase transitions, formation of products, etc. of precursor powders synthesized through different chemical route.

Thermal analysis of dried gel was carried out in air atmosphere with the heating rate of 10°C/min. When a material undergoes physical or chemical change it absorbs or releases thermal energy. The temperature difference of the sample with respect to the reference inert material ( $\alpha$ -Al<sub>2</sub>O<sub>3</sub>) during heating or cooling is plotted in a DTA curve as the deviation from zero base line.

Exothermic or endothermic changes are shown in opposite directions of the baseline. TGA is a simple analytical technique that measures the weight loss (or weight gain) of a material as a function of temperature. As materials are heated, they can lose weight due to drying, or from chemical reactions that liberate gasses. Some materials can gain weight by reacting with the atmosphere in the testing environment.

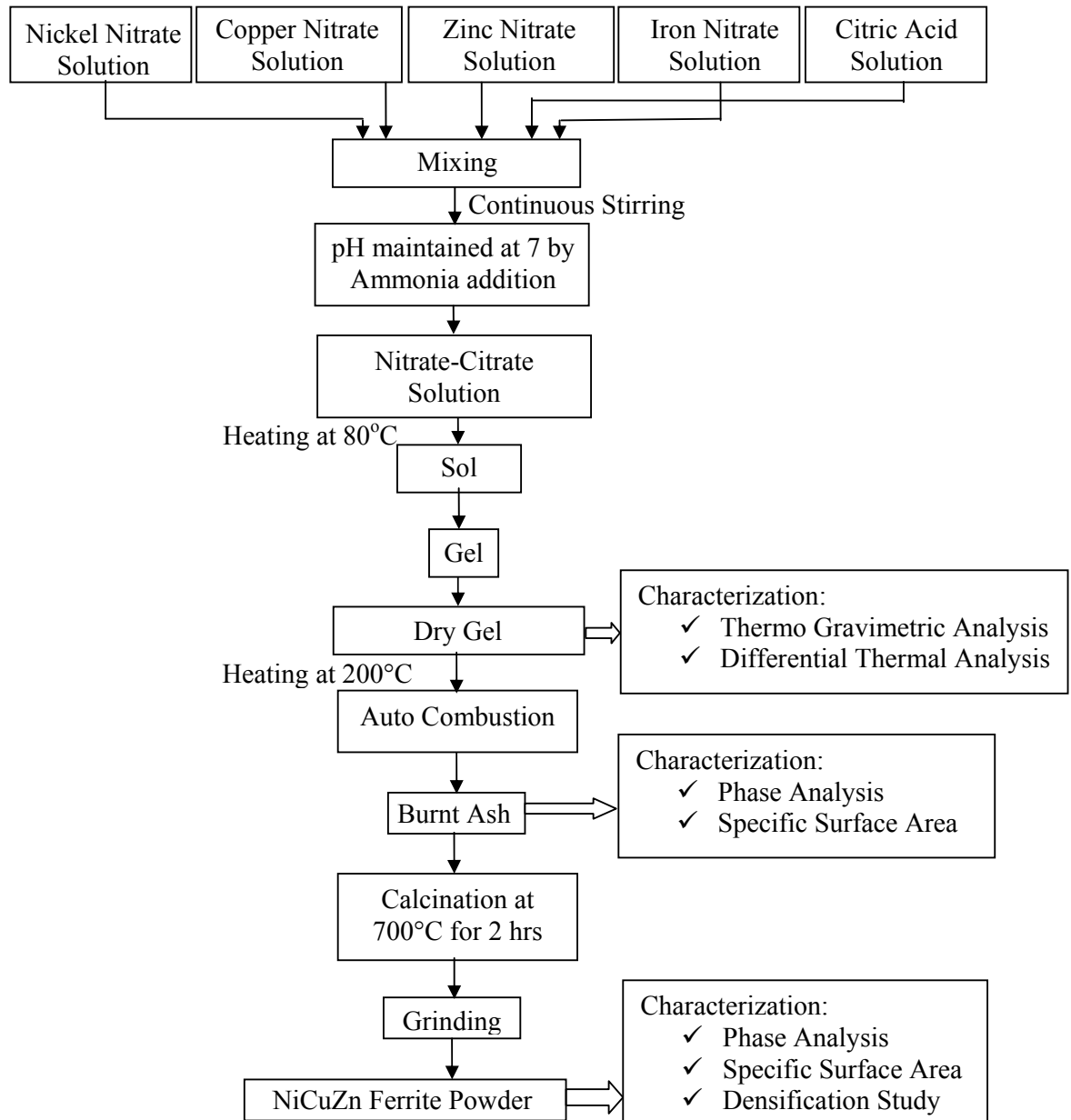


**Fig. 3.1.** Flow diagram for auto combustion synthesis of NiCuZn ferrite powder.

### 3.2.2 Phase and Crystallite Size Analysis

Phase formation of as burnt and calcined ferrite powder samples were studied by the powder X-ray diffraction performed with a Philip's Diffractometer (model: PW-1830, Philips, Netherlands). In the powder, thousands of grains have random orientations. With random orientations, it is expected that most of the different atomic planes lie parallel to the surface in some of the grains. Thus, scanning



through different angles would be associated with different atomic spacings. A powdered sample is packed on a sample stage so that it can be irradiated by the X-ray.



**Fig. 3.2.** Photograph of (a) nitrate-citrate solution, (b) dry gel, (c) auto combustion Reaction and (d) burnt ash powder.

To detect the diffracted X-rays, an electronic detector is placed on the other side of the sample from the X-ray tube, and rotated the sample through different Bragg's angles. The goniometer keeps track of the angle ( $\theta$ ), and the detector records the detected X-rays in units of counts/sec and sends this information to the computer. The operating parameters were; 40 kV and 35 mA with the Cu target, a step size of 0.02 (degree) and a count time of 4 s per step. After scan of the sample, the X-ray intensity (counts/sec) was plotted against the angle theta ( $2\theta$ ). The angle ( $2\theta$ ) for each diffraction peak was then converted to  $d$ -spacing, using the Bragg's law;  $n\lambda = 2d \sin\theta$ , where  $\lambda$  is the wave length of x-ray and  $n$  is order of diffraction.

The identification of different phases was carried out by Hanawalt method using Philips X-pert high score software. The powder pattern is characterized by a set of line position  $2\theta$  and a set of relative line intensities  $I$ . But the angular

positions of the lines depend on the wavelength used, and a more fundamental quantity is the spacing  $d$  of the lattice planes forming each line. Each pattern is described by listing the  $d$  and  $I$  values of its diffraction lines. Each substance is characterized by the  $d$  values of its 3 strongest lines. The  $d$  values together with the relative intensities are sufficient to characterize the pattern of an unknown crystal structure [118].

The crystallite sizes of the as burnt and calcined powder samples were determined from X-ray line broadening using the Sherrer's equation [118] as follows:

$$t = \frac{0.9\lambda}{B\cos\theta} \quad (3.6)$$

where,  $t$  is the crystallite size,  $\lambda$  is the wavelength of the radiation,  $\theta$  is the Bragg's angle and  $B$  is the full width at half maximum. Line broadening due to instrument was subtracted from the peak width before calculating the crystallite size using the following formula:

$$B^2 = B_{\text{meas}}^2 - B_{\text{equip}}^2 \quad (3.7)$$

where,  $B_{\text{meas}}$  = measured full width at half maximum from peak,  $B_{\text{equip}}$  = instrumental broadening [Standard Silicon sample was used, whose  $B$  value was 0.09821 at  $2\theta = 29^\circ$  with  $(hkl)$  value (111)].

Lattice parameters were determined using following relationship for cubic spinel structure:

$$a^2 = \frac{\lambda^2 (h^2 + k^2 + l^2)}{4\sin^2\theta} \quad (3.8)$$

where, ' $a$ ' is lattice parameter, ' $\lambda$ ' is the wavelength of the radiation, ' $\theta$ ' is the Bragg's angle and  $(hkl)$  is Miller index.

### 3.2.3 Surface Area

Surface area of ceramic powder is an important parameter to predict sintering characteristics. This can be measured by BET (Brunauer, Emmet and Teller

after the developers of the basic calculations) method. The BET method involves adsorbing a monolayer of nitrogen gas onto the surface of particles, then measuring the amount of nitrogen that is released when that monolayer is vaporized. Based on this nitrogen quantity, the surface area of the sample can be calculated from the BET equation:

$$\frac{1}{V_g} \frac{x}{1-x} = \frac{c-1}{cV_m} + \frac{1}{cV_m} \quad (3.9)$$

where,  $V_g$  = volume of gas adsorbed,  $V_m$  = volume of gas adsorbed at monolayer coverage,  $x = P/P_o$ ,  $P$  = Ambient pressure,  $P_o$  = Total pressure,  $c$  = a constant that is related to the heat of adsorption. A plot of  $\{(1/V_g)(x/(1-x))\}$  versus  $x$  gives a straight line with slope =  $m = (c-1)/(cV_m)$ , Intercept =  $g = 1/cV_m$ . The value of  $V_m$  and  $c$  are worked out,  $V_m = 1/(\text{slope} + \text{intercept})$ . This is normalized by the mass of particles tested to give a specific surface area ( $\text{m}^2/\text{gm}$ ).

Specific surface area of as burnt and calcined ferrite powders was determined using Quantachrome Autosorb (Model No: Nova 1200 BET). About 2-3 gm of sample was taken in the sample cell and degassed at  $110^\circ\text{C}$  in vacuum up to a maximum of 3 mbar. The sample holder mouth was closed by a stopper. Sample was cooled and the cell was placed in liquid nitrogen bath. The equipment measured the amount of gas adsorbed on the surface of the sample and the specific surface area was calculated.

### 3.2.4 Densification Study

Densification kinetics of compact samples was investigated by NETZSCH dilatometer model DIL 402 C. In the dilatometer the specimen is kept in a specimen holder in the centre of the furnace. The linear dimensional change i.e. shrinkage or expansion of the specimen is transmitted through the push rod (pressed against the sample inside the furnace) to the measuring head. The inductive displacement transducer details the change in length and produces an analogue signal through a measuring amplifier. The digitally displayed signal is in analogue form on a recorder.

Samples were made in the form in the rods having diameter 6 mm and length 20 mm for dilatometer experiment. The heating rate was maintained at

10°C/min. The measurement was carried out from room temperature to 1000°C in air atmosphere.

### 3.3 Fabrication and Sintering of Ferrite Parts

#### 3.3.1 Fabrication

The calcined powder of each batch was thoroughly mixed with 3 wt% binder (Polyvinyl alcohol) and was processed as per the flow chart (Fig 3.3).

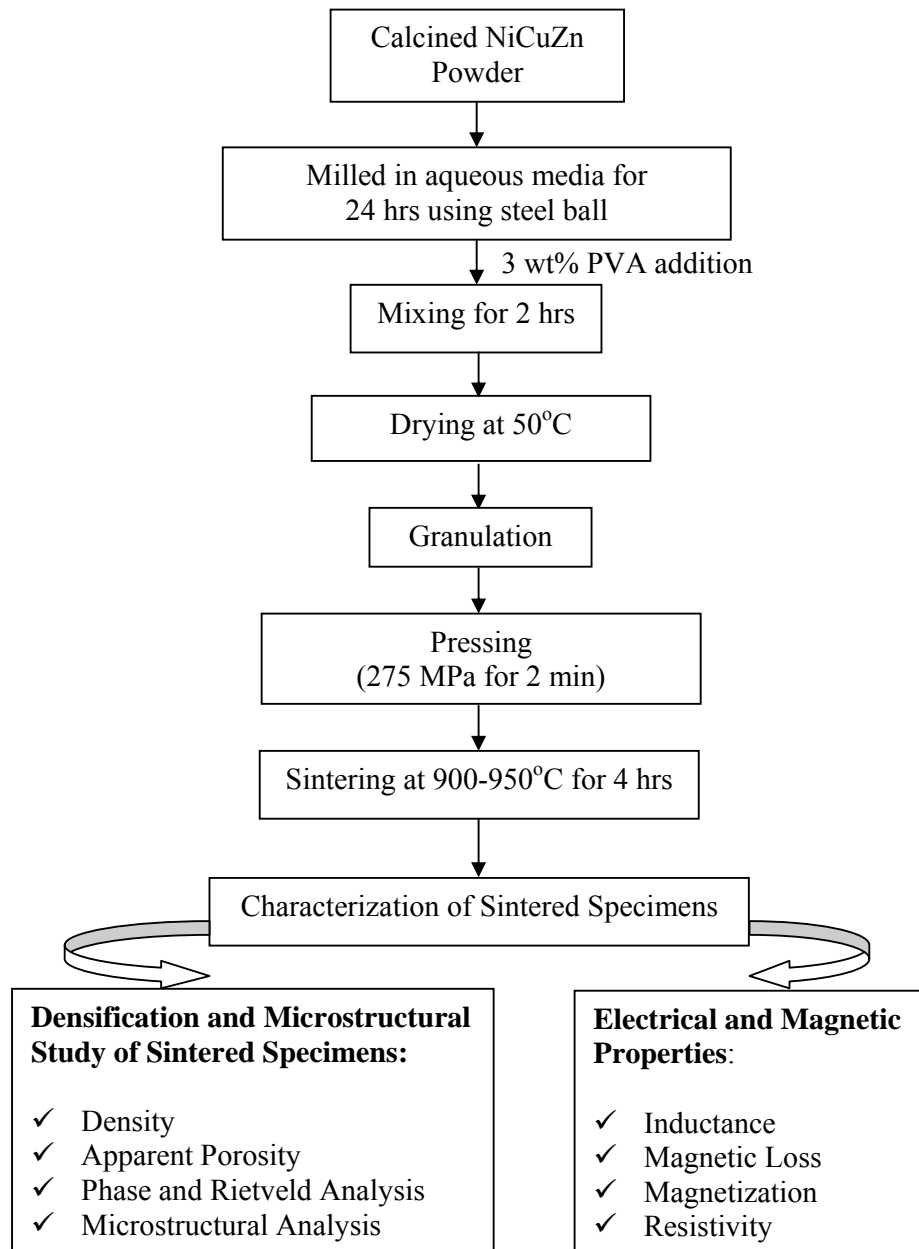


**Fig. 3.3.** A flow chart of fabrication and characterization for sintered ferrite parts.

Initially, the powders were wet milled for 24 hours using high purity iron balls and water media. In case of sintering additive experiment, additives were added with the calcined powders before wet milling. Then PVA binder was added and mixed for another 2 hrs. The mixed powder was dried and granulated. The granules were uniaxially pressed using a hydraulic press at a pressure of 275 MPa for 2 minutes to form pellets ( $D_o$ -15 mm, thickness-2 mm) and torroids ( $D_o$ -15 mm,  $D_{in}$ -6 mm, thickness 2 mm). Green densities were calculated from weight/volume ratio. Weight was measured using electronic balance whereas, volume was calculated from the dimension of the specimens.

### 3.3.2 Sintering

The pressed samples were sintered in an electrical furnace with super kanthal ( $MoSi_2$ ) heating elements and alumina insulation boards as chamber walls (size of the chamber 250x150x150 mm). The thermal regime of the furnace was controlled through a “Eurotherm” programmer-cum-controller within  $\pm 2^\circ C$  accuracy. Fig. 3.4 shows the typical sintering profile. The compacted samples heated from room temperature to  $400^\circ C$  at a rate  $1^\circ C/min$  followed by a soaking at  $400^\circ C$  for 2 hrs for binder burnout. Thereafter, the samples were heated at a rate  $3^\circ C/min$  to final sintering temperature  $900-950^\circ C$  with a soaking time of 4 hrs. Then the specimen was cooled at a rate  $3^\circ C/min$  to room temperature.

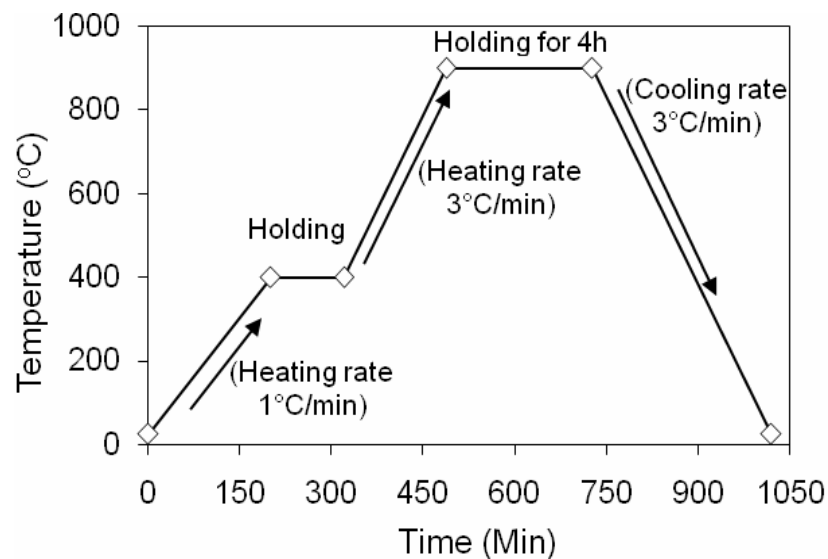


**Fig. 3.4.** A typical sintering profile of ferrite specimens at  $900^\circ C$  for 4 hrs.

### 3.4 Characterization of Sintered Specimens

The physical properties, such as density, apparent porosity, phase analysis, structural refinement and microstructural analysis of sintered samples were performed. The electrical and magnetic properties were also characterized for the sintered pellets and torroids.

#### 3.4.1 Density and Apparent Porosity

Bulk density and apparent porosity of sinter specimens were determined by Archimedes principle. Sintered samples were weighted in dry state. Samples were immersed in water and kept under a vacuum of 4 mm of mercury for 5 hrs to ensure that water filled up the open pores completely. Then, soaked and suspended weights were measured. The apparent porosity and bulk density were calculated as follows:

Dry weight of the sample =  $W_d$ , Soaked weight of the sample =  $W_s$ , Suspended weight of the sample =  $W_a$

$$\% P_{\text{App}} = \frac{W_s - W_d}{W_s - W_a} \times 100 \quad (3.10)$$

$$D_{\text{bulk}} = \frac{W_d}{W_s - W_a} \quad (3.11)$$

Relative density of different sintered specimens was calculated from the bulk density and theoretical density (obtained from X-ray method). The macroscopic density of a particular specimen, determined from the weight and volume of the specimen, is usually less than, and can not exceed the X-ray density, because the macroscopic specimen will usually contain minutes cracks and pores. Therefore, it is important to determine X-ray density. By comparing X-ray density with the macroscopic density of the sintered compacts, the true porosity can be calculated. X-ray density is sometimes also called ‘theoretical density’. However, it is not theoretical because it is determined experimentally. X-ray diffraction allows us to determine the lattice parameters of a crystal’s unit cell, and therefore its volume, together with number of atoms in the cell. So, the base for the density determination should be a single unit cell by defining [118] the X-ray density = weight of atoms in unit cell/ volume of unit cell and expressed as follows:

$$b = \frac{\Sigma A_w}{NV} \quad (3.12)$$

where,  $b$  = X-ray density (gm/cc),  $\Sigma A_w$  = Sum of the atomic weights of all the atoms in the unit cell,  $N$  = Avogadro's number and  $V$  = volume of unit cell (cc). NiCuZn ferrite is a cubic crystal structure and it contains 8 formula units in one unit cell. The equation (3.12) becomes:

$$b = \frac{8M_w}{Na^3} \quad (3.13)$$

where,  $M_w$  is the molecular weight and 'a' is the lattice parameter of unit cell. The percentage porosity is calculated as follows [119]:

$$\% \text{ Porosity} = \frac{\text{X - ray Density} - \text{Bulk Density}}{\text{X - ray Density}} \times 100 \quad (3.14)$$

### 3.4.2 Microstructural Analysis

Microstructure of the sintered ferrite specimens were analyzed by a Scanning Electron Microscope (SEM). In SEM, a hot tungsten filament electron gun under vacuum emits electrons which pass through a series of electromagnetic lenses. The sample is then bombarded with a fine beam of electrons having acceleration potentials range from 1-30 kV. A part of the beam is reflected as back scattered electrons (BSE) along with low energy secondary electron emission (SE), cathode luminescence, X-ray excitation beam and electron transmission also take place.

Images formed from the (SE) beam were studied in the extrinsic mode of SEM. While the images appeared very real as if they are photographed by ordinary means, the apparent illumination was a function of particle emission rather than radiation. The emitted secondary electrons are detected and displayed on a scanning TV display. A bright image will be the result of high secondary electron emission, while the primary influence on high emission is the surface structure of the specimen. The end result is therefore brightness associated with surface characteristics and an image which looks very much like a normally illuminated subject.

Sample surfaces were ground with the help of a series of diamond grinding pad from 1200  $\mu\text{m}$  to 15  $\mu\text{m}$  on an automatic polishing machine. The samples were polished with 8  $\mu\text{m}$  diamond paste on a rotating disk. Final polishing was done with 6, 2 and 1  $\mu\text{m}$  diamond pastes to create a mirror finish on a lapping machine. Prior to microscopic analysis, the samples were thermally etched at 50°C less than the respective sintering temperature. Thermal etched samples were heated up at the rate of 10°C/min whereas, the rate of cooling was 10°C/min initially up to 1000°C/min and subsequently at 5°C/min up to room temperature.

The thermally etched samples were mounted on a metal stub with carbon paint. The samples were thinly coated with palladium-gold under vacuum of 0.01 torr to make the surface conducting for viewing through SEM. The mounted specimens were studied by SEM (JEOL-JSM840). The grain size was determined using a rectangular intercept procedure, following the ASTM E112-88 standard.

### **3.4.3 Phase Analysis and Structural Refinement**

Phase analysis and crystallite size determination of the sintered specimen was done by XRD technique. The fundamentals and experimental method have been discussed in section 3.2.2.

A Rietveld structural refinement produces was used to analyze the diffraction patterns using MAUDWEB (version 2.031) software. MAUD is quite different from other Rietveld programs in the way it treats the peak broadening effect. Instead of using a unique classical Caglioti and similar formulas to describe the broadening change with  $2\theta$  as a sum of the instrumental and sample broadening, Maud treats separately the instrumental from the sample aberrations.

The Rietveld method [120] is a powerful technique to extract detailed structural information from powder diffraction data. In contrast to the conventional profile fitting, this method does not use integrated intensities of reflections but employs the entire powder diffraction pattern. In this method, each data point in the digitized intensity versus  $2\theta$  curve is an independent observation and during refinement, structure parameters, background parameters and profile parameters are



varied in a least squares procedure until the simulated pattern matches well with observed pattern for the proposed crystal structure model [121].

In Rietveld method the principal goal is to refine crystal structure not profiles. The things actually being refined are parameters in models for the crystal structure and for other specimen and instrument effects on the diffraction pattern. In this method the least squares refinements are carried out until the best fit is obtained between the entire observed powder diffraction pattern taken as a whole and the entire calculated pattern based on the simultaneously refined models for the crystal structures, diffraction optics effects, instrumental factors and other specimen characteristics i.e. lattice parameters as may be desired and can be modeled.

The quantity minimized in the least square refinement is the residual  $S_y$  [121]:

$$S_y = \frac{\sum W_i}{(I_i - I_{ci})^2} \quad (3.15)$$

where,  $I_i$  is observed intensity at the  $i^{\text{th}}$  Step, and  $I_{ci}$  is calculated intensity at the  $i^{\text{th}}$  Step and  $W_i = 1/I_i$ .

Initially, the positions of the peaks were corrected by successive refinements of zero-shift error. Considering the integrated intensity of the peaks as a function of structural parameters only, the Marquardt least-squares procedures were adopted to minimize the difference between the observed and simulated patterns.

Rietveld refinement process will adjust the refineable parameters until the residual [equation number (3.16)] is minimized with some sense. The users of the Rietveld method have developed several ‘ $R_a$ ’ values that are now commonly used [121] and expressed as follows:

$$R_p ( \text{‘}R_a\text{’ pattern) = } \frac{\sum I_i(\text{obs}) - I_i(\text{calc})}{\sum I_i(\text{obs})} \quad (3.16)$$

$$R_{wp} ( \text{‘}R_a\text{’ weighted pattern) = } \left\{ \frac{\sum W_i ([I_i(\text{obs}) - I_i(\text{calc})])^2}{\sum W_i (I_i(\text{obs}))^2} \right\}^{1/2} \quad (3.17)$$

$R_{wp}$  is the most meaningful of these  $R_a$ 's because the numerator is the residual being minimized. Another useful numerical criterion is the “goodness of fit”,  $G$ .

$$G = \left( \frac{S_y}{F - E} \right)^{1/2} \quad (3.18)$$

where,  $F$  is the number of observations (e.g. the number of  $I_i$ 's used) and  $E$  is the number of parameters adjusted. A ‘ $G$ ’ value of 1.3 or less is usually considered to be quite satisfactory. The Rietveld structure refinement was carried out on  $(Ni_{0.25}Cu_{0.2}Zn_{0.55})La_xFe_{2-x}O_4$  ferrites with  $x = 0.0, 0.025, 0.05$  and  $0.075$  nominal compositions.

#### 3.4.4 Magnetization

Saturation Magnetization has been determined from the force experienced by the ferrite specimen in a field gradient. It was measured using vibrating sample magnetometer (VSM) (model-7410, Lake Shore). The principle of VSM is the measurement of the electromotive force induced by magnetic sample when it is vibrated at a constant frequency in the presence of a static and uniform magnetic field. A small part of the pellet (10-40 mg) was weighed and made to avoid movements inside the sample holder. The VSM was operated to 3 T at a vibration frequency of 82 Hz. It was calibrated using a Ni standard (sphere) with known magnetization ( $M_s = 6.92$  emu at 5 kOe).

#### 3.4.5 Inductance and Magnetic Loss

Inductance and magnetic loss are the basic magnetic property of any ferrites. The Impedance Analyzer; Model 4192A, Hewlett Packard, USA, with the maximum frequency limit of the instrument 13 MHz, was used to measure the inductance and  $\tan\delta$  on toroid samples, wound with low capacitive six turns (Fig. 3.5) enameled copper wire. The significance of this winding is that the stray capacitance (undesirable capacitance which can allow signals to leak between circuit wires) can be reduced by this special winding of the ferrite core [43].

The inductance of a ferrite core depends on the number of turns, diameter of the coils, the length of the coil, and the nature of the ferrite composition. By definition, inductance is the ratio of the total magnetic flux linkage to the current

(I) through the ferrite core. Total magnetic flux linkage is dependent on magnetic permeability ( $\mu$ ) of the medium (core material). This means inductance is directly proportional to permeability.



**Fig. 3.5.** Low capacitance winding of six turns on ferrite core.

Initial permeability was calculated from the inductance data as per [35] using the following formula:

$$\mu_i = \frac{L}{2 * 10^{-7} * N_a^2 * H_t * \ln [D_o / D_{in}]} \quad (3.19)$$

where  $L$  is the inductance,  $N_a$  is the number of turn,  $H_t$ ,  $D_o$  and  $D_{in}$  are the toroid's height, outer diameter and inner diameter, respectively. The inductance was measured at the test conditions of frequency set at 100 kHz and voltage of 0.005 Volts. The permeability was further corrected for porosity using following equation [122]:

$$\mu_{actual} = \frac{\mu_i}{1 - V_{pi}} \quad (3.20)$$

where,  $V_{pi}$  is the volume fraction occupied by pores.

Variation in inductance with frequency was measured and permeability vs. frequency was plotted. Variation of inductance with temperature was also studied using the Curie set up. The ferrite core was uniformly heated at a constant heating rate and the inductance value corresponding to the temperature was measured by the impedance analyzer.

Core losses in ferrites are generally divided into hysteresis losses, eddy current losses and residual losses. High-frequency operating conditions, the hysteresis loss is mainly caused by the irreversible rotation of magnetization vector [123]. The eddy current loss is due to the current induced in the core under the influence of a time varying magnetic flux. The residual loss is generated by the power dissipation resulting from the reversible domain wall damping [124] and the reversible rotation of domains [125]. The relative loss factor (RLF), i.e. the ratio of the loss tangent ( $\tan\delta$ ) to initial permeability was calculated from  $\tan\delta$  and corrected initial permeability. Variation in RLF with frequency was measured in that frequency range.

### 3.4.6 Resistivity

Sintered ferrite pellet specimens were used to determine resistivity. Electrodes were painted (Fig. 3.6) on the surface of the sample using a conducting silver paste followed by curing at 300°C for 30 minutes. The AC resistivity  $\rho$  was calculated using the formula [126]:

$$\rho = \frac{1}{\omega \cdot \epsilon_0 \cdot k' \cdot \tan \delta} = \frac{A}{2\pi f \cdot \tan \delta \cdot C \cdot t} \quad (3.21)$$

where,  $\epsilon_0$  is the permittivity of free space,  $k'$  is the relative dielectric constant;  $\tan \delta$  is the dissipation or loss factor,  $\omega$  is the angular frequency,  $C$  is the capacitance,  $A$  and  $t$  are the area and thickness of the sintered pellet respectively.

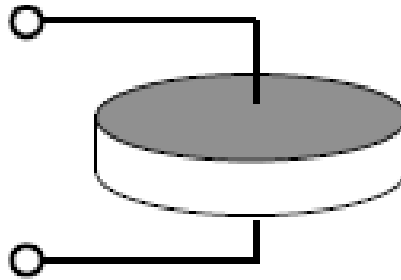


**Fig. 3.6.** Schematic electrode arrangement on the sintered pellet sample.

The Impedance Analyzer (Model 4192A, Hewlett Packard, USA) was used to measure the capacitance and  $\tan\delta$  on pellet sample at 100 kHz. Variation in

capacitance and  $\tan\delta$  with frequency was also measured and resistivity vs. frequency was plotted. All electrical and magnetic experiments are within the experimental error.

# *Chapter IV*

## *Results and Discussion*

## **4.1 Optimization of Zn concentration in $\text{Ni}_{0.8-x}\text{Cu}_{0.2}\text{Zn}_x\text{Fe}_2\text{O}_4$ ferrite ( $0.45 \leq x \leq 0.6$ )**

### **4.1.1 Introduction**

$(\text{Ni}_{0.8-x}\text{Cu}_{0.2}\text{Zn}_x)\text{Fe}_2\text{O}_4$  ferrites with  $x = 0.45, 0.50, 0.55$  and  $0.60$  were investigated to optimize Zn concentration. The Zn concentration in this range  $x = 0.45$ – $0.60$  were used as the saturation magnetization were reported to be maximized at higher concentration of Zn for other ferrites [43]. The Cu content of the compositions was kept constant at 10 mol% of B site as the dc resistivity was reported to be maximized in  $(\text{Ni}_{0.3}\text{Zn}_{0.5}\text{Cu}_{0.2})(\text{Fe}_2\text{O}_4)_{0.98}$  ferrite [5].

Different ranges of electromagnetic properties have been reported with various Zn concentrations in NiCuZn ferrites [22, 44]. Optimization of Zn concentration with respect to Ni will be investigated to achieve high permeability as well as high resistivity in the ferrites.

Ferrite compositions were synthesized through sol-gel auto combustion process. Details methodology has been illustrated in experimental chapter (section 3.1.2, 3.3). Briefly to prepare 20 gm  $(\text{Ni}_{0.8-x}\text{Cu}_{0.2}\text{Zn}_x)\text{Fe}_2\text{O}_4$  ferrite with  $x = 0.45, 0.50, 0.55$  and  $0.60$  composition, 0.0294, 0.0251, 0.0208 and 0.0167 mol nickel nitrate; 0.01678, 0.01674, 0.01673 and 0.01670 mol copper nitrate; 0.0377, 0.0418, 0.0460 and 0.0501 mol zinc nitrate; 0.1678, 0.1675, 0.1672 and 0.1670 mol ferric nitrate; 0.2516, 0.2512, 0.2506 and 0.2505 mol citric acid were taken respectively. The thermal decomposition behavior, phase formation, densification, sinterability, microstructural behavior and electromagnetic properties of ferrites were investigated.

### **4.1.2 Results and Discussion**

#### **4.1.2.1 Thermal Decomposition**

The thermal decomposition behavior of gel was studied by differential thermal analysis (DTA) and thermo-gravimetric (TG) analysis. Fig. 4.1 shows the DTA and TG of the gel precursor. There was one endothermic peak at about  $140^\circ\text{C}$  and one

exothermic peak at about 186°C in DTA. The thermo gravimetric analysis exhibited a two-step weight loss; one in the range 90-140°C, while the other at about 186°C.

The endothermic peak at about 140°C was due to the removal of residual water from gel. Dried gel sometime contained residual water and that has been reported by many researchers [127-128]. This dehydration process produced 3.2% weight losses in TG graph. The exothermic peak at around 186°C was caused by the autocatalytic combustion reaction of nitrates with citric acid. The combustion process, an exothermic one, can be considered as a thermally induced anionic redox reaction of the gel in which the carboxyl groups act as reductant and  $\text{NO}_3^-$  ions act as oxidant [33, 129].

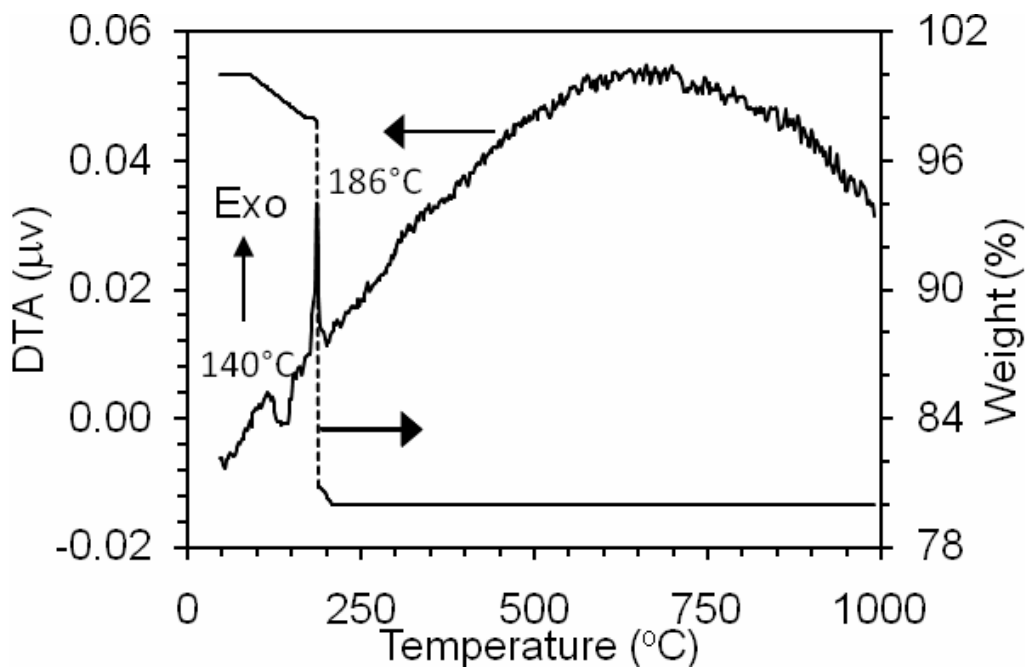
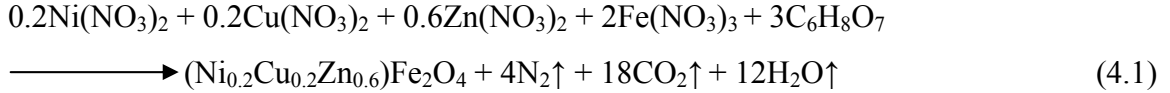


**Fig. 4.1.** DTA/TG plots for the nitrate-citrate gel with a heating rate of 10°C/min in air atmosphere.

In the combustion process heat is released which supply the energy needed to react the components to form NiCuZn ferrite through solid-state diffusion process [130]. During combustion  $\text{CO}_2$ ,  $\text{N}_2$ , and  $\text{H}_2\text{O}$  gasses are released. The nitrate-citrate combustion reaction for  $x=0.60$  composition may be stated as:





The decomposition at 186°C showed 16.8% weight losses in TG experiment. This weight loss is attributed to the loss of residual nitrate and organic matters [127], not the actual nitrate and organic matters as stated in equation (4.1). Similar weight loss was also reported by the authors and others [32]. The combustion behavior of the gel occurred suddenly in a single step. This single step decomposition behavior associated with a very sharp and intense exotherm, which was also reported by *A. Chakraborty et al.* [131].

#### 4.1.2.2 Phase Analysis

The phase formation behavior was studied by XRD. Fig. 4.2 shows the XRD patterns of the as-burnt ferrite powders. The powders were in crystalline state and identification revealed spinel ferrite phases similar to JCPDS card number 48-0489. There was no metal oxide phase in the as burnt powder.

The crystallite size was calculated from full width at half maximum of the [311] peak using Scherer formula. The crystallite size of as-burnt powders was in the range 19–22 nm. The as burnt powders were calcined at 700°C for 2 hrs to get more crystalline homogeneous spinel phase. The crystallite size of calcined powders was in the range 37-39 nm. Surface area of as burnt and calcined powder was 30-40 and 20-30 m<sup>2</sup>/gm respectively. This observation revealed that the nano-crystalline NiCuZn ferrite powders with high surface area could be synthesized directly by the auto-combustion of nitrate–citrate gels.

The sintered specimens were also characterized by XRD. The XRD pattern of sintered (Ni<sub>0.2</sub>Cu<sub>0.2</sub>Zn<sub>0.6</sub>)Fe<sub>2</sub>O<sub>4</sub> ferrite is compared with its as-burnt and calcined powders in Fig. 4.3. It was found that the broadening of diffraction peak decreased from as-burnt-to-calcined-to-sintered product, respectively. The crystallite size increased with successive heat treatment of the ferrite.

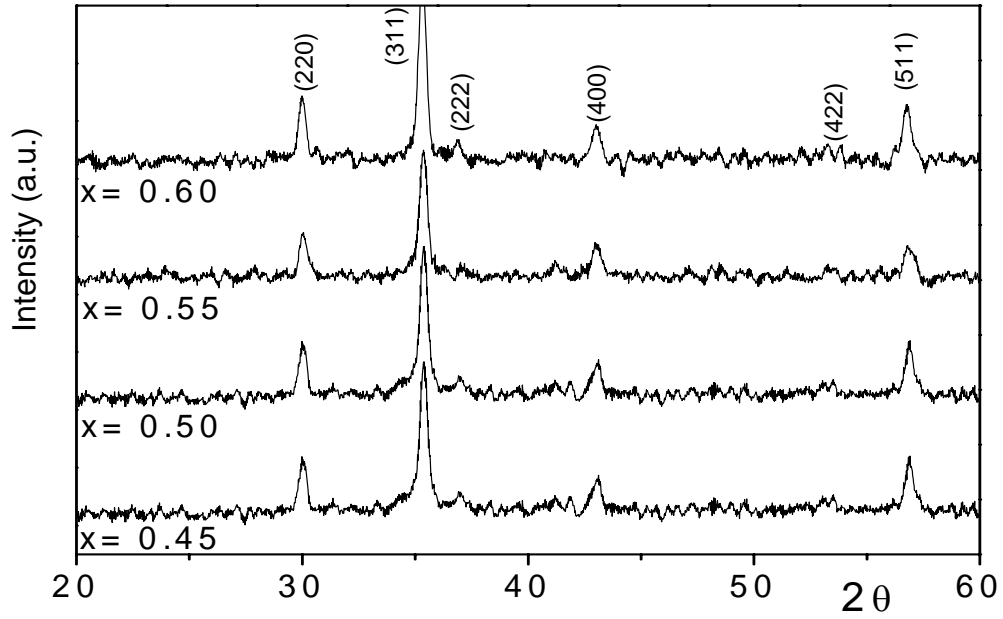


Fig. 4.2. XRD patterns of as-burnt powder of  $(\text{Ni}_{0.8-x}\text{Cu}_{0.2}\text{Zn}_x)\text{Fe}_2\text{O}_4$  ferrite with different Zn content.

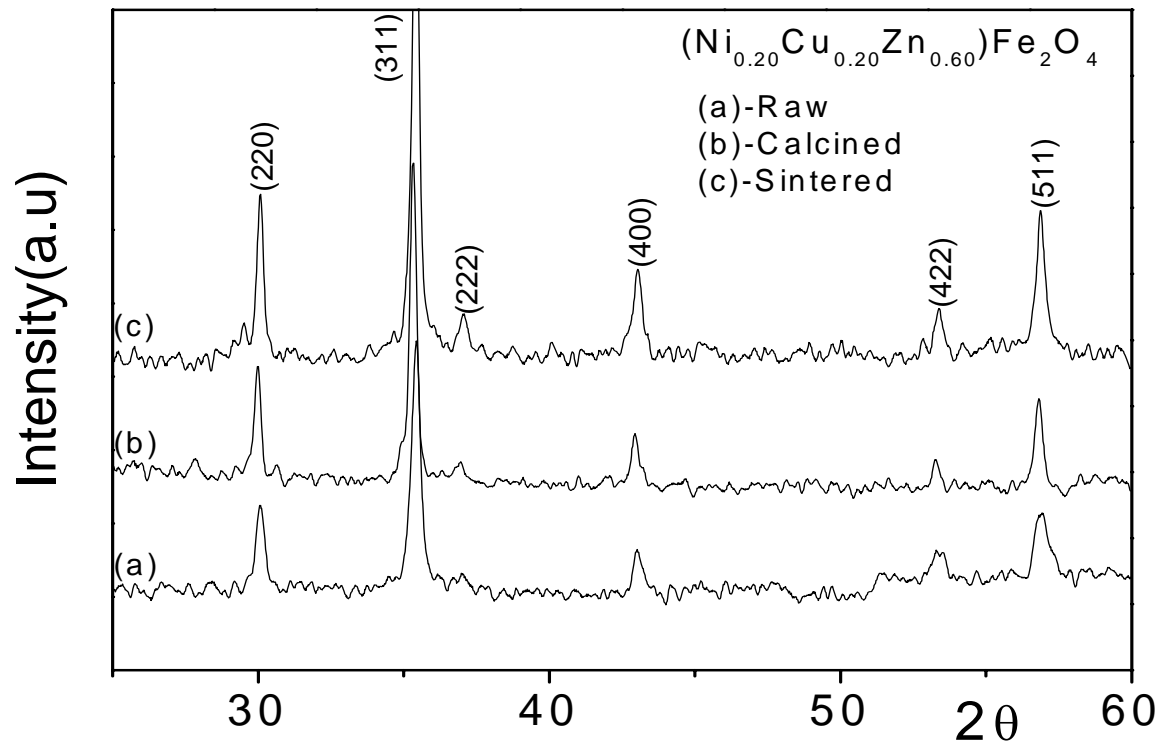
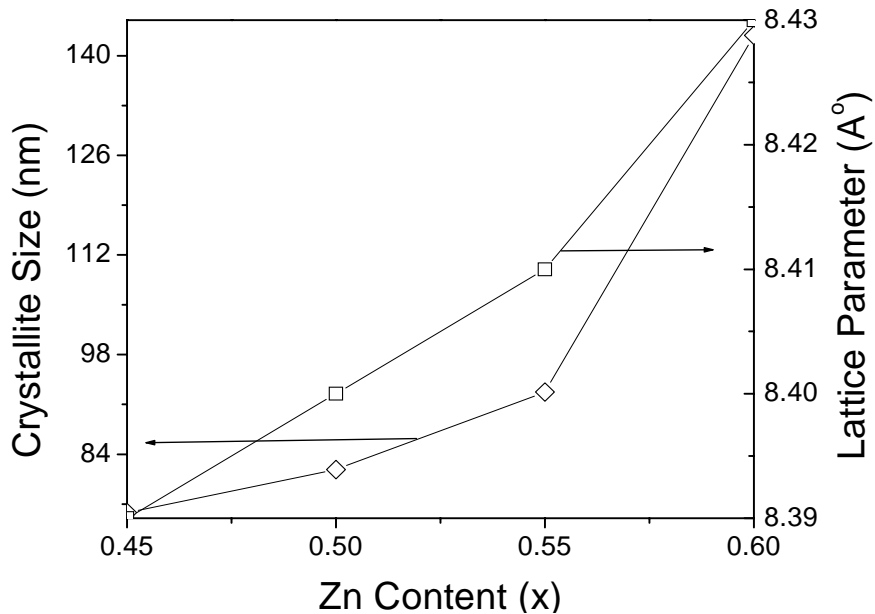


Fig. 4.3. XRD patterns of (a) as-burnt, (b) calcined and (c) sintered  $(\text{Ni}_{0.2}\text{Cu}_{0.2}\text{Zn}_{0.6})\text{Fe}_2\text{O}_4$  ferrite.

Table 4.1 shows the crystallite size and lattice parameters of sintered ferrites along with their bulk densities, apparent porosities and grain size. The crystallite size of sintered ferrites was in the range 75–143 nm. Fig. 4.4 shows the crystallite size and lattice parameters of  $(\text{Ni}_{0.8-x}\text{Cu}_{0.2}\text{Zn}_x)\text{Fe}_2\text{O}_4$  ferrites with different Zn content. The crystallite size of sintered product increased with Zn content. Lattice parameter was found to increase with increasing Zn substitution for Ni. This is attributed to the larger ionic radius of  $\text{Zn}^{2+}$  ( $0.84\text{\AA}$ ) as compared to the  $\text{Ni}^{2+}$  ( $0.74\text{\AA}$ ).

**Table 4.1** Crystallite size, lattice parameter, bulk density, apparent porosity and grain size of sintered  $(\text{Ni}_{0.80-x}\text{Cu}_{0.2}\text{Zn}_x)\text{Fe}_2\text{O}_4$  with different Zn content.

Zn-Content (x)	Crystallite Size (nm)	Lattice Parameter ( $\text{\AA}$ )	Bulk Density (gm/cc)	Apparent Porosity (%)	Grain Size ( $\mu\text{m}$ )
0.45	76	8.39	4.35 (0.01)	13.4	0.34
0.50	82	8.40	4.46 (0.02)	12.5	0.38
0.55	93	8.41	4.75 (0.01)	11.5	0.41
0.60	143	8.43	4.93 (0.01)	10.8	0.50



**Fig. 4.4.** Crystallite size and lattice parameter of sintered  $(\text{Ni}_{0.8-x}\text{Cu}_{0.2}\text{Zn}_x)\text{Fe}_2\text{O}_4$  ferrite with different Zn content. .

### 4.1.2.3 Densification and Microstructure

Fig. 4.5 shows the bulk density and apparent porosity of  $(\text{Ni}_{0.8-x}\text{Cu}_{0.2}\text{Zn}_x)\text{Fe}_2\text{O}_4$  ferrites with different Zn content. The bulk density increased with increasing Zn content, indicating improved densification by the substitution of Zn for Ni in the ferrite. Sintered density increased from 4.35 (for  $x = 0.45$ ) to 4.93 (for  $x = 0.60$ )  $\text{gm}/\text{cm}^3$ . The same type of phenomena was observed in NiZn ferrite [132].

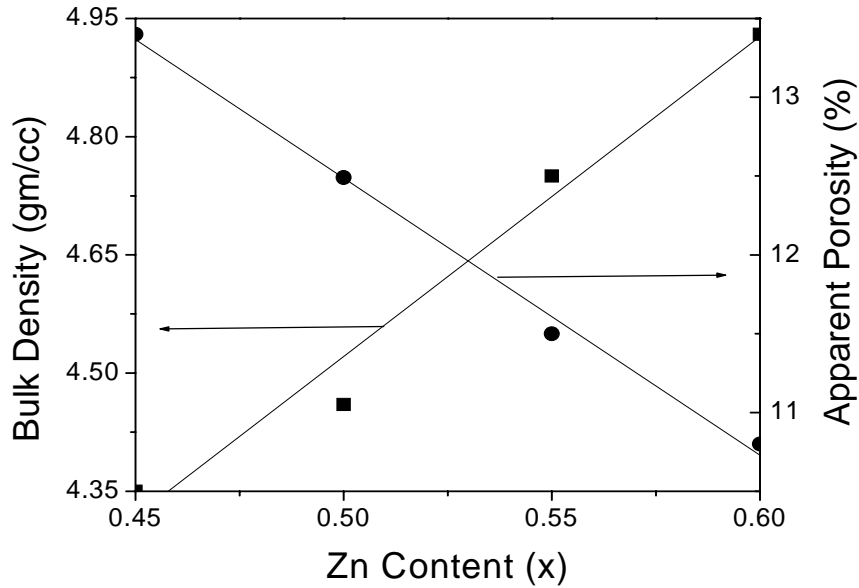


**Fig. 4.5.** Bulk density and apparent porosity of sintered  $(\text{Ni}_{0.8-x}\text{Cu}_{0.2}\text{Zn}_x)\text{Fe}_2\text{O}_4$  ferrite with different Zn content.

To see the effect of this Zn addition upon densification, sintering kinetics was also evaluated by thermo-mechanical analysis (TMA). Fig. 4.6 shows the shrinkage curves ( $5^\circ\text{C}/\text{min}$  heating rate in air) of different specimens. The slope of the shrinkage curve decreased with decreasing Zn content, which was very prominent for  $x = 0.45$  composition. This indicated that the rate of densification decreased with the decreasing Zn content. The dilatometric results also indicated that Zn acted as densification agent and reduced the sintering temperature. It is known that Ni reduces densification rate of NiCuZn ferrites; while Cu helps its densification [44]. This increase in densification might be due to the liquid phase formation in the ceramic or the expansion of unit cell (due to the higher ionic radius of Zn compared with the Ni) promoted material or atomic diffusion in the crystal lattice [133].

From the present study, it may be concluded that Zn substitution for Ni enhances densification rate (It may be noted that Cu content was fixed for all the compositions). The crystallite size of sintered ferrite was also found to increase with the increase in Zn substitution. This indicated that the Zn played an important role during sintering of the ferrites. It is evident from the Fig. 4.6 that the sintering temperature ( $\approx 900^\circ\text{C}$ ) of the ferrite powder, synthesized in this auto combustion process, was much lower than that of powders ( $\sim 1100^\circ\text{C}$ ) prepared by the conventional solid state reaction method [46].

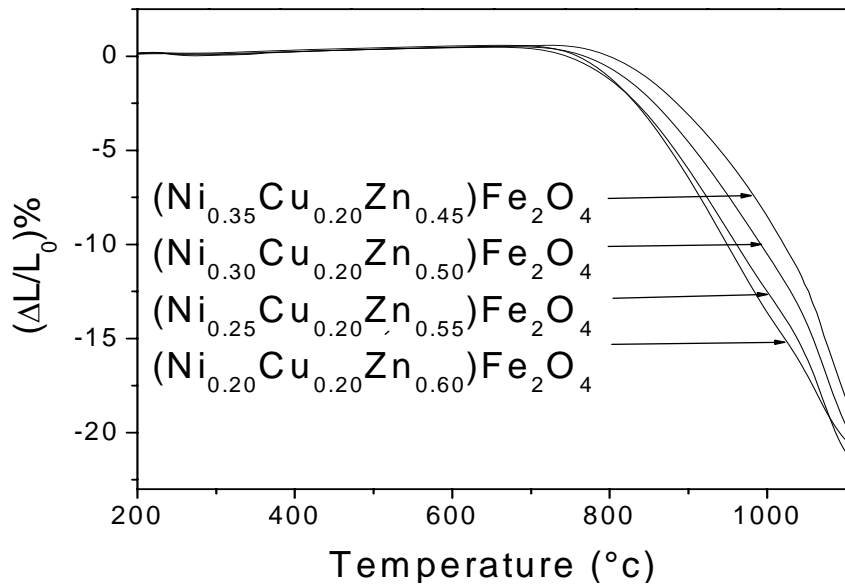


**Fig. 4.6.** Shrinkage curve at  $5^\circ\text{C}/\text{min}$  heating rate in air for  $(\text{Ni}_{0.8-x}\text{Cu}_{0.2}\text{Zn}_x)\text{Fe}_2\text{O}_4$  ferrite with different Zn content.

Fig. 4.7 shows the microstructure of sintered pellets. The grains grew as the Zn concentration increased. The average grain size increased from  $0.34$  ( $x = 0.45$ ) to  $0.50$  ( $x = 0.60$ )  $\mu\text{m}$ . This was due to the fact that sintering of ferrites might be assisted by a liquid phase that drew the particles together due to capillary forces and enabled more densification and grain growth.

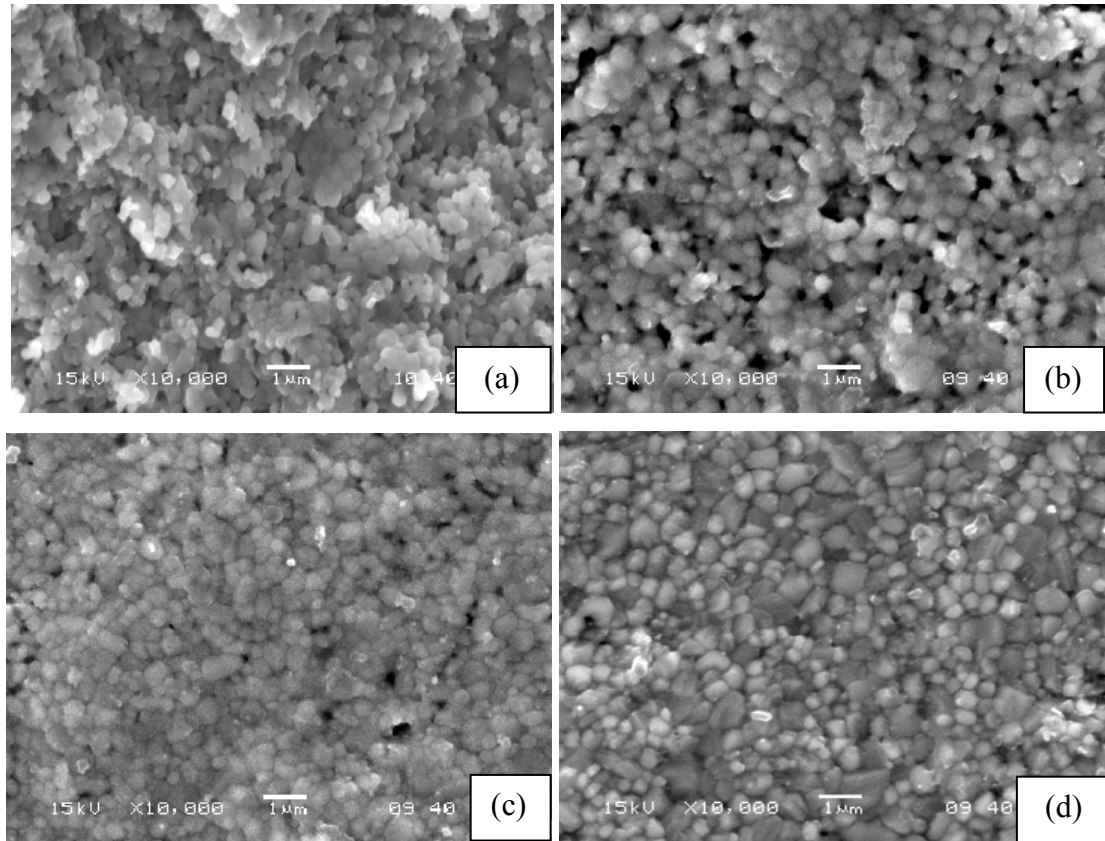


**Fig. 4.7.** SEM microstructures of sintered  $(\text{Ni}_{0.8-x}\text{Cu}_{0.2}\text{Zn}_x)\text{Fe}_2\text{O}_4$  ferrite with (a)  $x=0.45$ , (b)  $x=0.50$ , (c)  $x=0.55$  and (d)  $x=0.60$ .

#### 4.1.2.4 Electromagnetic Properties

Table 4.2 shows the permeabilities and saturation magnetization of sintered ferrites along with their resistivities. The permeability of the ferrite was found to increase with the increase in Zn content. The increase in permeability was primarily due to the substitution of Zn ion ( $d^{10}$ ) for Ni ( $d^8$ ) into the ferrite lattice.  $\text{Zn}^{2+}$  had a stronger preference for the tetrahedral site ('A' site), while  $\text{Ni}^{2+}$  ions (for which Zn is substituted) were located on octahedral site ('B' site) of  $\text{AB}_2\text{O}_4$  spinel ferrite. Thus, Zn displaced  $\text{Fe}^{3+}$  from 'A' to 'B' site. As the magnetic spin of neighboring 'A' and 'B'-sites were anti-ferromagnetically coupled; the net result was an increase in magnetic moment on the 'B' sub-lattice, as well as the net magnetic moment of the crystal increased.

The second reason was attributed to the increase in bulk density and average grain size of the ferrite with increased Zn substitution. It is known that ferrites

with higher bulk density and larger average grain size possess higher initial permeability, which is expressed by Globus model [134]:

$$\mu \approx \frac{3\mu_0 M_s^2 D}{16\gamma_w} \quad (4.2)$$

where,  $\mu_i$  is the initial permeability,  $\mu_0$  is the permeability of free space,  $M_s$  is the saturation magnetization,  $D$  is the average grain size and  $\gamma_w$  is the domain wall energy. The initial permeability is therefore, a linear function of grain size. An increase in the density (decrease in porosity) of ferrites not only resulted in the reduction of demagnetizing field due to decreased porosity but also raised the contribution due to rotation of spin, which in turn increased the permeability [53].

**Table 4.2** Permeability, saturation magnetization and resistivity of sintered  $(\text{Ni}_{0.80-x}\text{Cu}_{0.2}\text{Zn}_x)\text{Fe}_2\text{O}_4$  with different Zn content (measured at room temperature).

Zn-Content (x)	Permeability ( $\mu_i$ ) at 100 kHz	Saturation Magnetization (emu/gm)	Resistivity ( $*10^6 \Omega\text{-cm}$ ) at 100 kHz
0.45	70	61.28	11.32
0.50	76	63.56	10.39
0.55	111	65.13	8.9
0.60	168	68.13	3.3

Fig. 4.8 shows the magnetic hysteresis curve for  $(\text{Ni}_{0.8-x}\text{Cu}_{0.2}\text{Zn}_x)\text{Fe}_2\text{O}_4$  ferrites. The saturation magnetization was highest at the substitution  $x = 0.60$ . The magnetization increased with increasing Zn substitution, which was due to improved densification with Zn. It is known that magnetization increases with increasing density of the material which is expressed as follows [1]:

$$M = D_{\text{bulk}} * \sigma \quad (4.3)$$

where,  $M$  = magnetization,  $D_{\text{bulk}}$  = bulk density and  $\sigma$  = emu/gm. The increase in magnetization was also due to the increase in net magnetic moment of the crystal for substitution of Zn into the ferrite lattice.

Fig. 4.9 shows the frequency dependence of initial permeability in  $(\text{Ni}_{0.8-x}\text{Cu}_{0.2}\text{Zn}_x)\text{Fe}_2\text{O}_4$  ferrites with different Zn content. The permeability of compositions with  $x = 0.45, 0.50$  and  $0.55$  were stable up to 10 MHz and the cut-off frequencies of samples were above 13 MHz, the maximum frequency limit of the instrument.

The permeability of the  $x = 0.60$  composition was stable up to about 3 MHz whereas, the permeability dispersion initiated above 3 MHz. When ferrite specimens are subjected to an ac field, permeability shows several dispersions; as the field frequency increases, the various magnetization mechanisms become unable to follow the field. The dispersion frequency for each mechanism is different, since they have different time constant. The low frequency dispersions are associated with domain wall dynamics [134].

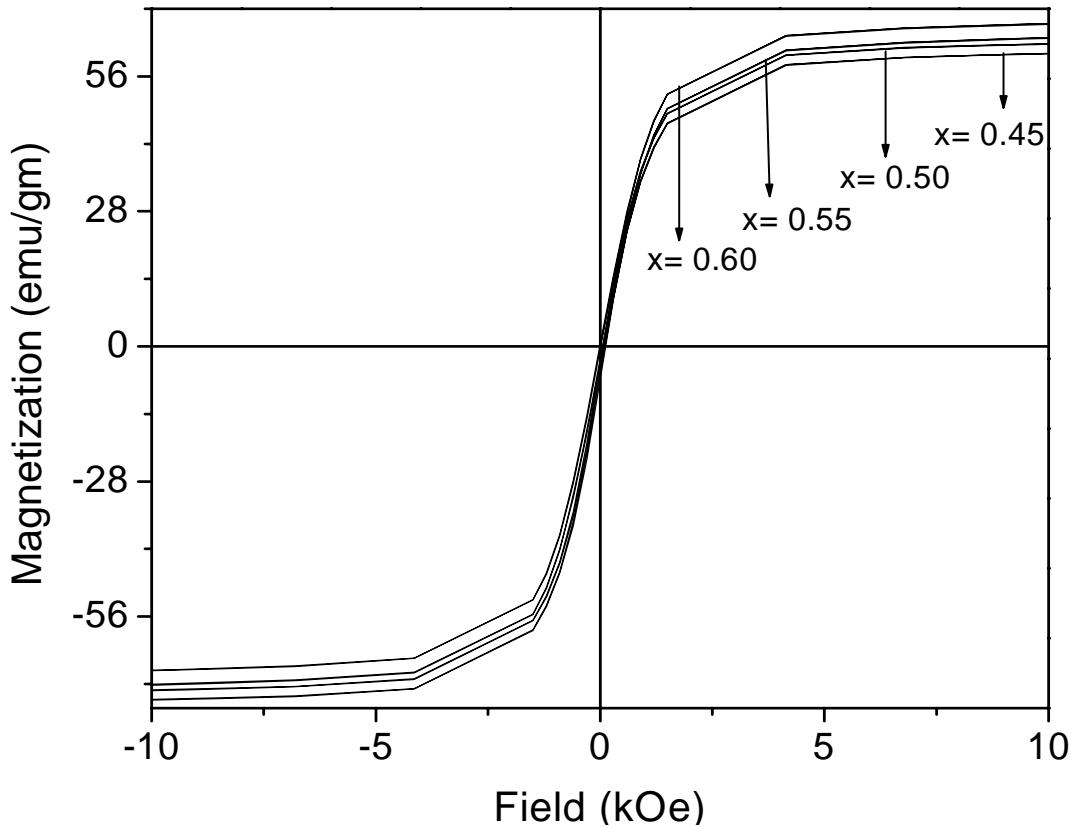


**Fig. 4.8.** Magnetic hysteresis curve for  $(\text{Ni}_{0.8-x}\text{Cu}_{0.2}\text{Zn}_x)\text{Fe}_2\text{O}_4$  ferrite with different Zn content measured by VSM at room temperature.



The dispersion was due to the much higher permeability of the composition ( $x = 0.60$ ) compared to others. The dispersion behavior could be explained by Snoek's law, which states that the cut-off frequency is inversely proportional to the magnetic permeability [135]. It is known that the permeability and the magnetic relaxation frequency are not independent, but are related by [134]:

$$\omega_i \mu_i^2 = \text{constant} \quad (4.4)$$

where,  $\omega_i$  is the magnetic relaxation frequency,  $\mu_i$  is the initial permeability.

So, lowest cut-off frequency for  $x = 0.60$  composition was due to its highest permeability among all.

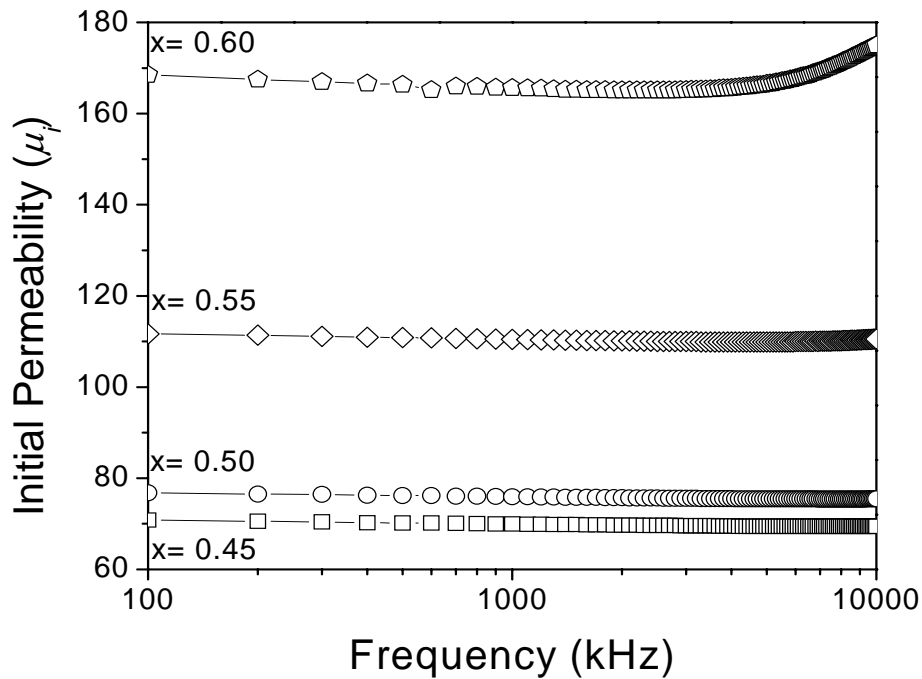


**Fig. 4.9.** Frequency dependency of initial permeability in  $(\text{Ni}_{0.8-x}\text{Cu}_{0.2}\text{Zn}_x)\text{Fe}_2\text{O}_4$  ferrite with different Zn content.

Fig. 4.10 shows the relative loss factor (RLF), i.e. the ratio of the magnetic loss tangent ( $\tan\delta$ ) to initial permeability ( $\mu_i$ ). High  $\mu_i$  and low  $\tan\delta$ , i.e. low RLF is required for high frequency magnetic applications. The RLF decreased with Zn substitution. That was due to the better densification of the ferrite with the Zn addition.

The higher RLF at  $x = 0.45$  might be due to higher hysteresis loss of the specimen, which might arise from its porous (Table 4.1) structure. It is known that hysteresis losses increase with the increase in porosity [136-137].

All ferrites had higher RLF at lower frequency (kHz) range. The RLF decreased with increasing frequency which could be explained by the following relation [43]:

$$\tan \delta = \frac{4\pi\varphi_{ac}}{\omega\varepsilon'} \quad (4.5)$$

where,  $\varepsilon'$  is the dielectric constant and  $\varphi_{ac}$  is the AC electrical conductivity,  $\omega (= 2\pi f)$  is the angular frequency.

The loss was primarily dependent on the frequency that was inversely proportional. This was why loss decreased with the increase in frequency. The increase in RLF above 3-4 MHz for composition  $x = 0.60$  was due to the relaxation losses of the specimen. The magnetic relaxation is presumed to be the reason for delay in the domain wall motion with respect to change in the externally applied magnetic field.

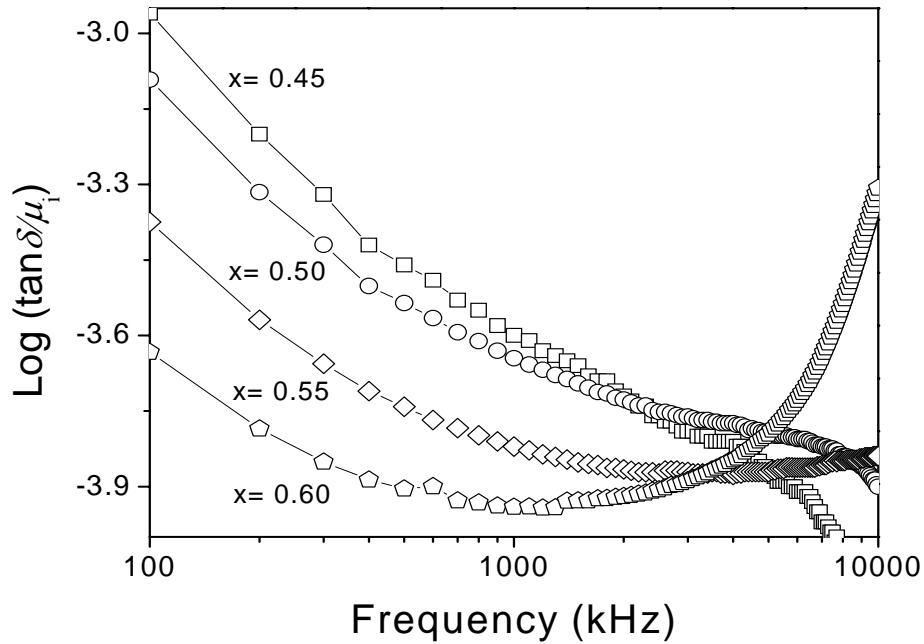


**Fig. 4.10.** Relative loss factor as a function of frequency in  $(\text{Ni}_{10.8-x}\text{Cu}_{0.2}\text{Zn}_x)\text{Fe}_2\text{O}_4$  ferrite with different Zn content.

Fig. 4.11 shows the frequency dependence of AC resistivity and the corresponding values are shown in Table 4.2. A small decrease in resistivity was found with increasing Zn content. The decrease in resistivity with Zn substitution was due to the increase in grain size of the ferrites. The grain size was found to increase with the Zn substitution (Table 4.1). The smaller grains resulted in large no of grain boundaries in the ferrite material. Grain boundaries were highly dislocated areas with trapped imperfections, such as porosity, dislocations and any other second phases. That is why it can act as scattering centers for the flow of electrons that contributes to the high resistivity [43].

The resistivity of all the compositions decreased with the increasing frequency. The resistivity ( $\rho$ ) was calculated as per equation (3.21). The resistivity was primarily dependent on the frequency and was found to be inversely proportional. That was why resistivity decreased with the increase in frequency. The low frequency region corresponds to high resistivity due to grain boundaries whereas, high frequency ranges correspond to low resistivity due to the grains [138].

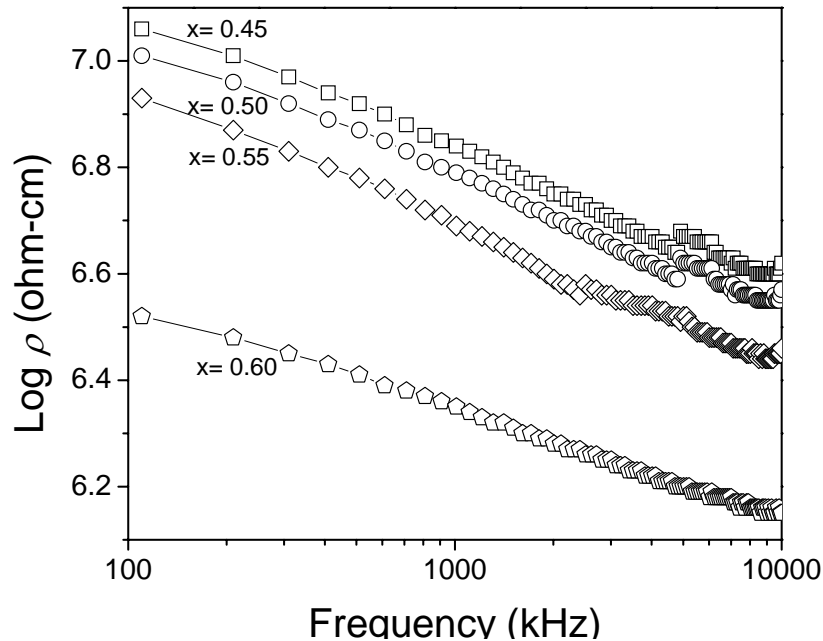


**Fig. 4.11.** AC resistivity as a function of frequency in  $(\text{Ni}_{0.8-x}\text{Cu}_{0.2}\text{Zn}_x)\text{Fe}_2\text{O}_4$  ferrite with different Zn content.

### 4.1.3 Summary

In this work Ni has been substituted by Zn to optimize Zn concentration in  $(\text{Ni}_{0.8-x}\text{Cu}_{0.2}\text{Zn}_x)\text{Fe}_2\text{O}_4$  ferrites. Nano crystalline NiCuZn ferrite powders were successfully synthesized by the ignition of gel precursor. Zn substitution helped in better densification of the ferrites. The sinterability of combustion synthesized powder ( $\approx 900^\circ\text{C}$ ) was much better than that of conventional solid-oxide route powder [24].

The compositions  $(\text{Ni}_{0.2}\text{Cu}_{0.2}\text{Zn}_{0.6})\text{Fe}_2\text{O}_4$  and  $(\text{Ni}_{0.35}\text{Cu}_{0.2}\text{Zn}_{0.45})\text{Fe}_2\text{O}_4$  showed highest permeability and resistivity, respectively. The nominal composition of  $(\text{Ni}_{0.25}\text{Cu}_{0.2}\text{Zn}_{0.55})\text{Fe}_2\text{O}_4$  was optimized for further study because it showed resistivity value  $\sim 3$  times higher than that of  $x = 0.60$  composition and permeability was stable up to 10 MHz frequency, although its permeability was about 1.5 times lower. In the following sections the effect of  $\text{Mg}^{2+}$ ,  $\text{La}^{3+}$  and  $\text{Sm}^{3+}$  substitutions and sintering aids will be investigated on the nominal composition of  $(\text{Ni}_{0.25}\text{Cu}_{0.2}\text{Zn}_{0.55})\text{Fe}_2\text{O}_4$ .

## 4.2 Effect of Mg substitution on structural and electromagnetic properties of $(\text{Ni}_{0.25}\text{Cu}_{0.2}\text{Zn}_{0.55})\text{Fe}_2\text{O}_4$ ferrite

### 4.2.1. Introduction

$(\text{Ni}_{0.25-x}\text{Mg}_x\text{Cu}_{0.2}\text{Zn}_{0.55})\text{Fe}_2\text{O}_4$  ferrites with  $x = 0.0, 0.07, 0.13, 0.18$  and  $0.25$  compositions were investigated to evaluate the effect of Mg on the ferrite. Mg containing composition is preferred to decrease the magnetostriction constant that helps to obtain high permeability [79].

Ferrite compositions were synthesized through sol-gel auto combustion process. Details experimental procedure has been illustrated in section 3.1.2, 3.3. Briefly to prepare 20 gm  $(\text{Ni}_{0.25-x}\text{Mg}_x\text{Cu}_{0.2}\text{Zn}_{0.55})\text{Fe}_2\text{O}_4$  with  $x = 0.0, 0.07, 0.13, 0.18$  and  $0.25$  composition, 0.0208, 0.0152, 0.0102, 0.0060 and 0 mol nickel nitrate; 0.0166, 0.0169, 0.0171, 0.0172 and 0.0174 mol copper nitrate; 0.0460, 0.0465, 0.0469, 0.0472 and 0.0477 mol zinc nitrate; 0.1672, 0.1690, 0.1705, 0.1718 and 0.1736 mol ferric nitrate; 0, 0.0059, 0.0111, 0.0155 and 0.0216 mol magnesium nitrate; 0.2506, 0.2536, 0.2558, 0.2576 and 0.2602 mol citric acid were taken respectively. The phase formation, densification, microstructural behavior and electromagnetic properties of ferrites were investigated.

### 4.2.2. Results and Discussion

#### 4.2.2.1 Phase Analysis

Phase formation was studied by XRD. Fig. 4.12 shows the XRD patterns of the as-burnt powders of different compositions. The powders were in crystalline state and identification revealed spinel ferrite phases similar to JCPDS card number 48-0489. There was no metal oxide phase in the as burnt powder.

The crystallite size was calculated from full width at half maximum of the [311] peak using Scherer formula. The crystallite size of as-burnt powders was in the range 17-20 nm. The as burnt powders were calcined at  $700^\circ\text{C}$  for 2 hrs to get more crystalline homogeneous spinel phase. The crystallite size of calcined powder was in the range 34-37 nm. Surface area of as burnt and calcined powder was 34-44 and 21-32  $\text{m}^2/\text{gm}$  respectively. This observation revealed that the nano-crystalline with high surface

area Mg substituted NiCuZn ferrite powders could be synthesized directly by the auto-combustion of nitrate–citrate gels. The sintered ferrites were also characterized by XRD. Fig. 4.13 shows the XRD patterns of different sintered ferrites.

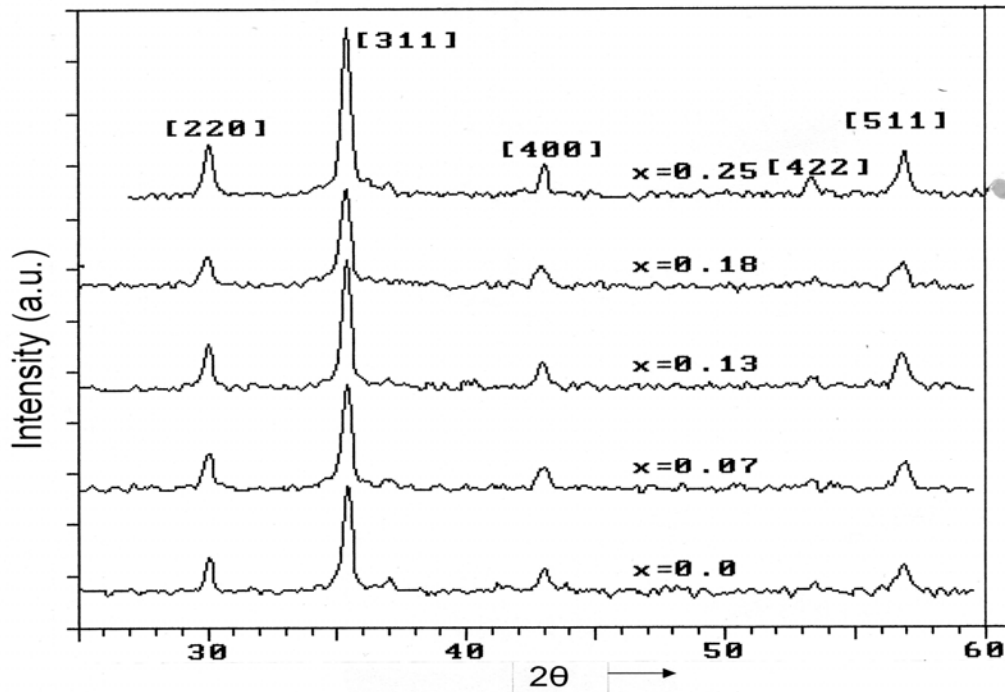


**Fig. 4.12.** XRD patterns of as-burnt  $(\text{Ni}_{0.25-x}\text{Mg}_x\text{Cu}_{0.2}\text{Zn}_{0.55})\text{Fe}_2\text{O}_4$  ferrites with different Mg content.

Table 4.3 shows the crystallite size and lattice parameter of sintered ferrites along with their bulk densities, apparent porosities, % closed porosities and grain sizes. The crystallite size of specimen was dependent on the Mg concentration up to  $x = 0.18$ . It is interesting to note that the crystallite size of sintered ferrite was enhanced when the composition contained both Mg and Ni.

The crystallite size of  $x = 0.0$  composition i.e. without Mg containing composition and  $x = 0.25$  composition i.e. without Ni containing compositions were much lower. The same trend was found in grain size of sintered specimen. This indicated that Mg could affect the crystallization and grain growth of the ferrite only if the

composition contained some Ni also. No noticeable change was found in lattice parameters as radius of  $Mg^{2+} \approx Ni^{2+}$ .

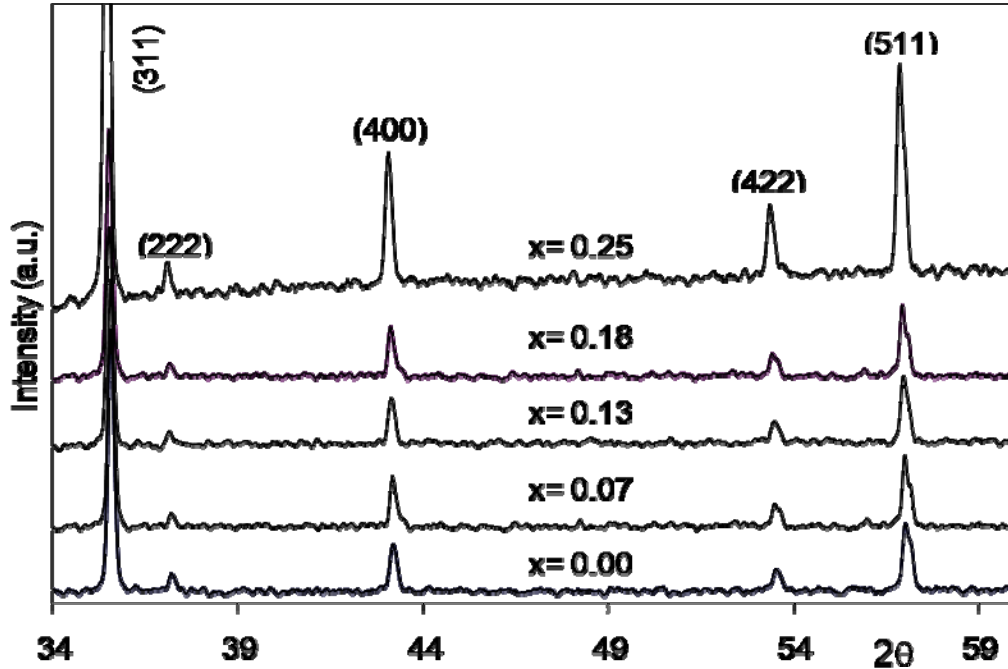


**Fig. 4.13.** XRD patterns of sintered  $(Ni_{0.25-x}Mg_xCu_{0.2}Zn_{0.55})Fe_2O_4$  ferrites with different Mg content.

**Table 4.3** Crystallite size, lattice parameter, bulk density, apparent porosity, percent closed porosity and grain size for sintered  $(Ni_{0.25-x}Mg_xCu_{0.2}Zn_{0.55})Fe_2O_4$  ferrites with different Mg content.

Mg-Content (x)	Crystallite Size (nm)	Lattice Parameter (Å)	Bulk Density (gm/cc)	Apparent Porosity (%)	Closed Porosity (%)	Grain Size (µm)
0	65	8.41	3.47 (0.02)	11.36	2.15	0.19
0.07	125	8.40	4.34 (0.02)	10.64	4.81	0.53
0.13	122	8.40	4.44 (0.01)	9.79	5.69	0.72
0.18	128	8.41	4.70 (0.01)	2.12	7.46	1.22
0.25	85	8.41	4.26 (0.02)	10.82	5.64	0.31

#### 4.2.2.2 Densification and Microstructure

Fig. 4.14 shows the bulk density and grain size of  $(\text{Ni}_{0.25-x}\text{Mg}_x\text{Cu}_{0.2}\text{Zn}_{0.55})\text{Fe}_2\text{O}_4$  ferrites with different Mg content. The bulk density increased with increasing Mg content, indicating improved densification by the substitution of Mg for Ni in NiCuZn ferrites. It might be considered that Mg addition lowered the eutectic temperature in NiCuZn ferrites [81]. However, density of MgCuZn ferrite ( $x = 0.25$ ) was lower than  $x = 0.18$  composition, might be due to the absence of Ni in the composition at  $x = 0.25$ .

Porosity decreased with increasing Mg content. Although, specimens contained some closed porosity. It was difficult to remove closed porosity completely due to the evaporation of constituents specially Zn. The amount of closed porosity increased with Mg content might be due to the formation of higher amount of liquid phase and hence higher rate of densification. Fig. 4.15 shows the microstructure of sintered specimens. The grains grew as the Mg concentration increased. The average grain size increased from 0.19 ( $x = 0.0$ ) to 1.22 ( $x = 0.18$ )  $\mu\text{m}$  and  $x = 0.18$  composition had bigger grain size.

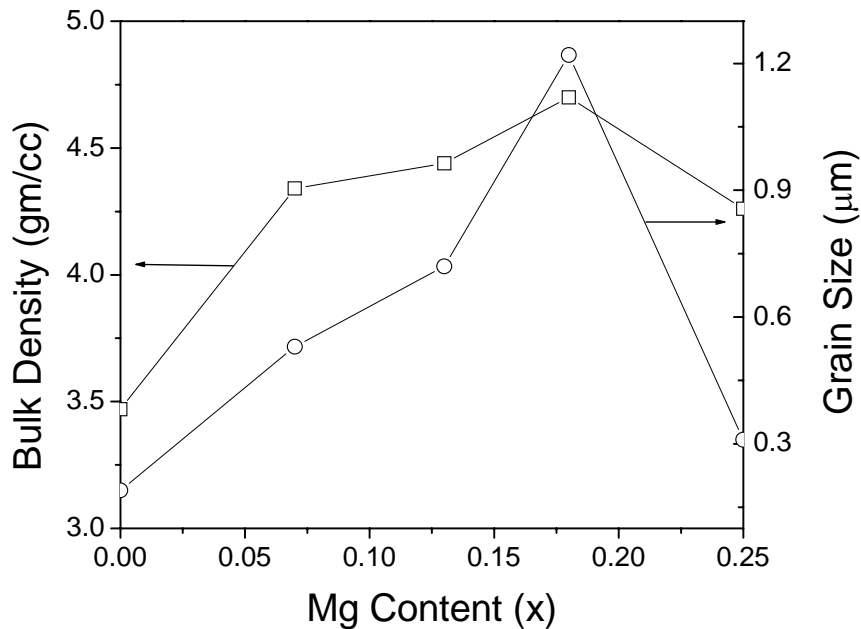


**Fig. 4.14.** Bulk density and grain size of sintered  $(\text{Ni}_{0.25-x}\text{Mg}_x\text{Cu}_{0.2}\text{Zn}_{0.55})\text{Fe}_2\text{O}_4$  ferrites with different Mg content.



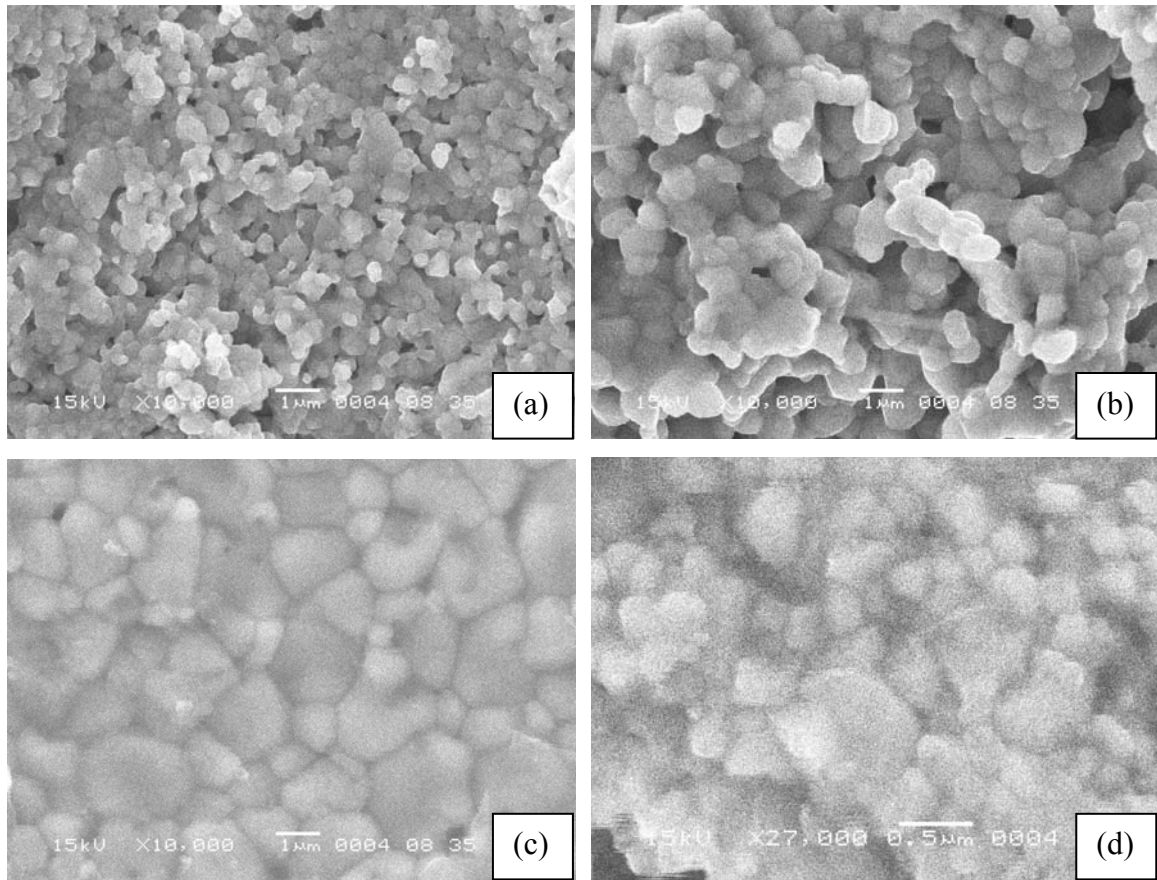


**Fig. 4.15.** SEM photographs of sintered  $(\text{Ni}_{0.25-x}\text{Mg}_x\text{Cu}_{0.2}\text{Zn}_{0.55})\text{Fe}_2\text{O}_4$  ferrites with (a)  $x=0.07$ , (b)  $x=0.13$ , (c)  $x=0.18$  and (d)  $x=0.25$ .

#### 4.2.2.3 Electromagnetic Properties

Fig. 4.16 shows the magnetic hysteresis curve for  $(\text{Ni}_{0.25-x}\text{Mg}_x\text{Cu}_{0.2}\text{Zn}_{0.55})\text{Fe}_2\text{O}_4$  ferrites. Table 4.4 shows the saturation magnetization and permeabilities of sintered ferrites along with their resistivities. The saturation magnetization of substituted compositions were higher than un-substituted sample, might be due to better density that could be explained by equation (4.3).

Fig. 4.17 shows the initial permeability as a function of Mg content. The permeability increased with increasing Mg content in NiCuZn ferrite. Increase in initial permeability with Mg content was primarily attributed to the increase in bulk density. It is known that ferrites with higher density and larger average grain size possess a higher initial permeability as per equation (4.2).

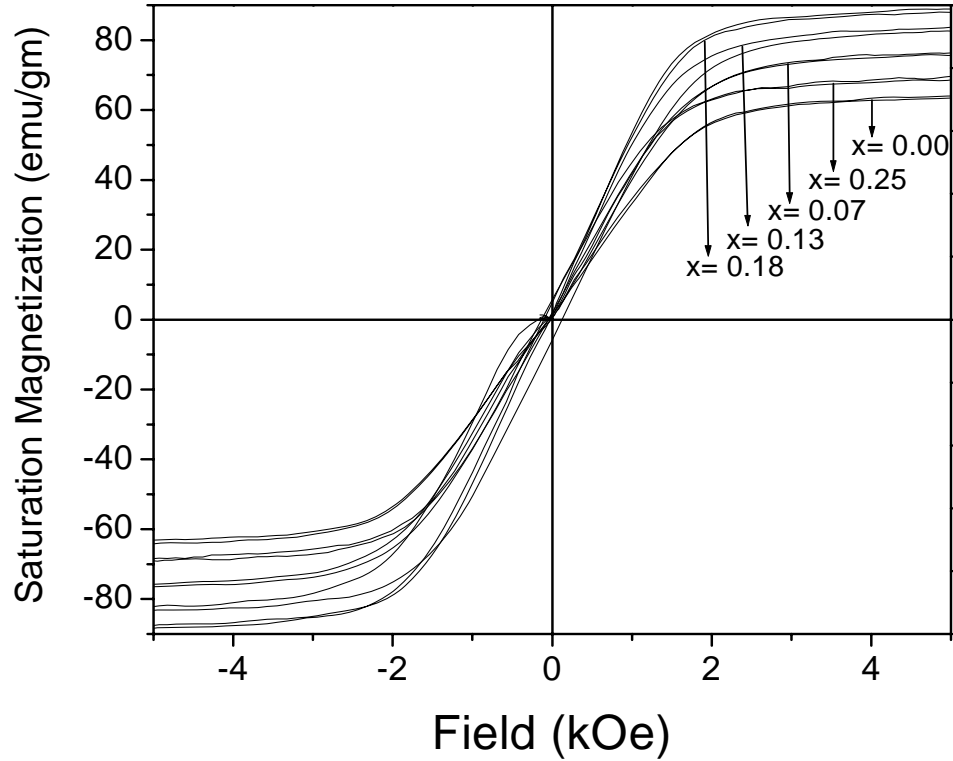


**Fig. 4.16.** Magnetic hysteresis curve for  $(\text{Ni}_{0.25-x}\text{Mg}_x\text{Cu}_{0.2}\text{Zn}_{0.55})\text{Fe}_2\text{O}_4$  ferrites with different Mg content measured by VSM at room temperature.

**Table 4.4** Saturation magnetization, permeability and resistivity for sintered  $(\text{Ni}_{0.25-x}\text{Mg}_x\text{Cu}_{0.2}\text{Zn}_{0.55})\text{Fe}_2\text{O}_4$  ferrites with different Mg content (measured at room temperature).

Mg-Content (x)	Saturation Magnetization (emu/gm)	Permeability ( $\mu_i$ ) at 100kHz	Resistivity ( $*10^6\text{ohm-cm}$ ) at 100kHz
0	65.07	268	1.2
0.07	76.09	680	5.4
0.13	78.45	940	6.3
0.18	85.46	2420	42
0.25	69.08	502	2.6

There was a sharp increase in permeability of nominal composition at  $x = 0.18$ . That sharp increase could not be fully explained by density and grain size parameters. The initial permeability of ferrite is usually expressed as follows [34];

$$\mu_i = \frac{M_s^2}{xK + y\eta\zeta} \quad (4.6)$$

where,  $\mu_i$  is the initial permeability,  $M_s$  is the saturation magnetization,  $K$  is the crystal magnetic anisotropy,  $\eta$  is the magnetostriction constant,  $\zeta$  the inner stress,  $x$  and  $y$  are constants.

Mg ferrite has smaller magnetostriction constant and anisotropy [139]. So, the major part of the increased permeability in  $x = 0.18$  composition was attributed to the decrease in magnetostriction constant mainly and might be in parts, decrease in the anisotropy and inner stresses in this narrow composition range. However, the initial permeability of the composition at  $x = 0.25$  was much lower than the composition at  $x = 0.18$ . This was attributed to the lower bulk density and lower grain size in the specimen.

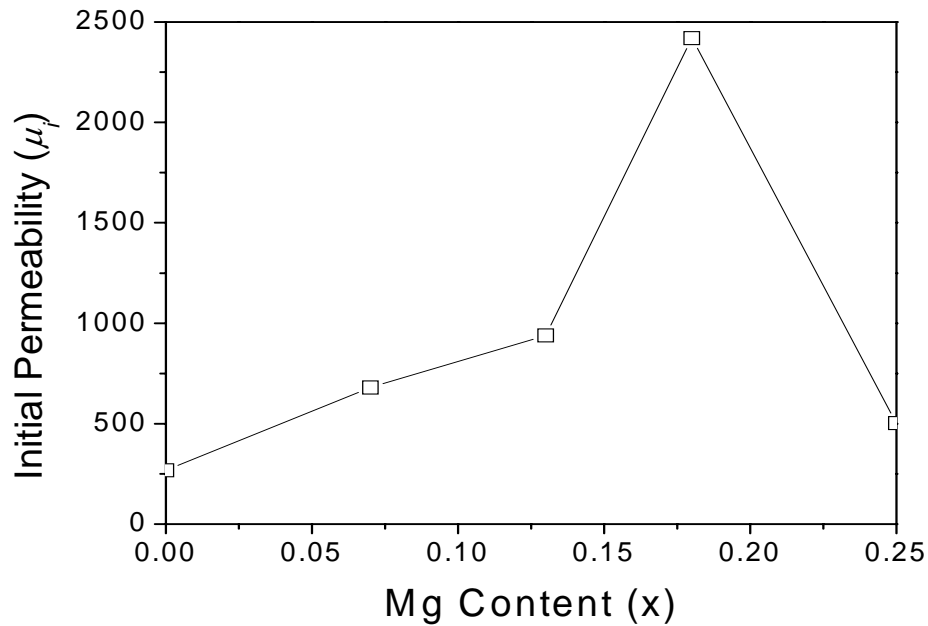


**Fig. 4.17.** Initial Permeability as a function of Mg content in  $(\text{Ni}_{0.25-x}\text{Mg}_x\text{Cu}_{0.2}\text{Zn}_{0.55})\text{Fe}_2\text{O}_4$  ferrites.

Fig. 4.18 shows the frequency dependence of permeability of  $(\text{Ni}_{0.25-x}\text{Mg}_x\text{Cu}_{0.2}\text{Zn}_{0.55})\text{Fe}_2\text{O}_4$  ferrites with different Mg content. It shows that the permeability

of compositions with  $x = 0.0, 0.07, 0.13$  and  $0.25$  were stable up to about  $10$  MHz and the cut-off frequencies of specimens were above  $13$  MHz, the maximum frequency limit of the instrument whereas, permeability of the  $x = 0.18$  composition was stable only up to about  $2$  MHz. The permeability dispersion occurred above about  $2$  MHz. That was due to the much higher permeability of the composition ( $x = 0.18$ ) compared to others, as explained by equation (4.4). The result of the experiment agrees with the Snock's law of cut-off frequency that is inversely proportional with magnetic permeability.

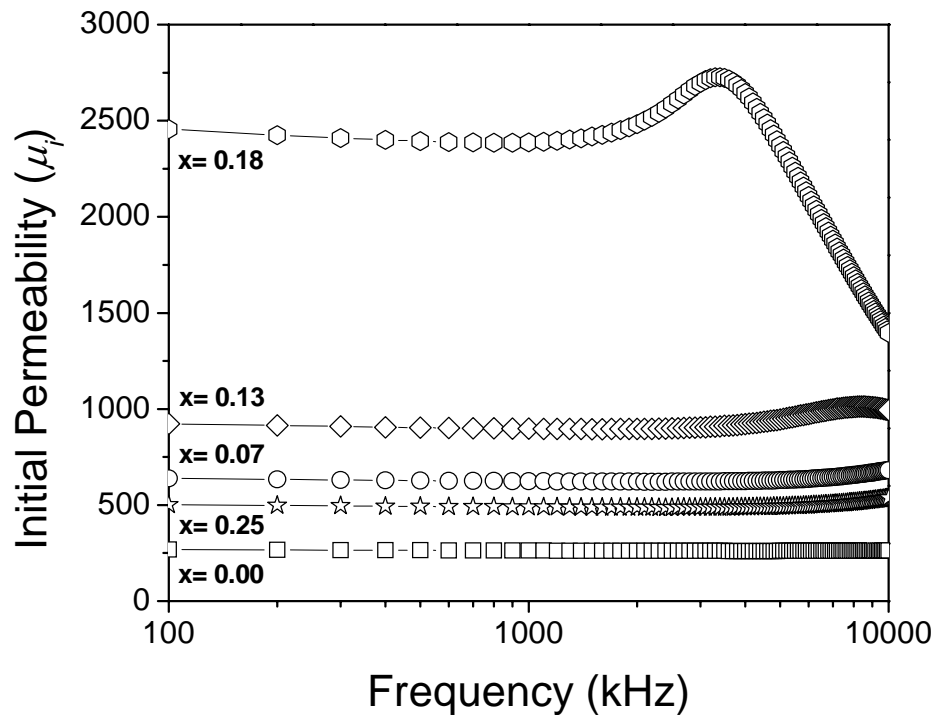


**Fig. 4.18.** Frequency dependence of initial permeability in  $(\text{Ni}_{0.25-x}\text{Mg}_x\text{Cu}_{0.2}\text{Zn}_{0.55})\text{Fe}_2\text{O}_4$  ferrites with different Mg content.

Fig. 4.19 shows the relative loss factor (RLF) i.e. the ratio of the magnetic loss tangent to the initial permeability. The figure shows that RLF decreases with Mg substitution. That was due to the better densification of the ferrite with the Mg substitution. The higher RLF at  $x = 0.0$  might be due to higher hysteresis loss of the specimen, which might arise from its porous (Table 4.3) structure. It is known that hysteresis losses increase with the increase in porosity [136-137]. The hysteresis loss is

mainly caused by the irreversible rotation of magnetization vector. The magnetization in the present ferrite may be primarily controlled by domain wall motions. Porosity, which acts as extra pinning centre, hinders the domain wall motion. In that case, higher field is required to switch the domain, which causes higher hysteresis losses

All ferrites had higher RLF at lower frequency (kHz) range. The RLF decreased with increasing frequency which could be explained by equation (4.5). RLF of all the cores increased in the MHz frequency zone due to the magnetic relaxation losses in the specimens.

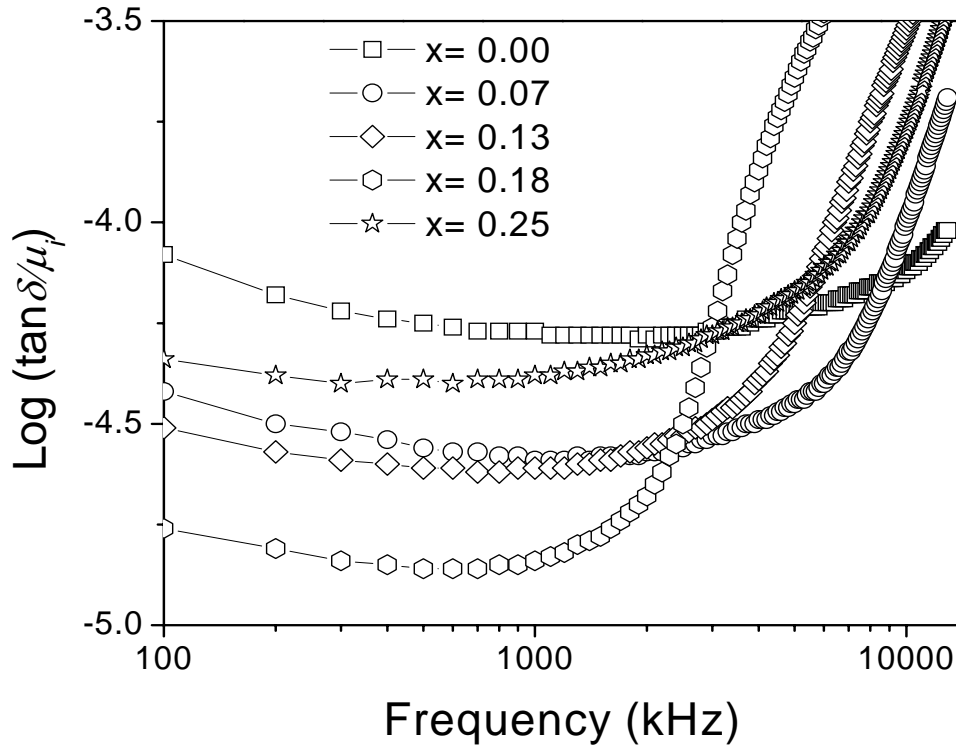


**Fig. 4.19.** Relative loss factor as a function of frequency in  $(\text{Ni}_{0.25-x}\text{Mg}_x\text{Cu}_{0.2}\text{Zn}_{0.55})\text{Fe}_2\text{O}_4$  ferrites with different Mg content.

Fig. 4.20 shows the frequency dependence of AC resistivity for different compositions. The increase in resistivity with Mg might be due to higher resistivity of Mg ferrite than that of NiZn ferrite [1]. The highest resistivity of composition at  $x = 0.18$  might be due to the presence of lower amount of  $\text{Fe}^{2+}$  ions in the ferrites. As the magnetic

anisotropy was expected to be lower at  $x = 0.18$  composition, the  $\text{Fe}^{2+}$  ions should be also lower. The magnetic anisotropy field in ferrites resulted mainly from  $\text{Fe}^{2+}$  ions [140].

The resistivity of all the compositions decreased with the increase in frequency. The resistivity was primarily dependent on the frequency that was inversely proportional as per equation (3.21). That was why resistivity decreased with the increase in frequency.

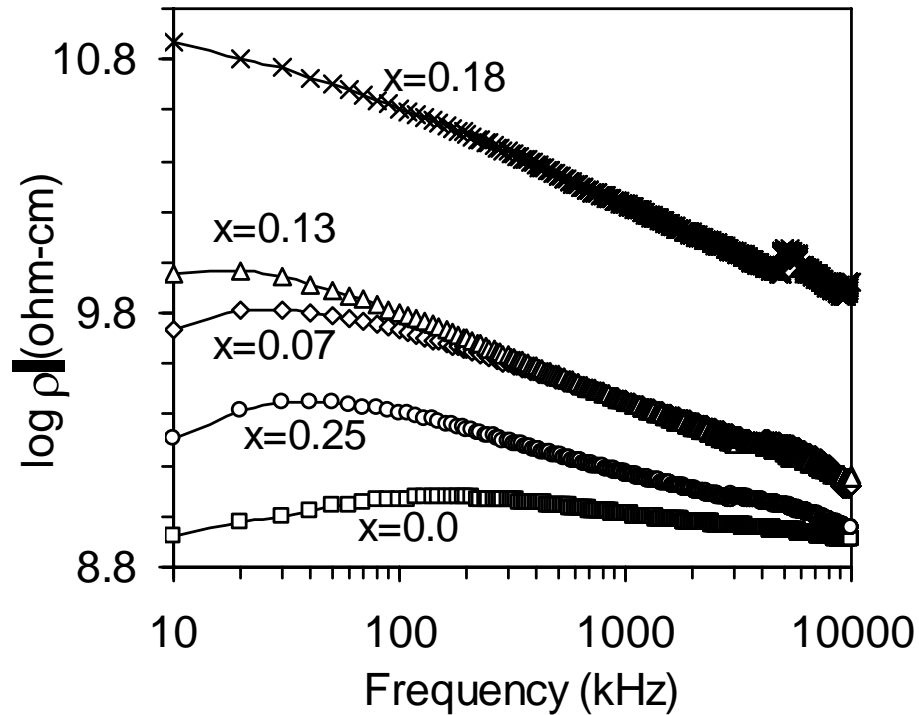


**Fig. 4.20.** AC Resistivity as a function of frequency in  $(\text{Ni}_{0.25-x}\text{Mg}_x\text{Cu}_{0.2}\text{Zn}_{0.55})\text{Fe}_2\text{O}_4$  ferrites with different Mg content.

### 4.2.3 Summary

$\text{Mg}^{2+}$  was substituted for  $\text{Ni}^{2+}$  in  $(\text{Ni}_{0.25-x}\text{Mg}_x\text{Cu}_{0.2}\text{Zn}_{0.55})\text{Fe}_2\text{O}_4$  ferrites. The bulk density and grain size increased with increasing Mg content.  $(\text{Ni}_{0.07}\text{Mg}_{0.18}\text{Cu}_{0.2}\text{Zn}_{0.55})\text{Fe}_2\text{O}_4$  nominal composition showed highest permeability, ac resistivity and lowest relative loss factor. The increase in permeability might be attributed to the decrease in magnetostriction constant and increase in densification with Mg substitution.

## **4.3 Effect of La substitution on structural and electromagnetic properties of $(\text{Ni}_{0.25}\text{Cu}_{0.2}\text{Zn}_{0.55})\text{Fe}_2\text{O}_4$ ferrite**

### **4.3.1 Introduction**

$\text{La}^{3+}$  was substituted for  $\text{Fe}^{3+}$  in  $(\text{Ni}_{0.25}\text{Cu}_{0.2}\text{Zn}_{0.55})\text{La}_x\text{Fe}_{2-x}\text{O}_4$  ferrite with  $x = 0.025, 0.05$  and  $0.075$ . La was substituted as it showed improved resistivity in NiZn ferrites [95]. Ferrite compositions were synthesized through sol-gel auto combustion process. Details methodology has been illustrated in experimental chapter (section 3.1.2, 3.3).

Briefly to prepare 20 gm  $(\text{Ni}_{0.25}\text{Cu}_{0.2}\text{Zn}_{0.55})\text{La}_x\text{Fe}_{2-x}\text{O}_4$  ferrite with  $x = 0.0, 0.025, 0.05$  and  $0.075$  compositions; 0.0208, 0.0207, 0.0206 and 0.0204 mol nickel nitrate; 0.01660, 0.01658, 0.01640 and 0.01630 mol copper nitrate; 0.0460, 0.0456, 0.0452 and 0.0448 mol zinc nitrate; 0.1672, 0.1638, 0.1604 and 0.1569 mol ferric nitrate; 0, 0.00207, 0.00412 and 0.00612 mol lanthanum nitrate; 0.2506, 0.2488, 0.2467 and 0.2446 mol citric acid were taken respectively. The effect of  $\text{La}^{3+}$  substitution on the density, microstructure, permeability, Curie temperature, magnetic losses, resistivity, saturation magnetization and hysteresis parameters of the ferrite were investigated. A Rietveld structure refinement was carried out to see the origin of the enhanced magnetic properties with La substitution.

### **4.3.2 Results and Discussion**

#### **4.3.2.1 Phase Analysis**

The La substituted NiCuZn ferrites were extensively characterized by XRD. Fig. 4.21 shows the XRD patterns of the as-burnt ferrite powders. The phase analysis revealed that the as burnt ferrite powders were crystalline (JCPDS card number 08-0234) in nature and contained spinel ferrite phase. The broad peaks in XRD patterns indicated fine crystallite size of the ferrite.

The crystallite size was calculated from full width at half maximum of the [311] peak using Scherer formula. The crystallite size of as-burnt powders was in the range 16-19 nm. The as-burnt powders were calcined at  $700^\circ\text{C}$  for 2 hrs to get more

crystalline homogeneous spinel phase. The crystallite size of calcined powders was in the range 30-35 nm. Surface area of as-burnt and calcined powder were 37-45 and 25-32 m<sup>2</sup>/gm respectively.

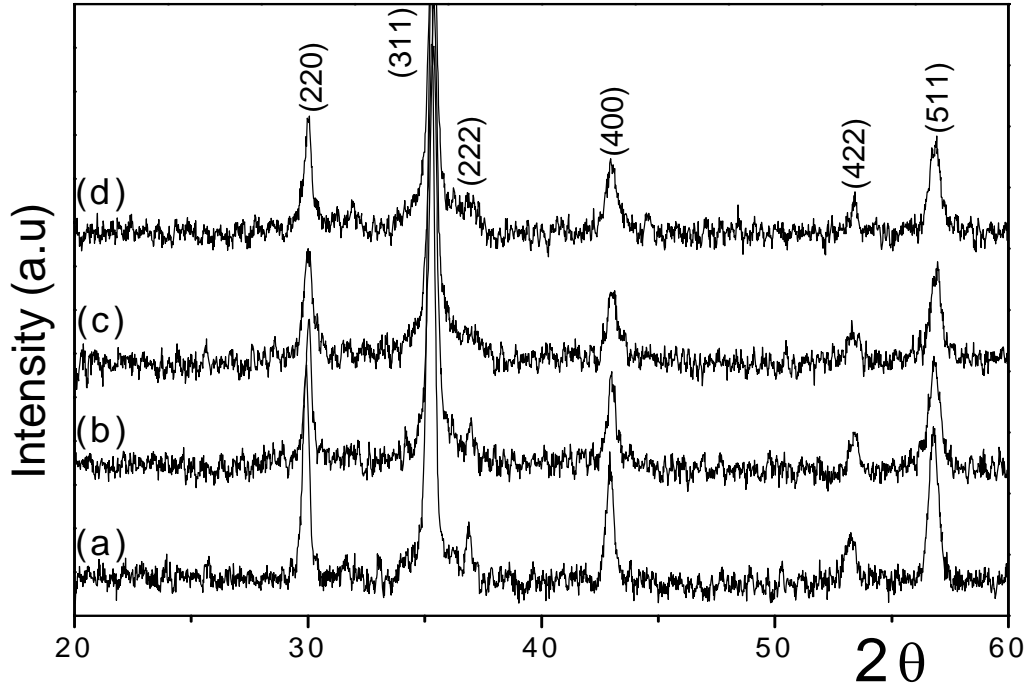


**Fig. 4.21.** XRD patterns of the as-burnt  $(\text{Ni}_{0.25}\text{Cu}_{0.2}\text{Zn}_{0.55})\text{La}_x\text{Fe}_{2-x}\text{O}_4$  ferrite with (a)  $x=0.0$ , (b)  $x=0.025$ , (c)  $x=0.05$  and (d)  $x=0.075$ .

To identify the possible formation of a second phase ( $\text{LaFeO}_3$ ) in substituted ferrite, the slow step scan XRD analysis was conducted on the samples after different stages of processing. Fig. 4.22 shows the step scan XRD pattern of as-burnt, calcined and sintered ferrite for  $x = 0.025$  (Fig. 4.22 (A)) and  $x = 0.075$  (Fig. 4.22 (B)) compositions, respectively.  $\text{LaFeO}_3$  was not detected in all raw powders and in calcined powder of  $x = 0.025$  composition. However, the phase was detected in calcined powder at  $x = 0.075$  nominal composition and in all sintered pellets.

The absence of  $\text{LaFeO}_3$  in as-burnt powders was due to the formation of amorphous/non-crystalline product of the same by very rapid rate of combustion reaction. Upon increased heat treatment (e.g. calcinations and sintering), the crystallinity of the phase increased both in calcined and sintered products. That  $\text{LaFeO}_3$  peaks were not



found in the calcined powder at  $x = 0.025$  nominal composition, might be due to the presence only a very little amount of crystalline  $\text{LaFeO}_3$  phase.

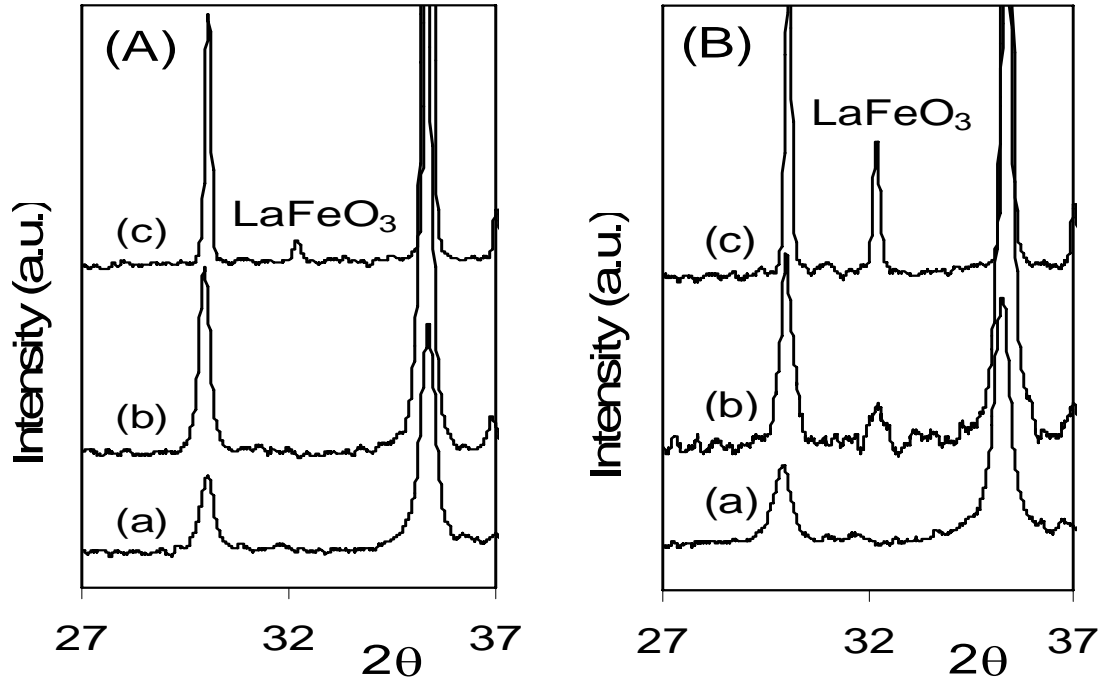


**Fig. 4.22.** XRD patterns of  $(\text{Ni}_{0.25}\text{Cu}_{0.2}\text{Zn}_{0.55})\text{La}_x\text{Fe}_{2-x}\text{O}_4$  ferrites with (A)  $x=0.025$ , (B)  $x=0.075$  and in each (a) as-burnt powder (b) calcined powder and (c) sintered pellets.

The sintered ferrites were also characterized by XRD. Fig. 4.23 shows the step scan XRD patterns of different sintered ferrite pellets along with that of the undoped calcined ferrite powder. All the compositions showed the presence of spinel as a major phase. La substituted samples (Fig. 4.23 (c)–(e)) showed the presence of  $\text{LaFeO}_3$  phase along with the major ferrite one. The intensity of  $\text{LaFeO}_3$  increased with the increase in La concentration. This apparently indicated that the La did not form a solid solution with spinel ferrite or  $\text{La}^{3+}$  had limited solid solubility.

One more interesting observation by slow step scanning was that a small unidentified phase peak appeared in the sintered undoped ferrite (Fig. 4.23 (b)). However, the above peak was not found in the calcined powder of the same (Fig. 4.23 (a)), as well as in the La substituted sintered pellets. Many investigators reported that NiCuZn ferrite

dissociated during sintering to precipitate Cu metal or its oxide [17, 35]. On this line, the peak was tried to match with Cu and/or Cu–O containing compounds.

The matching suggested that the peak might be corresponding to some Cu–O containing phase with composition between  $\text{Cu}_2\text{O}$ – $\text{Cu}_4\text{O}_3$ . The presence of Cu–O containing phase might be due to the surface oxidation of the precipitated Cu metal during sintering in air. The absence of that peak in the calcined powder was due to the lower heat treatment temperature of  $700^\circ\text{C}$  for 2 hrs of loose powder compared to high temperature sintering of compact pellets at  $900^\circ\text{C}$  for 4 hrs. It was interesting to note that the peak was absent in La substituted samples. This might be due to the solubility of Cu in  $\text{LaFeO}_3$  produced in the doped ferrites.

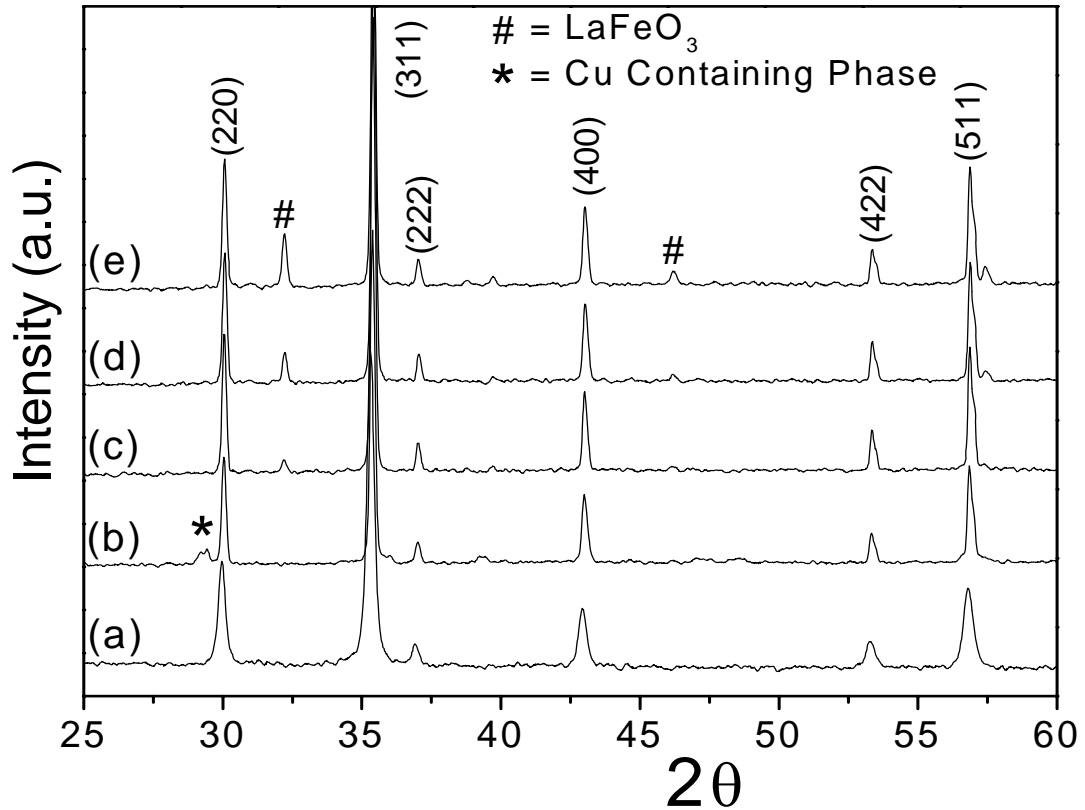


**Fig. 4.23.** XRD patterns of  $(\text{Ni}_{0.25}\text{Cu}_{0.2}\text{Zn}_{0.55})\text{La}_x\text{Fe}_{2-x}\text{O}_4$  ferrites (a) undoped calcined powder and sintered pellets of (b)  $x=0.0$ , (c)  $x=0.025$ , (d)  $x=0.05$  and (e)  $x=0.075$ .

#### 4.3.2.2 Densification and Microstructure

Table 4.5 shows the bulk density, apparent porosity of different sintered specimens along with their grain size. The bulk density and grain size increased with increasing La content which indicated improvement in densification and grain growth upon La substitution. The same behavior was found in MgCu ferrites [38]. Simultaneously, the apparent porosity decreased with La addition.

The increased densification in this case was due to the presence of excess Cu, Ni and Zn in the system. The excess Cu, Ni and Zn arose due to the La substitution for Fe in the ferrite, i.e. the La substituted compositions were Fe deficient with respect to undoped composition. As we have seen, La formed  $\text{LaFeO}_3$  in the system and it further absorbed some more Fe from the composition.

The net result was that the composition had non-stoichiometric excess Ni, Cu and Zn. This non-stoichiometry increased with the increase in %La substitution. It is known that the non-stoichiometric excess Ni, Cu and Zn are used for low temperature liquid phase sintering of the ferrites [17]. For this reason, the densification increased with La substitution.

**Table 4.5** Bulk density, apparent porosity and grain size, of sintered  $(\text{Ni}_{0.25}\text{Cu}_{0.2}\text{Zn}_{0.55})\text{La}_x\text{Fe}_{2-x}\text{O}_4$  ferrites with different La content.

(La-Content) “x”	Bulk Density (gm/cc)	Apparent Porosity (%)	Grain Size ( $\mu\text{m}$ )
x=0.0	4.61 (0.03)	11.6	0.65
x=0.025	4.85 (0.01)	2.3	0.88
x=0.05	4.98 (0.01)	1.3	0.92
x=0.075	5.04 (0.02)	1.2	1.17

Fig. 4.24 shows the microstructure of the sintered pellets. The undoped sample (Fig. 4.24 A) showed the presence of a monophasic spinel phase whereas, the La substituted materials showed (Fig. 4.24 B–D) a bi-phasic microstructure consisting of a

bigger matrix of ferrite grains and a smaller  $\text{LaFeO}_3$  secondary phase at the grain junctions/boundaries.

The EDX spectra (Fig. 4.25) obtained from the center of grain boundary  $\text{LaFeO}_3$  phase indicated the presence of mainly La, Fe and oxygen along with small amount of Cu, Ni and Zn. The grain size of ferrite matrix phase as well as the  $\text{LaFeO}_3$  phase increased with increasing the  $\text{La}^{3+}$  substitutions. The EDX spectra (Fig. 4.26) obtained from the center of La substituted NiCuZn ferrite grains indicated the presence of small concentration of La inside the grains.

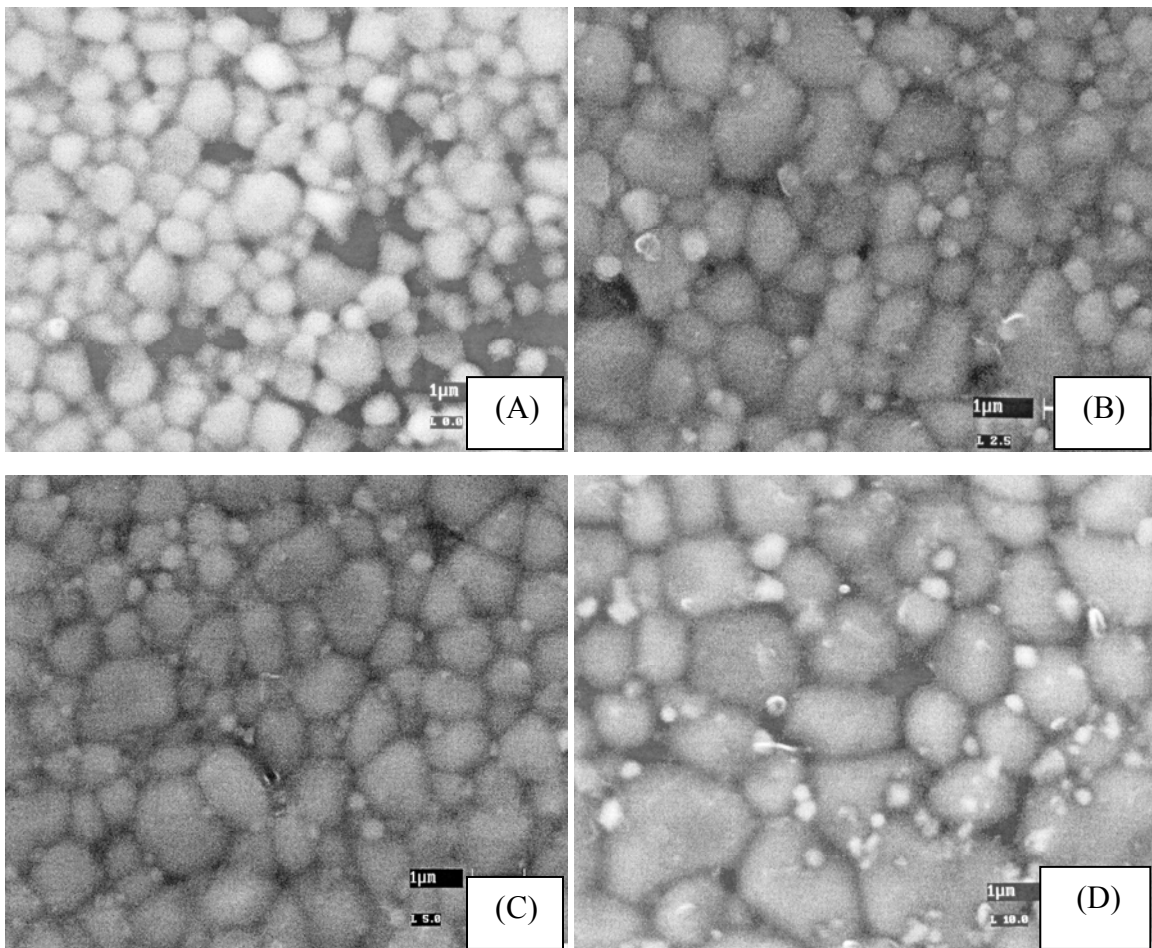


**Fig. 4.24.** SEM photographs of sintered  $(\text{Ni}_{0.25}\text{Cu}_{0.2}\text{Zn}_{0.55})\text{La}_x\text{Fe}_{2-x}\text{O}_4$  ferrites with (A)  $x=0.0$ , (B)  $x=0.025$ , (C)  $x=0.05$  and (D)  $x=0.075$ .

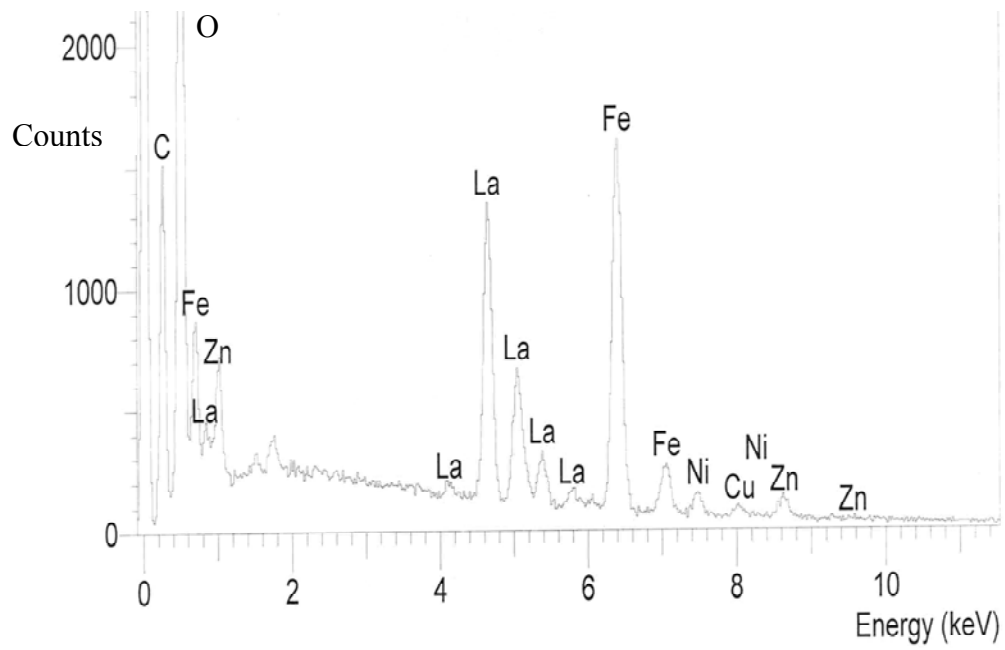


**Fig. 4.25.** EDX spectrum obtained from the center of grain boundary of  $\text{LaFeO}_3$  phase.

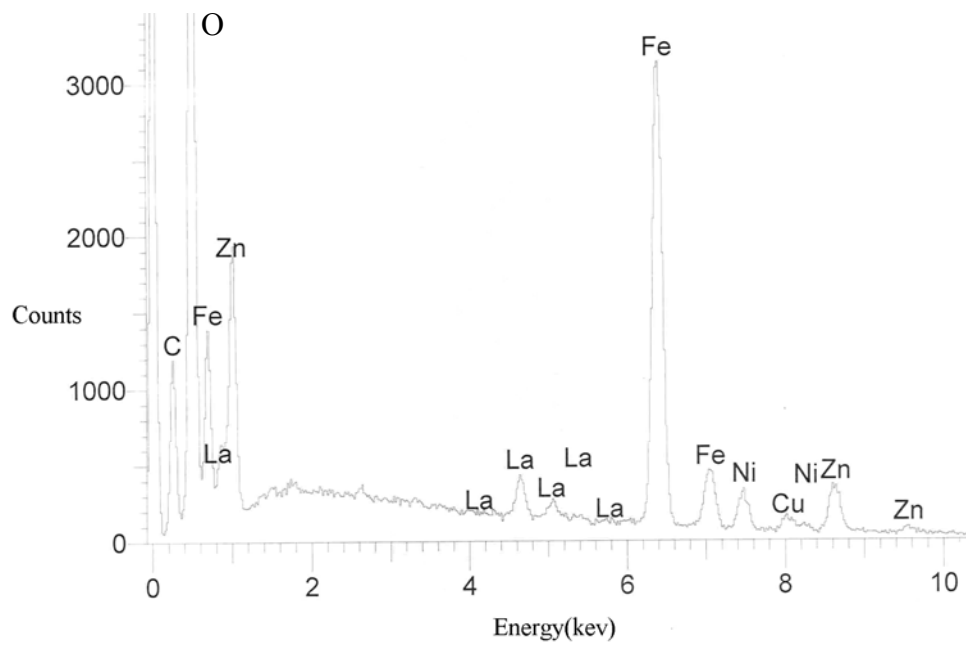


**Fig. 4.26.** EDX spectrum obtained from the center of La substituted NiCuZn ferrite grains.

### 4.3.2.3 Rietveld Analysis

The Rietveld structure refinement was carried out to determine the following:

(a) Amount of  $\text{LaFeO}_3$  formed (b) accurate lattice parameter (c) La-occupancy in the spinel lattice and (d) residual stress/strain in sintered ferrite, etc. XRD data for the refinement was obtained, as described in section 3.4.3, from sintered pellets to estimate actual stress/strain present in solid ferrite body.

The program MAUDWEB version 2.031 was used for the Rietveld refinement [141]. Fig. 4.27 and Fig. 4.28 shows the observed, calculated profiles and their differences after the refinement for two representative phases (spinel and  $\text{LaFeO}_3$ ) of composition  $x = 0.0$  and  $x = 0.075$  respectively.

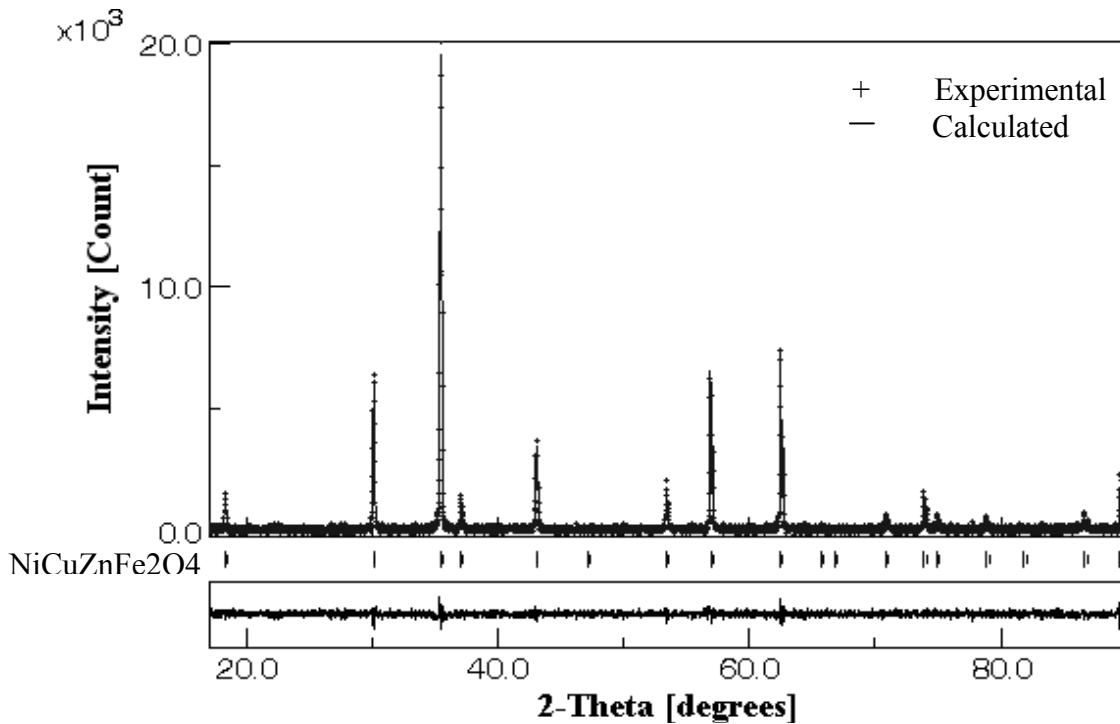


**Fig. 4.27.** Comparison between experimental (+) and calculated (-) X-ray diffraction pattern of  $(\text{Ni}_{0.25}\text{Cu}_{0.2}\text{Zn}_{0.55})\text{Fe}_2\text{O}_4$  ferrite fitted for spinel phases. Difference between the observed and the calculated pattern is given in the bar.

The refinements were very good yielding a low R-factor for all the compositions. Some important refined parameters are shown in Table 4.6 along with their refined cell parameter, crystallite size, micro-strain, macro-stress, % LaFeO<sub>3</sub> phase content. The cell edges  $a_0$ , were in the same range for different compositions. It has been reported that lattice constant increased by the incorporation of La in MgCu ferrites [38]. However, no significant increase in  $a_0$  was observed in the present experiment. There was a slight decrease in  $a_0$  for  $x = 0.025$  and slight increase for  $x = 0.075$  nominal compositions, respectively.

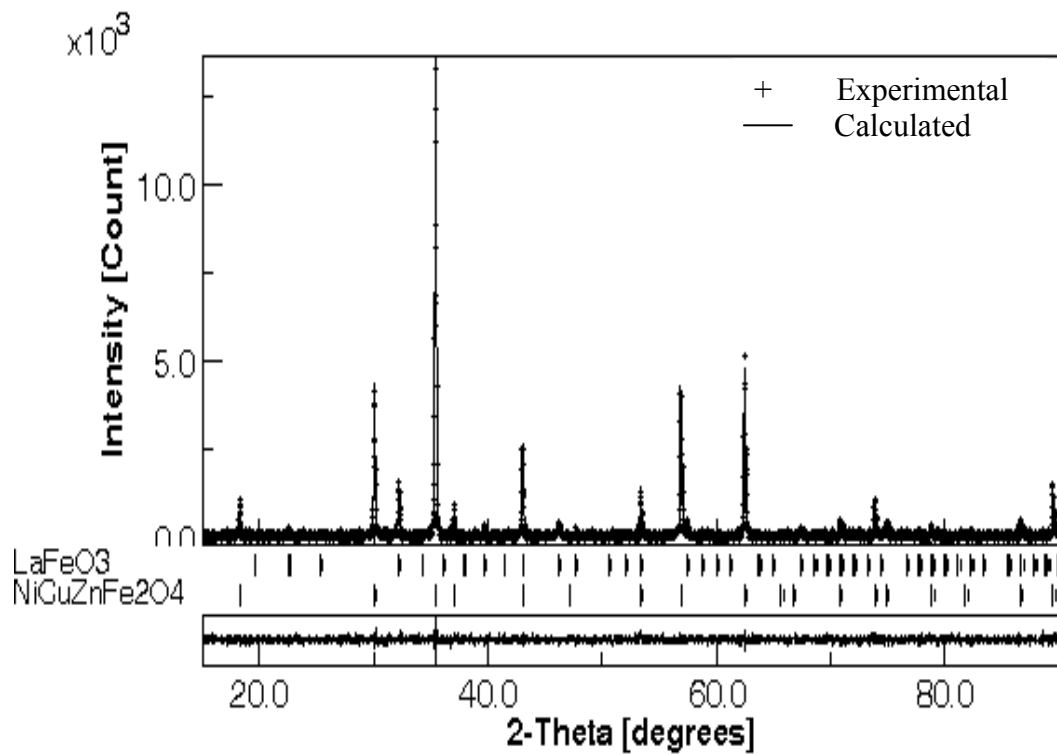


**Fig. 4.28.** Comparison between experimental (+) and calculated (-) X-ray diffraction pattern of  $(\text{Ni}_{0.25}\text{Cu}_{0.2}\text{Zn}_{0.55})\text{La}_{0.075}\text{Fe}_{1.925}\text{O}_4$  ferrite fitted for spinel and LaFeO<sub>3</sub> phases. Difference between the observed and the calculated pattern is given in the bar.

Crystallite size and micro-strains was refined using ‘Popa Line Broadening and Isotropic Size/strain’ model available in the MAUD program. Crystallite size was in the range 123–186 nm. It was interesting to note that the crystallite size (coherently scatter zone) of the ferrite (123 nm for undoped) increased by about 50%

(185 nm for  $x = 0.025$  composition) upon a small fraction of La substitution. There were no significant changes in r.m.s micro-strain in different pellet samples.

The macro-stresses present in the pellets were calculated using advanced ‘Triaxial Stress Isotropic E’ model available in the MAUD program. Significant differences in macro-stresses were found in La substituted pellets compared to undoped one. The macro-stress was more compressive (negative value) on La substituted pellets (except for  $x = 0.075$ ). That might be due to the compressive pressure exerted by the  $\text{LaFeO}_3$  present at the grain boundaries. A slightly lower  $a_0$  value was found in  $x = 0.025$  might be due to this compressive stress. A tensile macro-stress (positive value) was found in  $x = 0.075$  composition though it contained highest amount of  $\text{LaFeO}_3$  phase. A slight increase in lattice parameter of this composition might be due to the tensile stress.

**Table 4.6** Refined cell parameter, crystallite size, micro-strain, macro-stress, %  $\text{LaFeO}_3$  phase content, agreement factors (R-factors) and goodness of fit (G.O.F.) obtained from Rietveld fits for  $(\text{Ni}_{0.25}\text{Cu}_{0.2}\text{Zn}_{0.55})\text{La}_x\text{Fe}_{2-x}\text{O}_4$  ferrites with  $x = 0.0$ ,  $x=0.025$ ,  $x=0.05$  and  $x=0.075$ .

Parameters	Compositions			
	$x=0.0$	$x=0.025$	$x=0.05$	$x=0.075$
$a_0$ (Å)	8.4096	8.4004	8.4053	8.4112
Crystallite Size (nm)	123	186	152	158
r.m.s. micro-strain	$3.8 * 10^{-4}$	$3.17 * 10^{-4}$	$3.3 * 10^{-4}$	$3.2 * 10^{-4}$
Macro-stress (11)	$-3.7 * 10^{-9}$	-0.31	-0.30	0.033
% $\text{LaFeO}_3$	0%	1.34%	3.4%	5.4%
$R_{wp}$ (%)	2.04	1.76	1.82	1.81
$R_p$ (%)	1.58	1.39	1.43	1.44
G.O.F	1.15	1.09	1.10	1.08

Regarding  $\text{LaFeO}_3$  phase formation, if we considered La formed solely  $\text{LaFeO}_3$  without entering into the spinel lattice, then about 2.4, 5.0 and 7.4 wt%  $\text{LaFeO}_3$  should be formed in the compositions with  $x = 0.025$ , 0.05 and 0.075, respectively. However, the quantitative estimation (Table 4.6) shows slight by lower (1–2 wt %) amount of  $\text{LaFeO}_3$  in them. This might be due to the incorporation of remaining La into the spinel lattice and/or presence of small amorphous phase of it.



During structure refinement, it was found that the occupancy of octahedral site tended to increase above the permitted 16 atoms/unit cell for La substituted compositions. This might be due to the higher scattering factor at the sites. Since, Fe, Ni, Cu, etc. had almost equivalent scattering factors, there was some possibility of presence La having almost double scattering factor than others. Accordingly, octahedral occupancy was refined allowing La to occupy the site. However, the refinement yielded only about 0.05–0.08 La/unit cell occupancy. This was equivalent to about 1–2 wt% LaFeO<sub>3</sub>, which was not found in the quantitative estimation. The observation indicated that La had very low solubility in spinel lattice due to its bigger ionic radii. Lattice parameters values also suggested the same as there were very small changes in it.

#### 4.3.2.4 Electromagnetic Properties

Table 4.7 shows the initial permeability ( $\mu_i$ ), wall permeability ( $\mu_w$ ), rotational permeability ( $\mu_{rk}$ ) and anisotropy field ( $H_a$ ) of sintered ferrites along with their saturation magnetization ( $M_s$ ) which measured at room temperature. Fig. 4.29 shows the change in initial permeability of NiCuZn ferrite with different La substitution. It was interesting to note that the initial permeability significantly increased at  $x = 0.025$  of La substitution compared to that of undoped ones.

Similar increases in permeability of CuZn ferrites with Sm substitution for Fe were also reported by *Sattar et al.* [97]. La<sup>3+</sup> has no unpaired electrons and it behaves as diamagnetic. The substitution of ferromagnetic Fe<sup>3+</sup> ( $5\mu_B$ ) by diamagnetic La<sup>3+</sup> in the spinel was not useful for increasing permeability. It had been suggested that the substitution of Sm<sup>3+</sup> ion moved Cu<sup>2+</sup> and Zn<sup>2+</sup> ion from ‘B’ to ‘A’ site causing ‘A’ sub lattice dilution and increased the magnetic permeability in CuZn ferrites [98].

**Table 4.7** Permeability, wall permeability ( $\mu_w$ ), rotational permeability ( $\mu_{rk}$ ), anisotropy field ( $H_a$ ) and saturation magnetization ( $M_s$ ) of  $(\text{Ni}_{0.25}\text{Cu}_{0.2}\text{Zn}_{0.55})\text{La}_x\text{Fe}_{2-x}\text{O}_4$  ferrite with different La content.

(La-Content) "x"	Permeability ( $\mu_i$ )	$\mu_w$	$\mu_{rk}$	$H_a$ (Oe)	$M_s$ (emu/gm)
x=0.0	202	189.42	12.58	197.60	59.26
x=0.025	424	406.93	17.07	167.76	66.37
x=0.05	249	234.01	11.99	202.80	53.45
x=0.075	198	177.21	11.79	204.76	52.31

However, in the present case  $\text{La}^{3+}$  incorporation into the lattice was very small ( $\sim 0.1$  atom/unit cell) and hence the increased permeability was not due to its incorporation. The increased permeability at  $x = 0.025$  compared to undoped one might be due to the following reasons: (a) increased grain size, a specially increased crystallite size; (b) increased density as well as decreased porosity; (c) decreased magneto-crystalline anisotropy; (d) change in stress and (e) absence of the Cu-containing non-magnetic precipitated compound due to the solid-solution formation of Cu in  $\text{LaFeO}_3$ , etc.

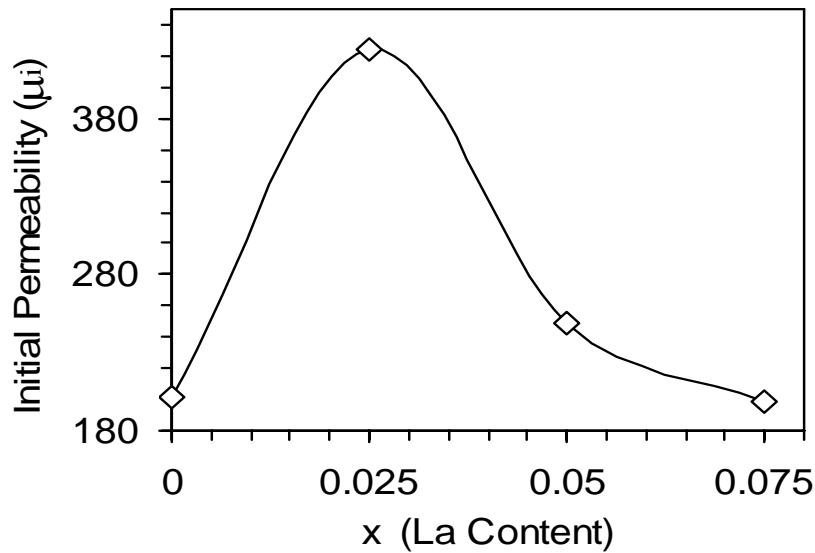


**Fig. 4.29.** Initial Permeability as a function of La substitution in  $(\text{Ni}_{0.25}\text{Cu}_{0.2}\text{Zn}_{0.55})\text{La}_x\text{Fe}_{2-x}\text{O}_4$  ferrites.

It is well established that the permeability increases with the increase in density, grain size and with the decrease in porosity in polycrystalline ferrite as per equation (4.2). The initial permeability of ferrite is usually expressed as equation (4.6). The initial permeability was strongly influenced by anisotropy, magnetostriction constant and stress.

The La-substituted compositions were deficient in Fe and hence  $\text{Fe}^{2+}$  ions were expected to be at minimum. The magnetic anisotropy was also expected to decrease. Because magnetic anisotropy field in ferrites results mainly from  $\text{Fe}^{2+}$  ions [140]. This decrease in anisotropy increases the permeability. The compressive macro-stress (Table 4.6) in  $x = 0.025$  composition was higher than undoped one. The stress in the undoped sample might be considered as zero (as in the order of  $10^{-8}$ ). A compressive stress can increase the initial permeability of ferrite with negative magnetostriction [43]. So the increased permeability in  $x = 0.025$  composition was due to the higher compressive stress prevailing in the sample.

However, the permeability decreased with higher La ( $x > 0.025$ ) substitution. This might be due to the presence of higher amount  $\text{LaFeO}_3$  phase. One more reason might be the change in macro-stress. As stated earlier, a tensile macro-stress was found in  $x = 0.075$  specimen and the decreased permeability was due to that tensile stress [43].

Fig. 4.30 shows the frequency dependence of permeability in different compositions. The permeability of  $x = 0.025$  composition was stable in the frequency range 100 kHz to 2 MHz and its dispersion occurred above 2 MHz. The dispersions of the other compositions were at higher frequency compared to  $x = 0.025$  composition. The dispersion behavior could be explained by equation (4.4), and followed Snoek's law that cut-off frequency is inversely proportional to that magnetic permeability. So, lowest cut-off frequency of  $x = 0.025$  composition was due to its highest permeability among all.

Fig. 4.31 shows the magnetic hysteresis curve for  $(\text{Ni}_{0.25}\text{Cu}_{0.2}\text{Zn}_{0.55})\text{La}_x\text{Fe}_{2-x}\text{O}_4$  ferrites. The saturation magnetization of nominal composition at  $x = 0.025$  was higher than that of the undoped one. This might be due to

better density and higher permeability of the doped ferrite.  $M_s$  value of compositions at  $x = 0.05$  and  $0.075$  were lower than at  $x = 0.025$  composition. This might be due to the presence of higher quantity of nonmagnetic  $\text{LaFeO}_3$  in  $x = 0.05$  and  $0.075$  compositions.

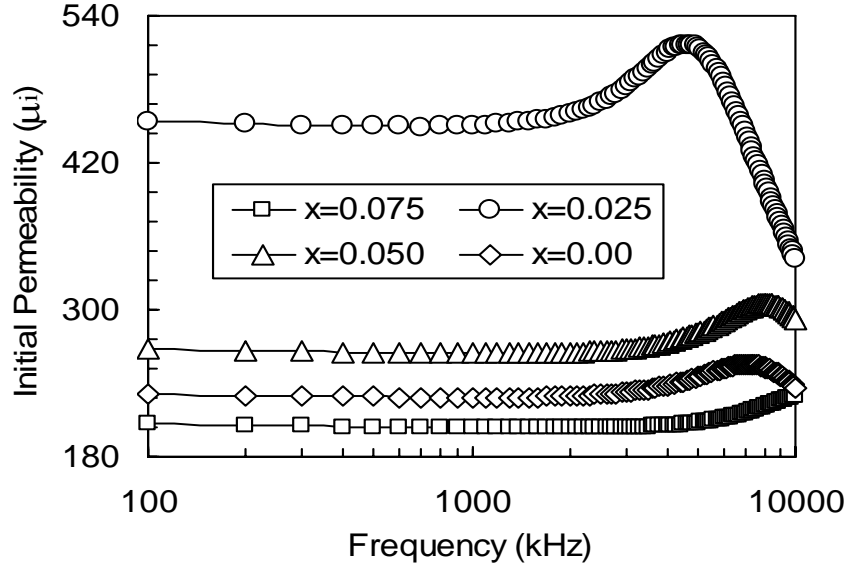


**Fig. 4.30.** Frequency dependence of permeability in  $(\text{Ni}_{0.25}\text{Cu}_{0.2}\text{Zn}_{0.55})\text{La}_x\text{Fe}_{2-x}\text{O}_4$  ferrites with different La content.

The two main magnetization mechanisms are wall displacement and spin rotation [134]. The values of rotational permeability ( $\mu_{rk}$ ) have been calculated as per [43] using;

$$\mu_{rk} = 1 + \frac{8\pi M_s}{3H_a} \quad (4.7)$$

and the anisotropy field ( $H_a$ ) is calculated as per [142] using;

$$H_a = \frac{2K_1}{M_s} \quad (4.8)$$

where,  $M_s$  is the saturation magnetization,  $K_1$  is the anisotropy constant which was taken as  $-K_1 = 2.70 \times 10^4 \text{ erg/cm}^3$  [28] for all the compositions, considering no La solubility in the spinel ferrite structure.

The calculated values of rotational permeability ( $\mu_{rk}$ ), wall permeability ( $\mu_w$ ) and anisotropy field ( $H_a$ ) for different compositions are given in Table 4.7. It is evident from the Table 4.7 that the magnitudes of wall permeability are larger in comparison to rotational permeability. So, wall permeability dominated the magnetization mechanism.

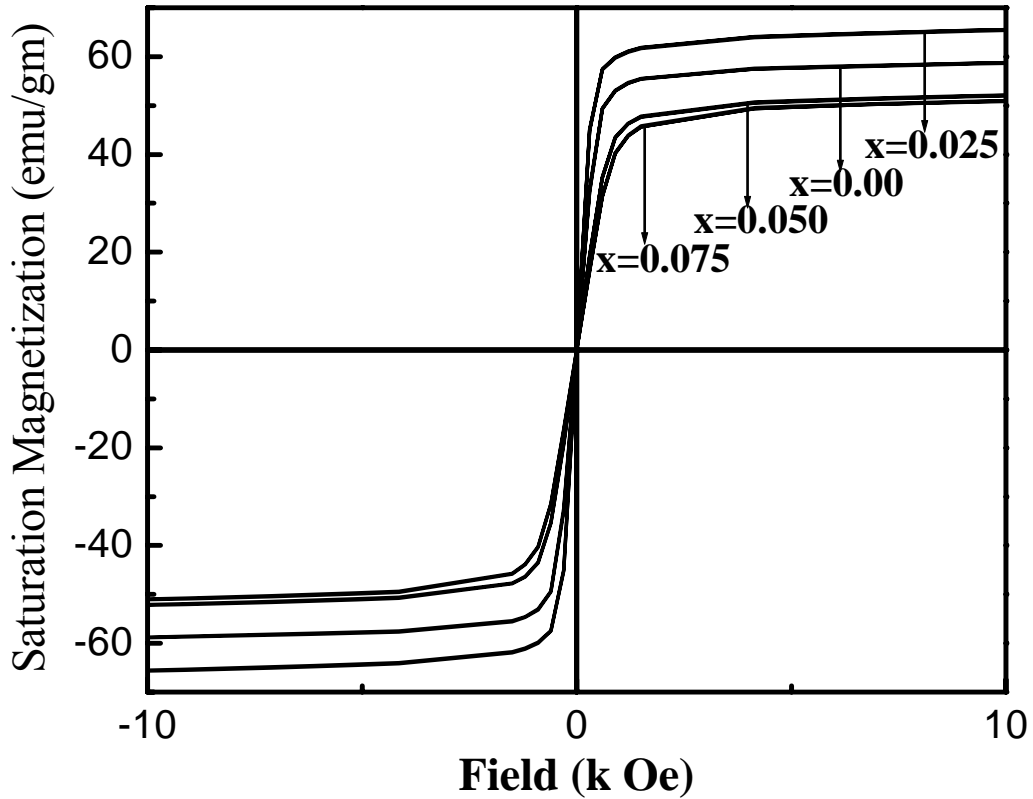


**Fig. 4.31.** Magnetic hysteresis curve for  $(\text{Ni}_{0.25}\text{Cu}_{0.2}\text{Zn}_{0.55})\text{La}_x\text{Fe}_{2-x}\text{O}_4$  ferrites with different La content measured at room temperature.

Table 4.8 shows the coercive field ( $H_c$ ), Curie temperature of sintered ferrites along with their resistivity. All compositions exhibited low coercivity values, which was typical of soft ferrite. Coercivity increased in  $x = 0.025$  composition compared to undoped sample, which might be due to an extrinsic effect associated with a favorable microstructure in the sample [143]. Since coercivity was the micro-structural property, it depended upon defects, strains, non-magnetic atoms etc. in the material. However, the coercivity ( $H_c$ ) decreased with further La addition. This might be due to the higher grain

size (Table 4.5) in later two compositions, as it is known,  $H_c$  decreases with increasing grain size.

**Table 4.8** Coercive field ( $H_c$ ), Curie temperature and resistivity of  $(\text{Ni}_{0.25}\text{Cu}_{0.2}\text{Zn}_{0.55})\text{La}_x\text{Fe}_{2-x}\text{O}_4$  ferrites with different La content.

(La-Content) "x"	$H_c$ (Oe)	Curie Temperature (°C)	Resistivity (* $10^6$ ohm-cm) at 100kHz
x=0.0	0.74	185	3.9
x=0.025	2.22	190	69
x=0.05	0.51	185	61
x=0.075	0.45	187	42

The change in Curie temperature of the ferrite with La substitution was also evaluated. Fig. 4.32 shows the temperature dependence of permeability in different compositions. No significant change in Curie temperature (Table 4.8) was found with La substitution. This again indicated that La had very low solubility in spinel ferrite.

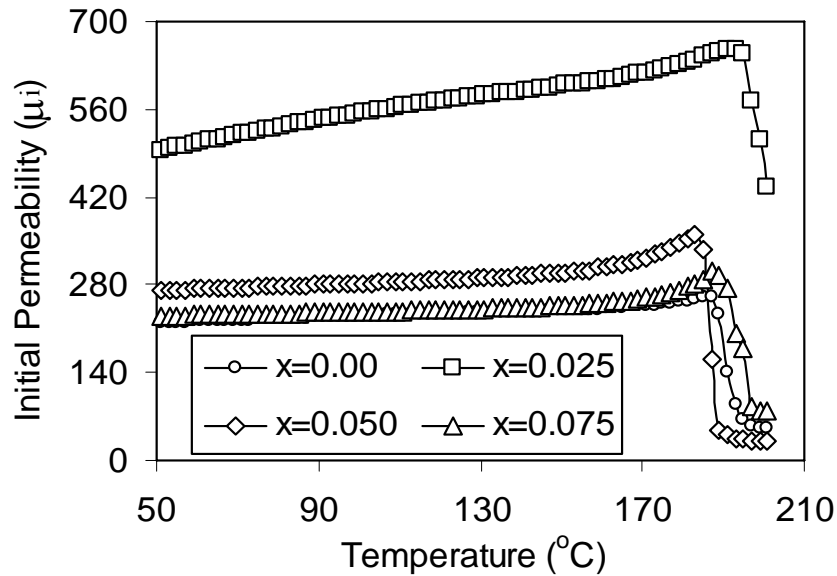


**Fig. 4.32.** Temperature dependency of permeability in  $(\text{Ni}_{0.25}\text{Cu}_{0.2}\text{Zn}_{0.55})\text{La}_x\text{Fe}_{2-x}\text{O}_4$  ferrites with different La content.

Resistivity of the ferrite (Table 4.8) increased with increase in La-content with respect to undoped ferrite. It is well known that the magnetic anisotropy field in ferrites results mainly from the presence of  $\text{Fe}^{+2}$  ions [140]. The anisotropy field (Table 4.7) for  $x = 0.025$  composition was lower than the undoped sample, i.e.  $\text{Fe}^{+2}$  ion concentration was lower for this composition. Decreased  $\text{Fe}^{+2}$  ionic concentrations might be attributed due to the formation of secondary  $\text{LaFeO}_3$  phases. The crystallization of  $\text{LaFeO}_3$  phase on the grain boundaries impeded the reduction of  $\text{Fe}^{+3}$  ions inside the grains. That's why the  $x = 0.025$  composition had higher resistivity compared to undoped ferrite. A small decrease in resistivity in  $x = 0.05$  and  $0.075$  compositions was due to the increase in grain size (Table 4.5). As it is known, larger grains result in less number of grain boundaries, which act as scattering center for the flow of electrons and therefore decrease of resistivity.

Fig. 4.33 shows the relative loss factor (RLF) i.e. the ratio of the magnetic loss tangent to the initial permeability of different cores. It was revealed from the figure that the RLF of La substituted ferrites were lower than undoped one up to 2 MHz.

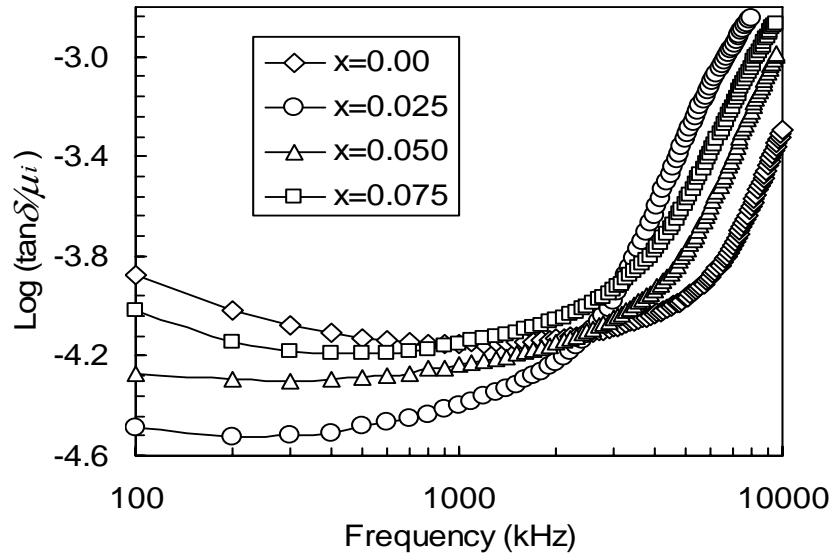


**Fig. 4.33.** Relative loss factor as a function of frequency in  $(\text{Ni}_{0.25}\text{Cu}_{0.2}\text{Zn}_{0.55})\text{La}_x\text{Fe}_{2-x}\text{O}_4$  ferrites with different La content.

The predominant losses in ferrites were due to hysteresis and eddy current losses at operating frequency lower than the relaxation frequency of wall displacement.

The hysteresis loss depends on many parameters like magnetostriction constant, magneto-crystalline anisotropy, saturation magnetization and microstructure. The eddy current loss mainly depends on the electrical resistivity of the ferrite. So, it might be considered that the lowering of RLF in La-substituted compositions resulted mainly from a reduction in eddy current loss due to their higher electrical resistivity.

The undoped ferrite showed highest RLF in 100 to 1000 kHz zone. This might be due to its higher porosity and lower resistivity [136]. The RLF of all the cores increased in MHz frequency zone due to the relaxation losses.

### 4.3.3 Summary

It may be concluded that the substitution of La for Fe in NiCuZn ferrite mainly produce secondary phase  $\text{LaFeO}_3$ . An amorphous  $\text{LaFeO}_3$  phase was formed during nitrate-citrate auto combustion synthesis of the substituted ferrites and the crystallinity of it increased upon successive heat treatments. Bulk density and grain size of the ferrites increased with the increase in La substitution mainly due to the increase in non-stoichiometric composition.

A Cu-containing oxide phase was found to precipitate during sintering of undoped NiCuZn ferrite. However, that Cu-containing phase was not found in La substituted ferrite due to the solid solution formation of Cu within  $\text{LaFeO}_3$ . A significant increase in initial permeability and saturation magnetization of the ferrite was found at small fraction of La ( $x = 0.025$ ) substitution. The increased permeability was due to the combined effect of increased grain size, specially increased crystallite size, increased densification (decreased porosity), decreased anisotropy and compressive macro-stress. The La solubility in the ferrite lattice was found very low ( $\sim 0.1$  atom/unit cell).

The AC resistivity of the composition also increased due to the lowering of  $\text{Fe}^{+2}$  ion concentration by the formation of  $\text{LaFeO}_3$  phase at the grain boundary. The relative loss factor of the specific composition at  $x = 0.025$  was lower due to the higher electrical resistivity as well as the higher initial permeability. The magnetic loss was stable in the frequency range 100 kHz to 1 MHz.



## 4.4 Effect of Sm substitution on structural and electromagnetic properties of $(\text{Ni}_{0.25}\text{Cu}_{0.2}\text{Zn}_{0.55})\text{Fe}_2\text{O}_4$ ferrite

### 4.4.1 Introduction

$\text{Sm}^{3+}$  was substituted for  $\text{Fe}^{3+}$  in  $(\text{Ni}_{0.25}\text{Cu}_{0.2}\text{Zn}_{0.55})\text{Sm}_x\text{Fe}_{2-x}\text{O}_4$  ferrites with  $x = 0.025, 0.05$  and  $0.075$ . Sm was substituted as it showed a significant increase in relative permeability in CuZn ferrite [98]. Ferrite compositions were synthesized through sol-gel auto combustion process. Details experimental procedure has been illustrated in experimental chapter (section 3.1.2, 3.3).

Briefly to prepare 20 gm  $(\text{Ni}_{0.25}\text{Cu}_{0.2}\text{Zn}_{0.55})\text{Sm}_x\text{Fe}_{2-x}\text{O}_4$  ferrite with  $x = 0.0, 0.025, 0.05$  and  $0.075$  compositions, 0.0208, 0.0207, 0.0206 and 0.0204 mol nickel nitrate; 0.0166, 0.0165, 0.0164 and 0.0163 mol copper nitrate; 0.0460, 0.0456, 0.0452 and 0.0448 mol zinc nitrate; 0.1672, 0.1638, 0.1604 and 0.1569 mol ferric nitrate; 0, 0.00207, 0.00412 and 0.00612 mol samarium nitrate; 0.2506, 0.2488, 0.2467 and 0.2446 mol citric acid were taken respectively. The effect of  $\text{Sm}^{3+}$  substitution on the density, microstructure, permeability, magnetic losses, resistivity and saturation magnetization of the ferrite were investigated.

### 4.4.2 Results and Discussion

#### 4.4.2.1 Phase Analysis

The Sm substituted NiCuZn ferrites were extensively characterized by XRD. Fig. 4.34 shows the XRD patterns of the as-burnt ferrite powders. The phase analysis revealed that the as burnt ferrite powders were crystalline (JCPDS card number 08-0234) in nature and contained spinel ferrite phase. The broad peaks in XRD patterns indicated fine crystallite size of the ferrites.

The crystallite size was calculated from full width at half maximum of the [311] peak using Scherer formula. The crystallite size of as-burnt powders was in the range 17-20 nm. The as burnt powders were calcined at  $\approx 700^\circ\text{C}$  for 2 hrs to get more crystalline homogeneous spinel phase. The crystallite size of calcined powders was in the

range 29-33 nm. Surface area of as burnt and calcined powders was found to be in the range of 37-42 and 26-34 m<sup>2</sup>/gm respectively.

To identify the possible formation of a second phase (SmFeO<sub>3</sub>) in the substituted ferrites, the slow step scan XRD analyses were conducted on the samples after different stages of processing. Fig. 4.35 shows the step scan XRD patterns of different sintered ferrite pellets. The most intense peaks in all the specimens were found to match well with the spinel ferrite structure. Samarium iron oxide, SmFeO<sub>3</sub> phase was detected in all Sm-substituted ferrites. The amount of SmFeO<sub>3</sub>, that is its' peak intensity increased with increasing Sm concentration. This apparently indicated that Sm did not form a solid solution with spinel ferrites or it had very small solid solubility.

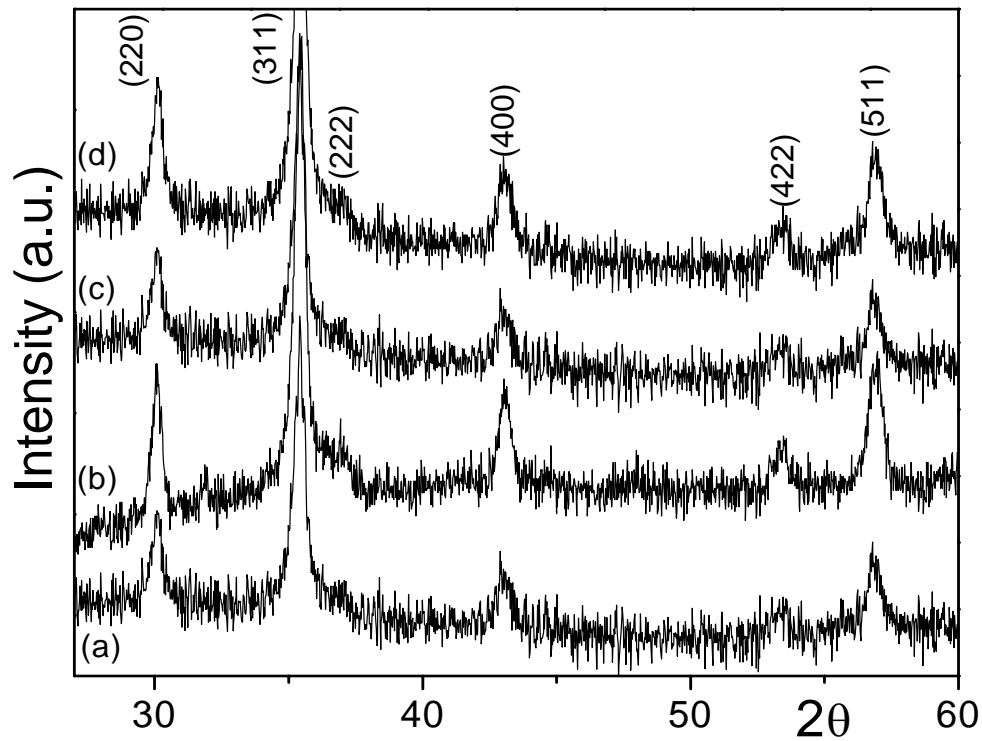


**Fig. 4.34.** XRD patterns of the as-burnt (Ni<sub>0.25</sub>Cu<sub>0.2</sub>Zn<sub>0.55</sub>)Sm<sub>x</sub>Fe<sub>2-x</sub>O<sub>4</sub> ferrites with (a) x =0.0, (b) x=0.025, (c) x=0.05 and (d) x=0.075.

A small amount of unknown phase was found in the un-substituted ferrite. The peak was tried to match with Cu and/or Cu–oxygen containing compounds. The matching suggested that the peak might be corresponding to some compound in between

$\text{Cu}_2\text{O}$ – $\text{Cu}_4\text{O}_3$ . Many investigators reported that NiCuZn ferrites dissociated during sintering to precipitate Cu metal or its oxides [17, 35]. The presence of Cu-oxygen containing phase might be due to surface oxidation of that precipitated Cu metal during sintering in air. It is interesting to note that the Cu containing compound was absent in all Sm substituted specimen. This might be due to the solubility of precipitated Cu in  $\text{SmFeO}_3$ .

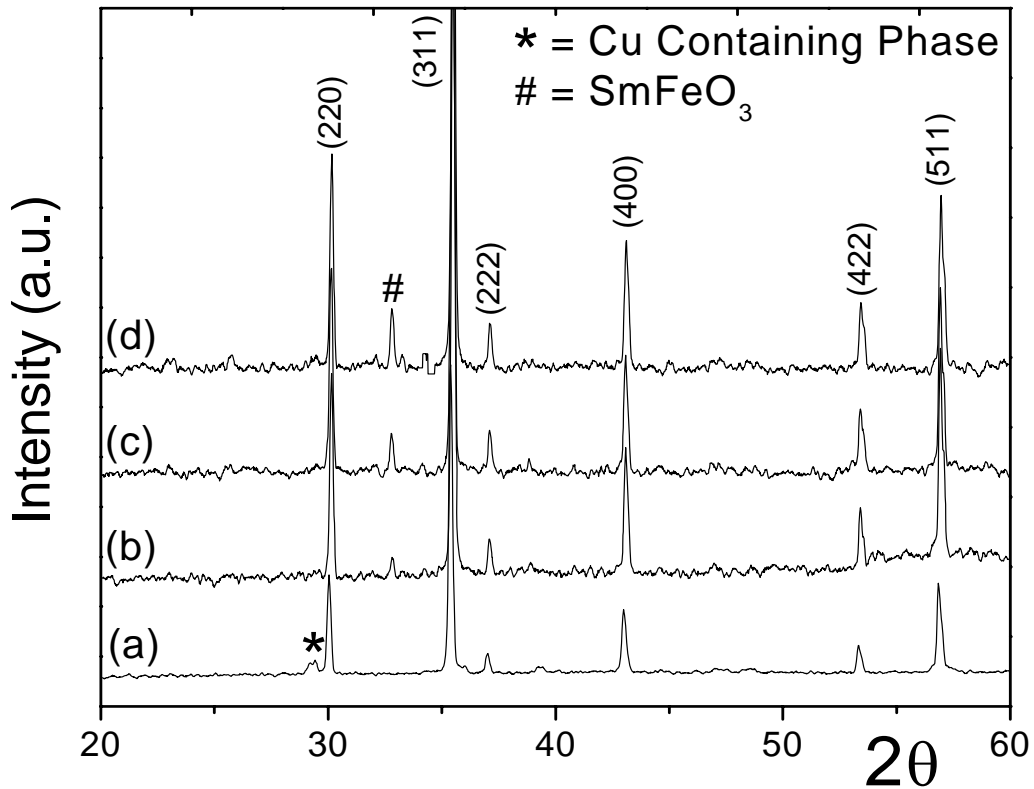


**Fig. 4.35.** XRD patterns of sintered  $(\text{Ni}_{0.25}\text{Cu}_{0.2}\text{Zn}_{0.55})\text{Sm}_x\text{Fe}_{2-x}\text{O}_4$  ferrites with different Sm content (a)  $x = 0.0$ , (b)  $x = 0.025$ , (c)  $x = 0.05$  and (d)  $x = 0.075$ .

Table 4.9 shows the crystallite size and lattice parameters of sintered ferrite specimens along with their bulk density, apparent porosity and grain size. Crystallite size increased with Sm substitution due to improved densification and grain growth. There was a minor decrease in lattice parameter  $a_0$  of NiCuZn ferrite with Sm substitution, which might be due to the compressive pressure exerted on the ferrite lattice by  $\text{SmFeO}_3$ .

**Table 4.9** Crystallite size, lattice parameter, bulk density, apparent porosity, and grain size of sintered  $(\text{Ni}_{0.25}\text{Cu}_{0.2}\text{Zn}_{0.55})\text{Sm}_x\text{Fe}_{2-x}\text{O}_4$  ferrites with different Sm content.

(Sm-Content) "x"	Crystallite Size (nm)	Lattice Parameter (Å)	Bulk Density (gm/cc)	Apparent Porosity (%)	Grain Size ( $\mu\text{m}$ )
x = 0.0	102	8.429	3.75 (0.03)	11.4	0.42
x = 0.025	170	8.403	5.06 (0.02)	6.36	1.18
x = 0.05	184	8.392	5.15 (0.01)	6.35	1.21
x = 0.075	156	8.384	5.01 (0.01)	9.35	0.95

#### 4.4.2.2 Densification and Microstructure

Fig. 4.36 shows the bulk density and grain size of  $(\text{Ni}_{0.25}\text{Cu}_{0.2}\text{Zn}_{0.55})\text{Sm}_x\text{Fe}_{2-x}\text{O}_4$  ferrites with different Sm-content. The density of sintered specimen increased upon Sm substitution, indicating an improved densification with the substitution. A similar trend was reported by *Costa et al.* [96] for Sm substituted NiZn ferrites.

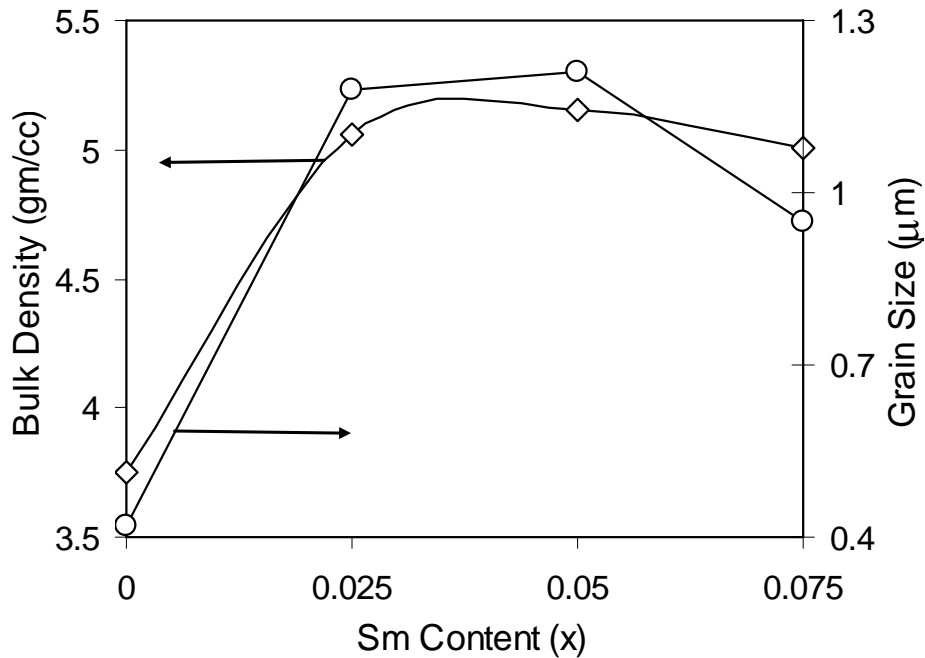


**Fig. 4.36.** Bulk density and grain size of sintered  $(\text{Ni}_{0.25}\text{Cu}_{0.2}\text{Zn}_{0.55})\text{Sm}_x\text{Fe}_{2-x}\text{O}_4$  ferrites with different Sm content.

Increased densification might be due to the evolution of excess Cu, Ni and Zn in the composition as Sm was substituted for Fe. Sm further took some Fe to form  $\text{SmFeO}_3$ . So, the net result of Sm substitution was to create non-stoichiometry in composition. It is known that, non-stoichiometric excess Ni, Cu and Zn are often used for low temperature liquid phase sintering of the ferrites [17]. For this reason, the densification increased with Sm substitution.

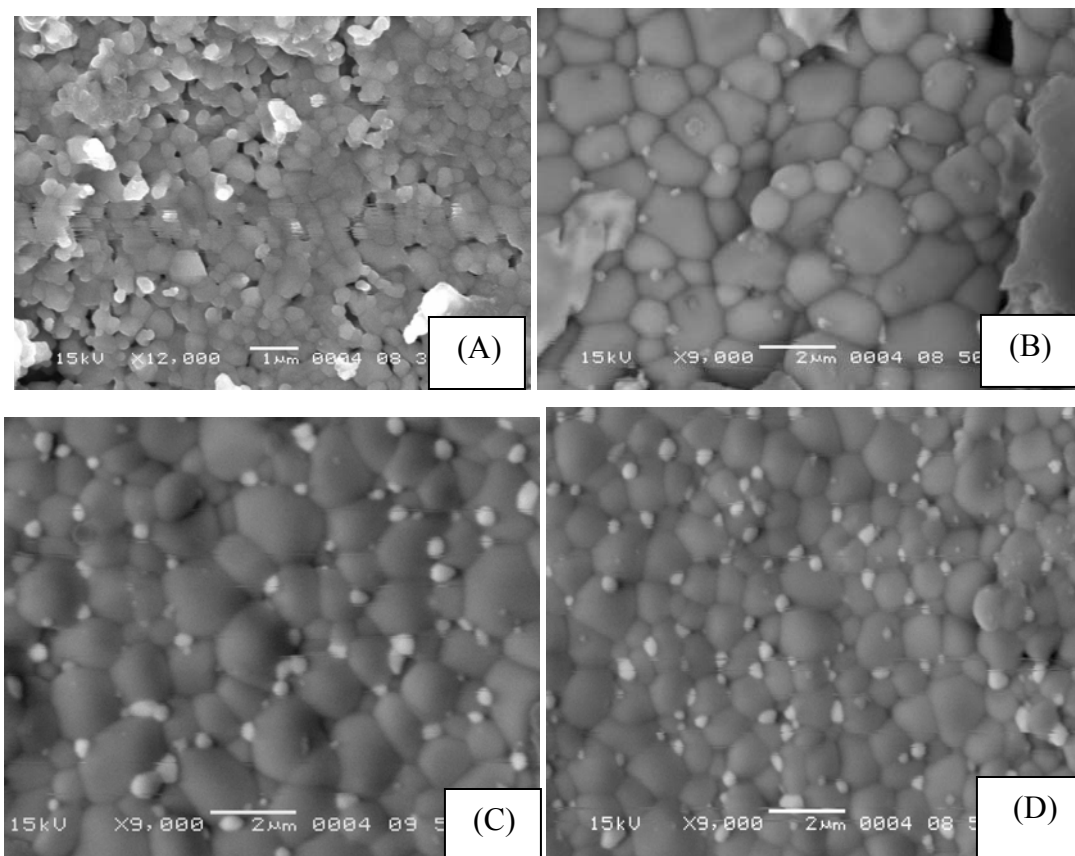
Fig. 4.37 shows the microstructure of sintered specimen. Un-substituted specimen (Fig. 4.37A) showed the presence of a monophasic homogeneous microstructure with an average grain size  $0.42 \mu\text{m}$  whereas, Sm doped specimens (Fig. 4.37 B, C, D) showed a bi-phasic microstructure constituted of dark ferrite matrix grains and small whitish grain at the grain junction/boundary.

EDX spectra (Fig. 4.38) obtained from the center of whitish grain confirmed the presence of Sm, Fe, oxygen and minor amount of Cu, Ni and Zn. This indicated whitish grains were  $\text{SmFeO}_3$ . The amount of  $\text{SmFeO}_3$  was maximum at  $x = 0.075$  composition. The grain size of matrix phase was maximum at  $x = 0.05$  composition. Relatively lower grain size of ferrite matrix at  $x = 0.075$  composition (Fig. 4.37 D) might be due to the grain growth inhibition caused by  $\text{SmFeO}_3$  [96].

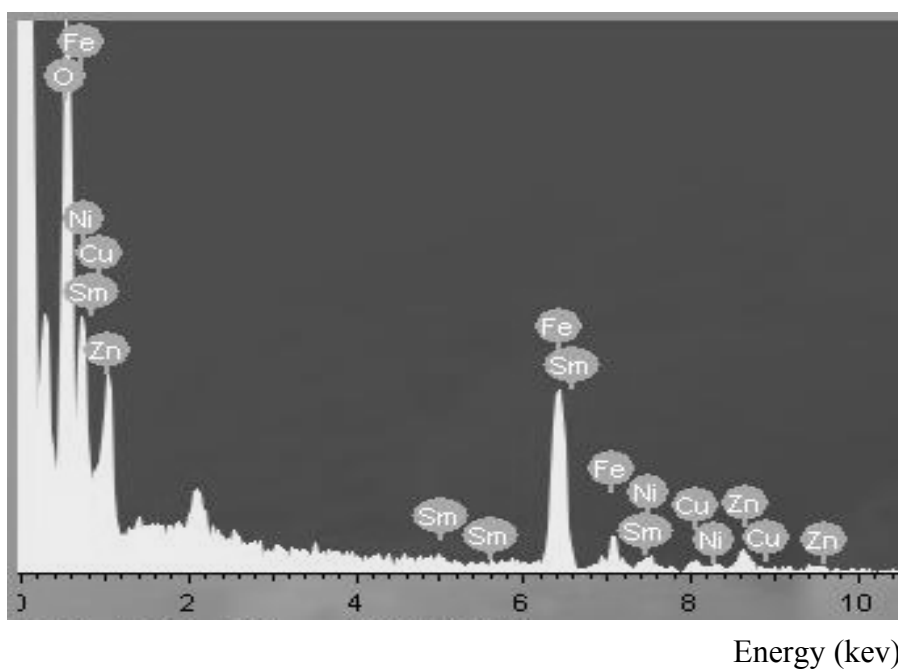
#### 4.4.2.3 Electromagnetic Properties

Fig. 4.39 shows the initial permeability as a function of Sm substitution in  $(\text{Ni}_{0.25}\text{Cu}_{0.2}\text{Zn}_{0.55})\text{Sm}_x\text{Fe}_{2-x}\text{O}_4$  ferrites. Table 4.10 shows the permeability, saturation magnetization and Curie temperature of sintered ferrites along with their resistivity. The permeability increased with increasing Sm-substitution with a maximum at  $x = 0.05$  and then decreased at  $x = 0.075$  composition.

It is well established that permeability of polycrystalline ferrite increases with increasing density and grain size. Increase in permeability with Sm-substitution might primarily be attributed to the increase in bulk density. An increase in the density, not only results in the reduction of demagnetizing field due to the reduction of pores but



**Fig. 4.37.** SEM images of sintered  $(\text{Ni}_{0.25}\text{Cu}_{0.2}\text{Zn}_{0.55})\text{Sm}_x\text{Fe}_{2-x}\text{O}_4$  ferrites with different Sm-content (A)  $x=0.0$ , (B)  $x=0.025$ , (C)  $x=0.05$  and (D)  $x=0.075$ .



**Fig. 4.38.** EDX spectrum obtained from the center of grain boundary of  $\text{SmFeO}_3$  phase.

also raises the spin rotational contribution, which in turn increase the permeability [53]. However, the lowering of permeability at  $x = 0.075$  specimen might be due to the formation of significant amount of non-magnetic  $\text{SmFeO}_3$  phase and decreased grain size (Table 4.9) in the ferrites.

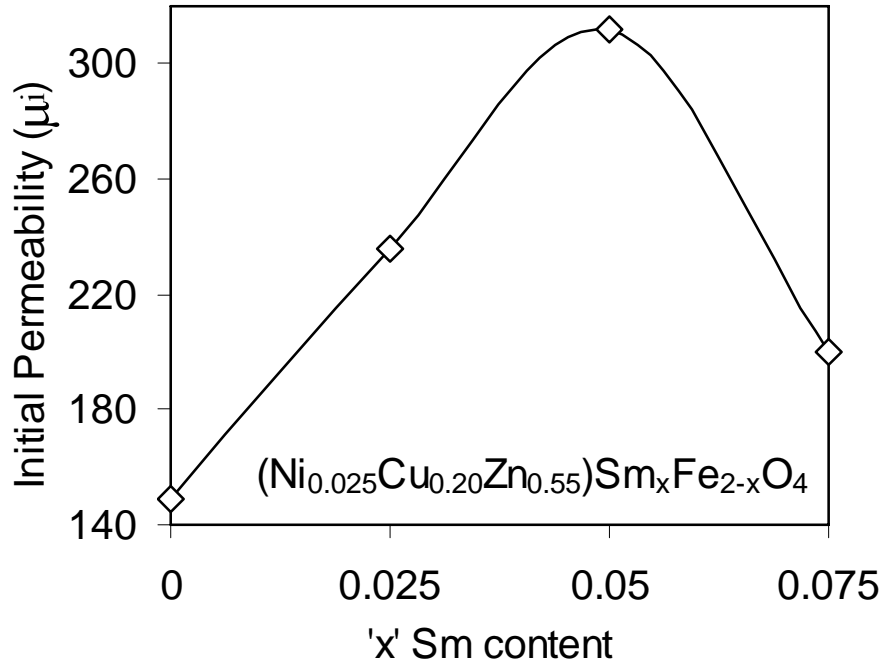
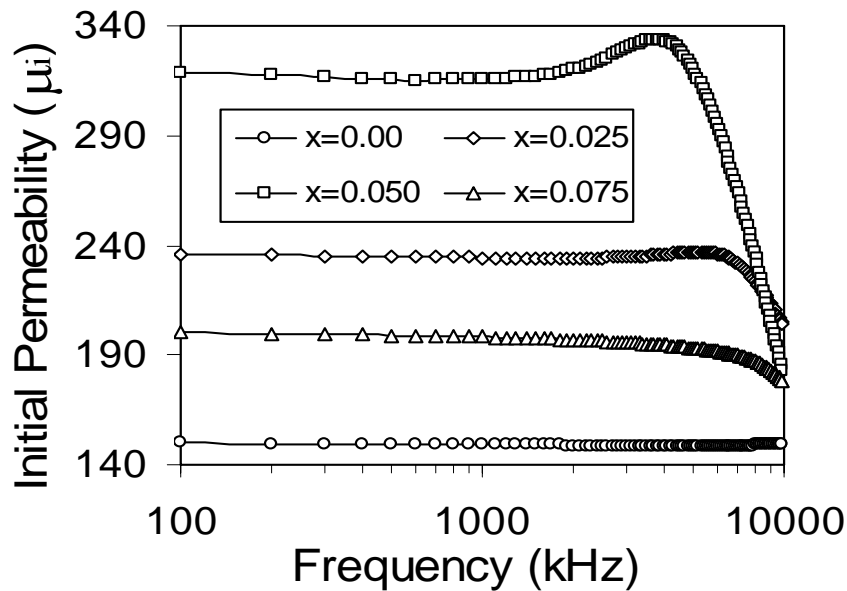


**Fig. 4.39.** Permeability as a function of Sm-substitution in  $(\text{Ni}_{0.25}\text{Cu}_{0.2}\text{Zn}_{0.55})\text{Sm}_x\text{Fe}_{2-x}\text{O}_4$  ferrites.

**Table 4.10** Permeability, saturation magnetization, Curie temperature and resistivity of sintered  $(\text{Ni}_{0.25}\text{Cu}_{0.2}\text{Zn}_{0.55})\text{Sm}_x\text{Fe}_{2-x}\text{O}_4$  ferrites with different Sm-content.

(Sm-Content) "x"	Permeability ( $\mu_i$ )	Saturation Magnetization (emu/gm)	Curie Temperature ( $^{\circ}\text{C}$ )	Resistivity ( $*10^6 \Omega\text{-cm}$ ) at 100 kHz
x =0.0	150	59.26	185	3.3
x =0.025	236	65.80	187	27
x =0.05	312	69.97	192	54
x =0.075	200	62.05	188	21

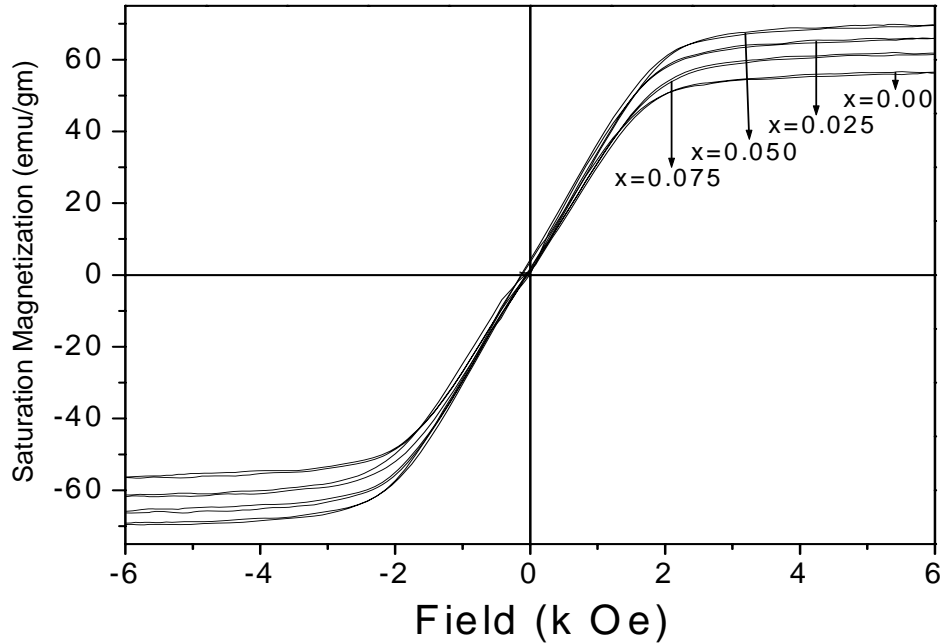
Fig. 4.40 shows the frequency dependence of permeability of the  $(\text{Ni}_{0.25}\text{Cu}_{0.2}\text{Zn}_{0.55})\text{Sm}_x\text{Fe}_{2-x}\text{O}_4$  ferrites. The permeability at  $x = 0.05$  composition was stable in the frequency range 100 kHz to 2 MHz and its dispersion occurred above 2 MHz. The dispersions of the other compositions were at higher frequency compared to that at  $x = 0.05$  composition. The dispersion behavior could be explained by equation (4.4), and followed Snoek's law that cut-off frequency is inversely proportional to the magnetic permeability. So, the lowest cut-off frequency at  $x = 0.05$  composition was due to its highest permeability among all.



**Fig. 4.40.** Frequency dependency of permeability in  $(\text{Ni}_{0.25}\text{Cu}_{0.2}\text{Zn}_{0.55})\text{Sm}_x\text{Fe}_{2-x}\text{O}_4$  ferrites with different Sm-content.

Fig. 4.41 shows the magnetic hysteresis loop of different  $(\text{Ni}_{0.25}\text{Cu}_{0.2}\text{Zn}_{0.55})\text{Sm}_x\text{Fe}_{2-x}\text{O}_4$  ferrites. Saturation magnetization ( $M_s$ ) values of different compositions are given in Table 4.10. The saturation magnetization of substituted ferrites was higher than un-substituted specimen, might be due to better density and higher permeability of the substituted ferrites. The  $M_s$  of  $x = 0.075$  specimen was lower than that of  $x = 0.05$  specimen. This was due to the presence of higher quantity of nonmagnetic  $\text{SmFeO}_3$  phase in  $x = 0.075$  composition or due to its ( $x = 0.075$ ) lower permeability as stated above.





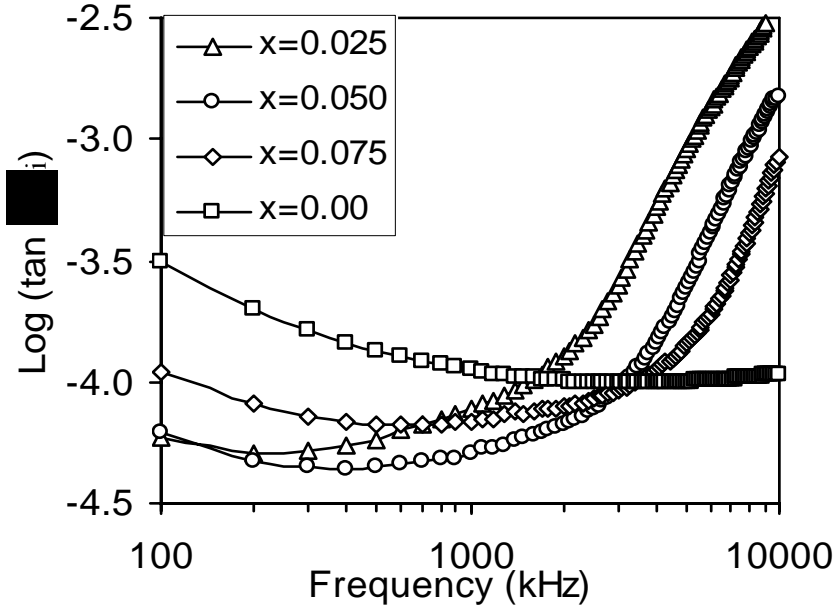
**Fig. 4.41.** Magnetic hysteresis loop for  $(\text{Ni}_{0.25}\text{Cu}_{0.2}\text{Zn}_{0.55})\text{Sm}_x\text{Fe}_{2-x}\text{O}_4$  ferrites with different Sm-content measured at room temperature.

Fig. 4.42 shows the relative loss factor (RLF) i.e. the ratio of the magnetic loss tangent to the initial permeability. RLF (up to a frequency around 2 MHz) of the ferrites decreased with Sm substitution. The higher RLF of un-substituted ferrite might be due to higher hysteresis loss of the specimen, which might arise from its porous (Table 4.9) structure. In general, hysteresis loss increases with increasing porosity [136]. All ferrites had higher RLF at lower frequency (kHz) range. The RLF decreased with increasing frequency which could be explained by equation (4.5). RLF of all specimens increased after about 2 MHz frequency due to magnetic relaxation losses.

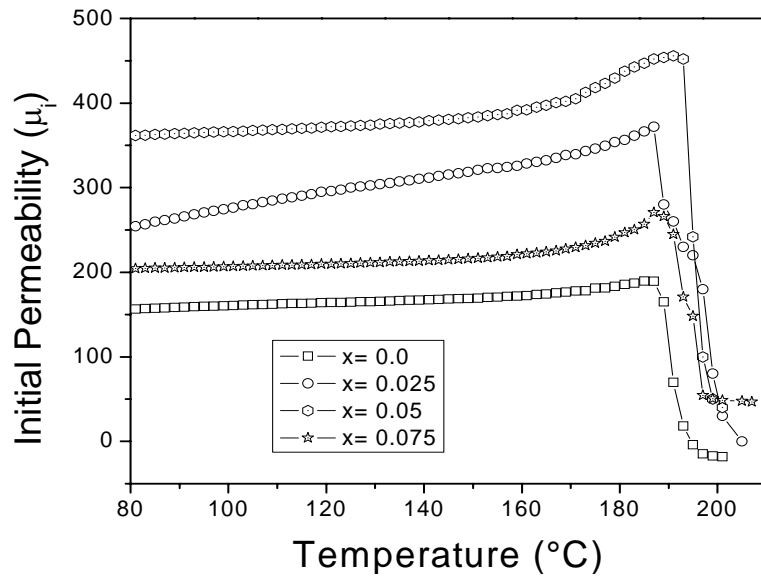
The change in Curie temperature of the ferrite with Sm substitution was also evaluated. Fig. 4.43 shows the temperature dependence of permeability in different compositions. No significant change in Curie temperature (Table 4.10) was found with Sm substitution. This again indicated that Sm had very low solubility in spinel ferrite.

Fig. 4.44 shows the frequency dependence of AC resistivity for different specimens. The resistivity increased with Sm substitution. The conduction in ferrite was considered to occur by the electron hopping between  $\text{Fe}^{2+}$  and  $\text{Fe}^{3+}$  ions that were located

at the octahedral site of the spinel ferrite structure. The specimen at  $x = 0.05$  showed highest resistivity among all, which might be attributed to the presence of lower amount of  $\text{Fe}^{2+}$  ions in the ferrites.



**Fig. 4.42.** Relative loss factor as a function of frequency in  $(\text{Ni}_{0.25}\text{Cu}_{0.2}\text{Zn}_{0.55})\text{Sm}_x\text{Fe}_{2-x}\text{O}_4$  ferrites with different Sm-content.



**Fig. 4.43.** Temperature dependency of permeability in  $(\text{Ni}_{0.25}\text{Cu}_{0.2}\text{Zn}_{0.55})\text{Sm}_x\text{Fe}_{2-x}\text{O}_4$  ferrites with different Sm-content.

As described earlier, Sm substituted compositions were deficient in Fe content and the crystallization of  $\text{SmFeO}_3$  at their grain boundaries impeded the oxidation of  $\text{Fe}^{+3}$  ions inside the grains. Hence,  $\text{Fe}^{+2}$  ions were expected to be at minimum in Sm substituted ferrites. This might be a reason of increased resistivity in them. The resistivity of all the compositions decreased with the increasing frequency. The AC resistivity ( $\rho$ ) was calculated as per equation (3.21). The resistivity was primarily dependent on the frequency, which was inversely proportional. That was why resistivity decreased with the increase in frequency.

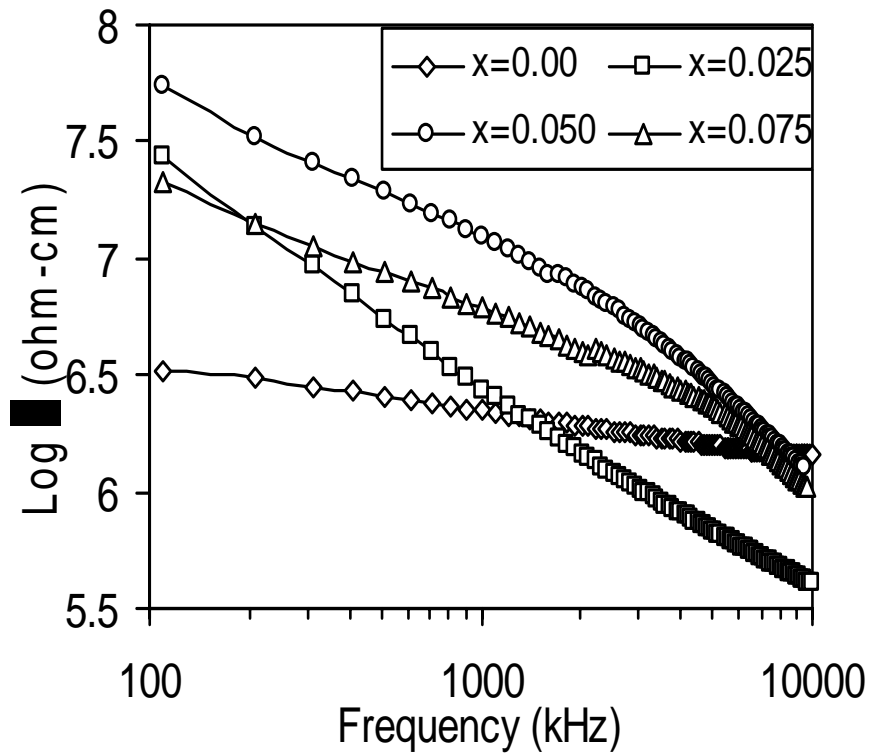


**Fig. 4.44.** AC Resistivity as a function of frequency in  $(\text{Ni}_{0.25}\text{Cu}_{0.2}\text{Zn}_{0.55})\text{Sm}_x\text{Fe}_{2-x}\text{O}_4$  ferrites with different Sm content.

#### 4.4.3 Summary

The substitution of Sm for Fe in  $(\text{Ni}_{0.25}\text{Cu}_{0.2}\text{Zn}_{0.55})\text{Sm}_x\text{Fe}_{2-x}\text{O}_4$  ferrites revealed mainly the formation of secondary phase of composition  $\text{SmFeO}_3$ . Bulk density and grain size of the ferrites increased with increasing Sm substitution. Increased densification

might be due to the appearance of excess Ni, Cu, and Zn compared to Fe in the composition.

A significant increase in initial permeability of the ferrite was found at small fraction at  $x = 0.05$  of Sm substitution. The increased permeability was due to better densification and increased grain size in substituted ferrites. The AC resistivities of substituted ferrites also increased due to the lowering of  $\text{Fe}^{+2}$  ion concentration. The composition  $(\text{Ni}_{0.25}\text{Cu}_{0.2}\text{Zn}_{0.55})\text{Sm}_{0.05}\text{Fe}_{1.95}\text{O}_4$  showed the best electromagnetic properties among all the specimens.

## 4.5 Effect of Bi<sub>2</sub>O<sub>3</sub>-V<sub>2</sub>O<sub>5</sub>-MoO<sub>3</sub> addition on structural, densification behaviors and electromagnetic properties of (Ni<sub>0.25</sub>Cu<sub>0.2</sub>Zn<sub>0.55</sub>)Fe<sub>2</sub>O<sub>4</sub> ferrite

### 4.5.1 Introduction

The use of sintering additives was found to be an effective method in practical manufacturing to lower the sintering temperature without degrading the electromagnetic properties [108] of the ferrites. Many researchers used Bi<sub>2</sub>O<sub>3</sub> [13, 109-111], V<sub>2</sub>O<sub>5</sub> [55, 99, 103], MoO<sub>3</sub> [20, 106], Glass [144], PbO [9] and WO<sub>3</sub> [110, 113] as sintering aids in NiCuZn ferrite. Among these V<sub>2</sub>O<sub>5</sub>, Bi<sub>2</sub>O<sub>3</sub>, and MoO<sub>3</sub> were the most effective sintering aids for NiCuZn ferrites [145].

These additives form liquid phases either due to the melting of the additives or due to the eutectic liquid phase formation between the additives and ferrite. Amount of liquid phase increases with increasing amount of sintering aids which results in increased densification. However, excessive amount of sintering additives will deteriorate electromagnetic properties of the ferrites. So, optimum content of sintering aids is necessary to achieve good sinterability as well as better electromagnetic properties.

*Hsu et al.* [99] stated that 0.5 mol% (~ 0.20 wt%) V<sub>2</sub>O<sub>5</sub> addition had better densification in NiCuZn ferrites. In *Jeong et al.* [109] study, 0.25 wt% Bi<sub>2</sub>O<sub>3</sub> addition showed optimum electromagnetic properties in the ferrite. *Seo et al.* [106] reported that 0.20 wt% MoO<sub>3</sub> addition had given highest bulk density and maximum initial permeability in the ferrite. In this study, the concentration of above three sintering additives were fixed at 0.20 wt% for V<sub>2</sub>O<sub>5</sub>, 0.25 wt% for Bi<sub>2</sub>O<sub>3</sub> and 0.20 wt% for MoO<sub>3</sub>, respectively as per above references. Table 4.11 shows the weight percent of different sintering additives used in densification study of (Ni<sub>0.25</sub>Cu<sub>0.2</sub>Zn<sub>0.55</sub>)Fe<sub>2</sub>O<sub>4</sub> ferrites. When 2 and 3 additives were used in the mixture, 1/2 and 1/3rd of the above concentration of each were added respectively.

The green samples containing different additives were sintered at temperatures in the range of 875°C to 950°C at 25°C interval with 4 hrs holding time. Effects of those

sintering additives on the densification behavior were investigated. Electrical resistivity and magnetic properties of sintered specimens were also measured.

**Table 4.11** Weight percent of different sintering additives used in  $(\text{Ni}_{0.25}\text{Cu}_{0.2}\text{Zn}_{0.55})\text{Fe}_2\text{O}_4$  ferrite.

Composition	Sintering aids & their contents (wt %)		
	$\text{V}_2\text{O}_5$	$\text{Bi}_2\text{O}_3$	$\text{MoO}_3$
$\text{V}_2\text{O}_5$	0.20	Nil	Nil
$\text{Bi}_2\text{O}_3$	Nil	0.25	Nil
$\text{MoO}_3$	Nil	Nil	0.20
$\text{V}_2\text{O}_5 + \text{Bi}_2\text{O}_3$	0.10	0.125	Nil
$\text{V}_2\text{O}_5 + \text{MoO}_3$	0.10	Nil	0.10
$\text{Bi}_2\text{O}_3 + \text{MoO}_3$	Nil	0.125	0.10
$\text{V}_2\text{O}_5 + \text{Bi}_2\text{O}_3 + \text{MoO}_3$	0.067	0.083	0.067

## 4.5.2 Results and Discussion

### 4.5.2.1 Phase Analysis

The phase purity of sintered specimens was studied by XRD. Fig. 4.45 shows the XRD patterns of sintered (900°C for 4 hrs) ferrite pellets containing different additives. No secondary phase was detected except spinel ferrite phases. The crystallite size was calculated from full width at half maximum of the [311] peak using Scherer formula.

Table 4.12 shows the crystallite size of ferrites with different additives and sintered at different temperatures. The crystallite size increased with increasing sintering temperature.  $\text{V}_2\text{O}_5$  added ferrite had shown the highest crystallite size compared to the other additives which might be due to its lowest melting temperature among all that encouraged the formation of higher amount of liquid phase in the system [99] and hence greater crystallization.

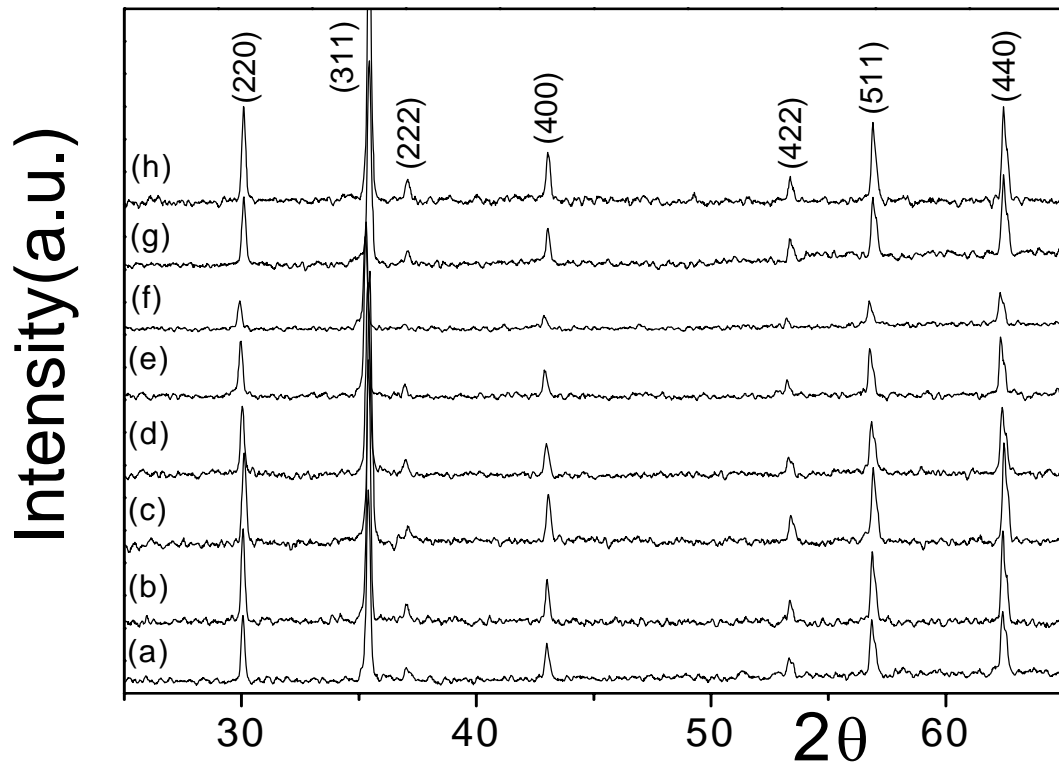


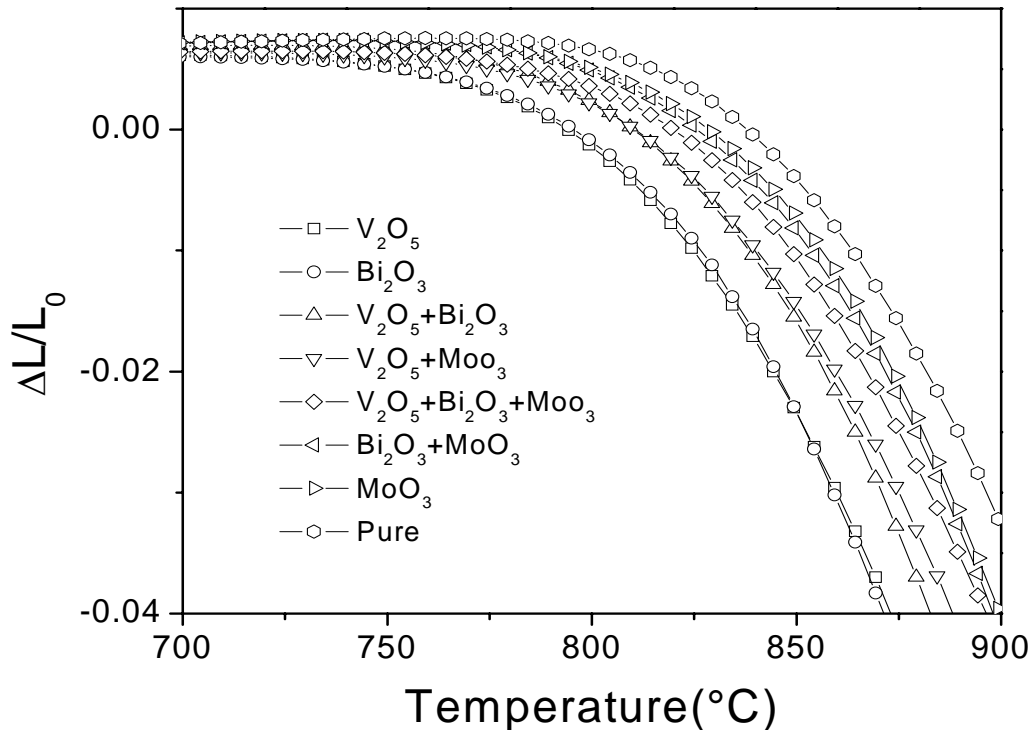
**Fig. 4.45.** XRD patterns of the a) sintered  $(\text{Ni}_{0.25}\text{Cu}_{0.2}\text{Zn}_{0.55})\text{Fe}_2\text{O}_4$  ferrite and that added with sintering additives like b)  $\text{V}_2\text{O}_5$ , c)  $\text{Bi}_2\text{O}_3$ , d)  $\text{MoO}_3$ , e)  $\text{V}_2\text{O}_5$  plus  $\text{Bi}_2\text{O}_3$ , f)  $\text{V}_2\text{O}_5$  plus  $\text{MoO}_3$ , g)  $\text{Bi}_2\text{O}_3$  plus  $\text{MoO}_3$  and h)  $\text{V}_2\text{O}_5$  plus  $\text{Bi}_2\text{O}_3$  plus  $\text{MoO}_3$ .

**Table 4.12** Crystallite size of pure and different sintering additives modified  $(\text{Ni}_{0.25}\text{Cu}_{0.2}\text{Zn}_{0.55})\text{Fe}_2\text{O}_4$  ferrite sintered at different temperatures.

Composition	Crystallite size (nm) at different sintering temperature			
	875°C	900°C	925°C	950°C
Pure	53	55	58	60
$\text{V}_2\text{O}_5$	76	98	104	114
$\text{Bi}_2\text{O}_3$	67	92	95	98
$\text{MoO}_3$	55	58	65	68
$\text{V}_2\text{O}_5 + \text{Bi}_2\text{O}_3$	62	80	89	91
$\text{V}_2\text{O}_5 + \text{MoO}_3$	60	76	82	87
$\text{Bi}_2\text{O}_3 + \text{MoO}_3$	56	65	70	71
$\text{V}_2\text{O}_5 + \text{Bi}_2\text{O}_3 + \text{MoO}_3$	58	71	72	77

#### 4.5.2.2 Densification and Microstructure

Fig. 4.46 shows the shrinkage curves of ferrite specimens in presence of different sintering aids. The slope of the shrinkage curve increased with sintering aids compared to that of undoped ferrite specimen. This indicated that the rate of densification increased with different sintering additives. Onset temperature of shrinkage can be a parameter for evaluating the efficiency of sintering aids. Onset temperatures of different specimens were derived from the Fig. 4.46 and shown in Table 4.13. The onsets were lowered with the addition of sintering aids and it was found to be lowest for  $V_2O_5$  added ferrites. This indicated that  $V_2O_5$  might help in forming higher amount of liquid phase compared to other sintering aids in the system.



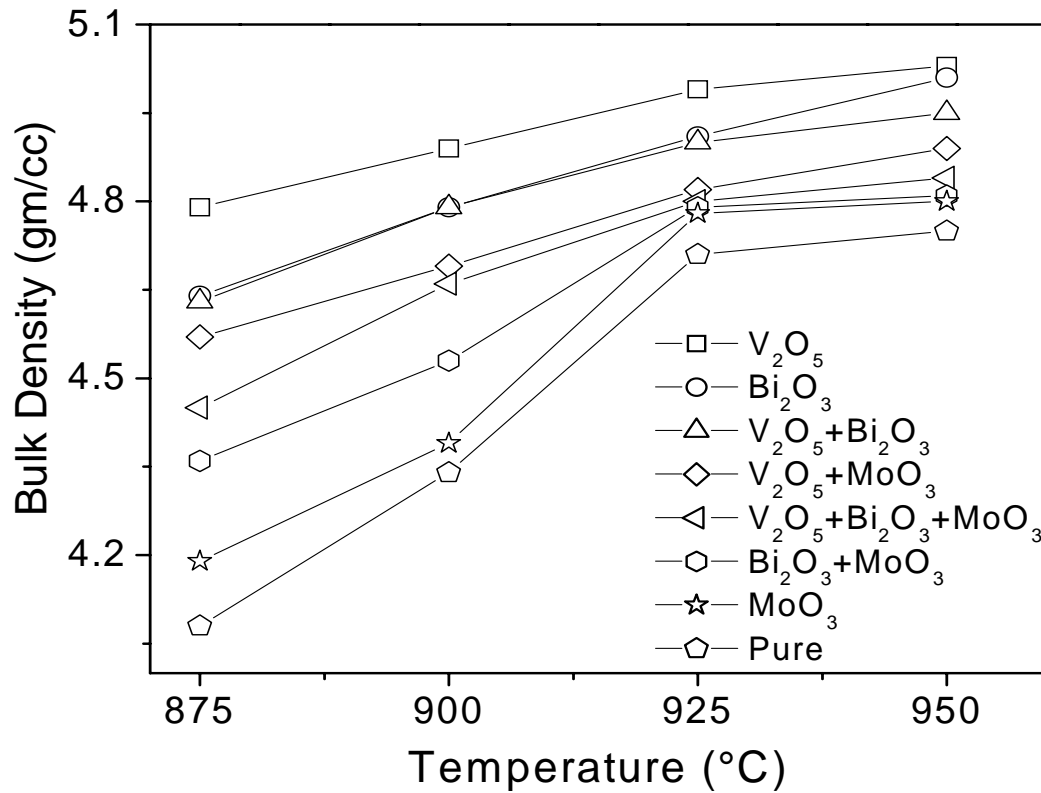
**Fig. 4.46.** Shrinkage curves for  $(Ni_{0.25}Cu_{0.2}Zn_{0.55})Fe_2O_4$  ferrites those modified with different additives. Shrinkage was measured at a heating rate of  $5^\circ C/min$  in air.

Fig. 4.47 shows the variation of sintered densities with sintering temperatures of the ferrite those containing different sintering additives. Fig. 4.48 shows the variation of open porosities with sintering temperatures of the ferrite those containing different sintering additives.



**Table 4.13** Onset temperature of shrinkage curve of  $(\text{Ni}_{0.25}\text{Cu}_{0.2}\text{Zn}_{0.55})\text{Fe}_2\text{O}_4$  ferrite with different sintering additives.

Composition	On-Set Temperature (°C)
Pure	868
$\text{V}_2\text{O}_5$	825
$\text{Bi}_2\text{O}_3$	838
$\text{MoO}_3$	867
$\text{V}_2\text{O}_5 + \text{Bi}_2\text{O}_3$	858
$\text{V}_2\text{O}_5 + \text{MoO}_3$	862
$\text{Bi}_2\text{O}_3 + \text{MoO}_3$	867
$\text{V}_2\text{O}_5 + \text{Bi}_2\text{O}_3 + \text{MoO}_3$	866



**Fig. 4.47.** Bulk densities of the sintered  $(\text{Ni}_{0.25}\text{Cu}_{0.2}\text{Zn}_{0.55})\text{Fe}_2\text{O}_4$  ferrites with different additives and sintered at different temperatures.

The bulk density increased and porosity decreased with sintering aids compared to undoped one. This indicated an improved densification by the addition of sintering aids. The enhanced densification of the ferrite was attributed to the liquid phase assisted densification through particle re-arrangement and solution re-precipitation [144]. Liquid phase formation in these systems was either due to the melting of the sintering additives or due to the lowering of eutectic temperatures in presence of additives [144].

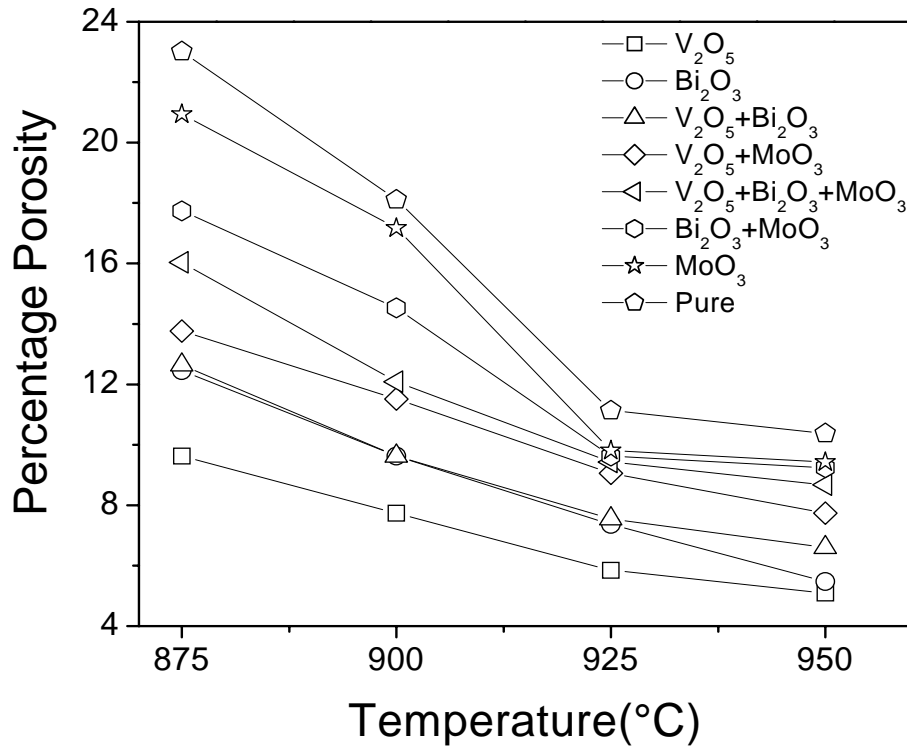


**Fig. 4.48.** Variation of porosity with sintering temperature of  $(\text{Ni}_{0.25}\text{Cu}_{0.2}\text{Zn}_{0.55})\text{Fe}_2\text{O}_4$  ferrites having different additives.

All sintering aids promoted the densification of the ferrite. This is mainly due to the formation of interfacial liquid by the additives which enhanced the mass transport kinetics between the ferrite grains [9]. In case of single additive,  $\text{V}_2\text{O}_5$  had shown better densification than  $\text{Bi}_2\text{O}_3$  and  $\text{MoO}_3$ , respectively. It was due to lower melting temperature of  $\text{V}_2\text{O}_5$  ( $690^\circ\text{C}$ ) [99] compared to that of  $\text{Bi}_2\text{O}_3$  ( $\sim 817^\circ\text{C}$ ) and  $\text{MoO}_3$  ( $800^\circ\text{C}$ ) [106].  $\text{Bi}_2\text{O}_3$  showed higher densification behavior than  $\text{MoO}_3$ , although  $\text{Bi}_2\text{O}_3$  had higher melting temperature compared to  $\text{MoO}_3$ . The phenomena also reflected in the

shrinkage study with lower onset temperature for  $\text{Bi}_2\text{O}_3$ . It might be due to the greater lowering of eutectic temperature by  $\text{Bi}_2\text{O}_3$  than  $\text{MoO}_3$  in the ferrite matrix.

The binary mixed additives could also promote densification of NiCuZn ferrites [110, 105]. The bulk density in case of ' $\text{V}_2\text{O}_5$  plus  $\text{Bi}_2\text{O}_3$ ' mixed additive was almost same to that for  $\text{Bi}_2\text{O}_3$  additive. 2<sup>nd</sup> and 3<sup>rd</sup> highest densification was found in ' $\text{V}_2\text{O}_5$  plus  $\text{MoO}_3$ ' and ' $\text{Bi}_2\text{O}_3$  plus  $\text{MoO}_3$ ' respectively. All  $\text{MoO}_3$  containing binary additive systems showed lower densification behavior, which might be due to higher onset temperature of  $\text{MoO}_3$  component. In case of ternary mixed additives i.e. ' $\text{V}_2\text{O}_5$  plus  $\text{Bi}_2\text{O}_3$  plus  $\text{MoO}_3$ ', densification was lower than ' $\text{V}_2\text{O}_5$  plus  $\text{MoO}_3$ ' and higher than ' $\text{Bi}_2\text{O}_3$  plus  $\text{MoO}_3$ '. So, this indicated that the densification behavior of binary ' $\text{Bi}_2\text{O}_3$  plus  $\text{MoO}_3$ ' mixed additives could be improved by adding  $\text{V}_2\text{O}_5$  as third component. As expected, densities of the sintered ferrites increased with increasing sintering temperature.

Fig. 4.49 to Fig. 4.50 shows the microstructure of sintered specimens that were sintered at  $900^\circ\text{C}$  for 4 hrs. It was evidenced from SEM analysis that abnormal grain growth occurred in the presence of additives. A rapid grain growth of a limited number of grains to size much larger than those of the average grain population was observed. It might be due to the presence of different particle size in the powder. Large particles in the initial powder mix act as seeds for rapid grain growth because the solubility of large particles is low and that of small particles is high [146].

#### **4.5.2.3 Electromagnetic Properties**

Fig. 4.51 shows initial permeability at 100 kHz of ferrites sintered at various temperatures and treated with various additives. As expected, the initial permeability increased with temperature for all cases.  $\text{V}_2\text{O}_5$  added specimen had the highest initial permeability and as usual undoped specimen had the lowest. The initial permeability decreased with the following sequence of sintering additives modified specimens;

$\text{Bi}_2\text{O}_3 \rightarrow \text{'V}_2\text{O}_5 \text{ plus Bi}_2\text{O}_3\text{'}$   $\rightarrow \text{'V}_2\text{O}_5 \text{ plus MoO}_3\text{'}$   $\rightarrow \text{'V}_2\text{O}_5 \text{ plus Bi}_2\text{O}_3 \text{ plus MoO}_3\text{'}$   $\rightarrow \text{'Bi}_2\text{O}_3 \text{ plus MoO}_3\text{'}$   $\rightarrow \text{MoO}_3$ , respectively.

Comparing this data with sintered densities (Fig. 4.47) and grain size of microstructures (Fig. 4.49 and Fig. 4.50), it might be concluded that the increased permeability was closely correlated with the densification and grain size of the ferrites. It has been described that ferrites with higher density and larger average grain size possess higher initial permeability [134].

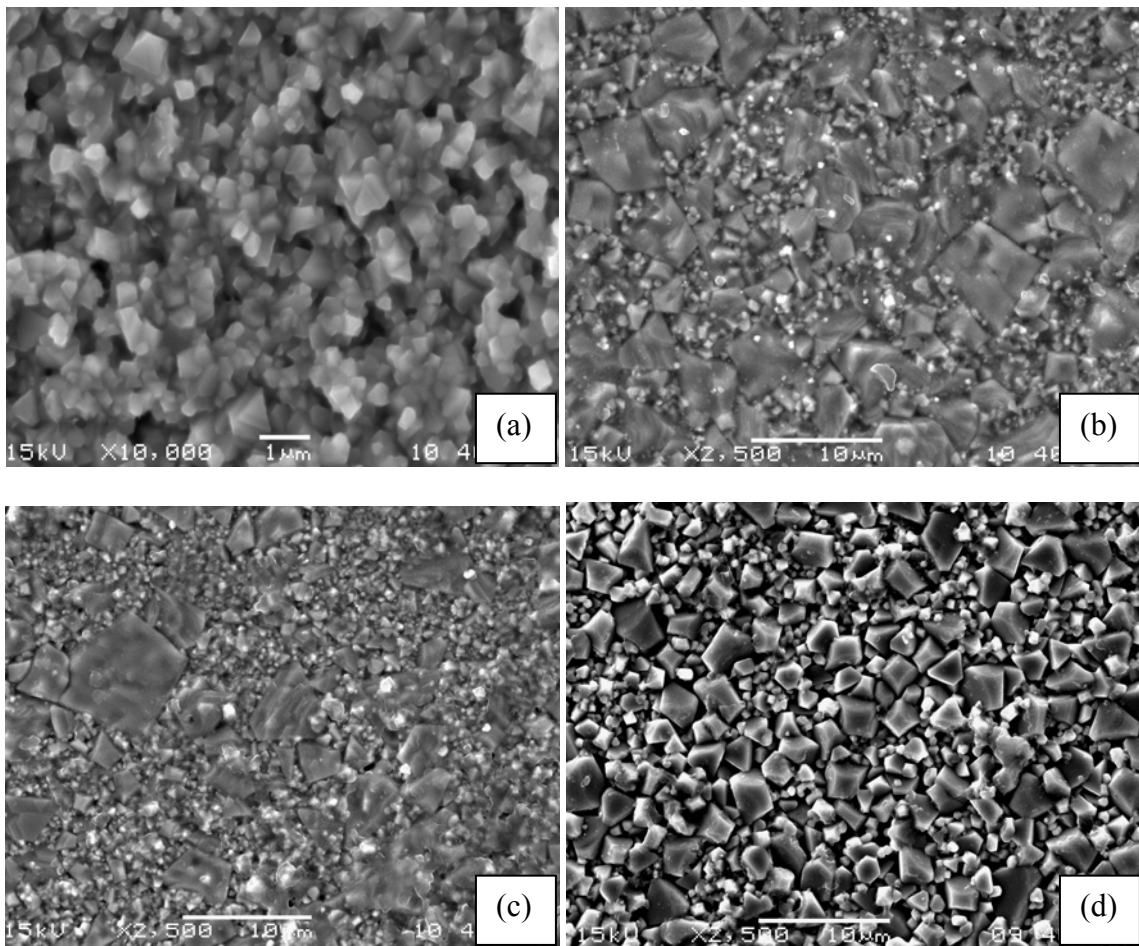


**Fig. 4.49.** SEM photographs of sintered  $(\text{Ni}_{0.25}\text{Cu}_{0.2}\text{Zn}_{0.55})\text{Fe}_2\text{O}_4$  ferrite a) undoped and doped with sintering additives like b)  $\text{V}_2\text{O}_5$ , c)  $\text{Bi}_2\text{O}_3$  and d)  $\text{MoO}_3$ .

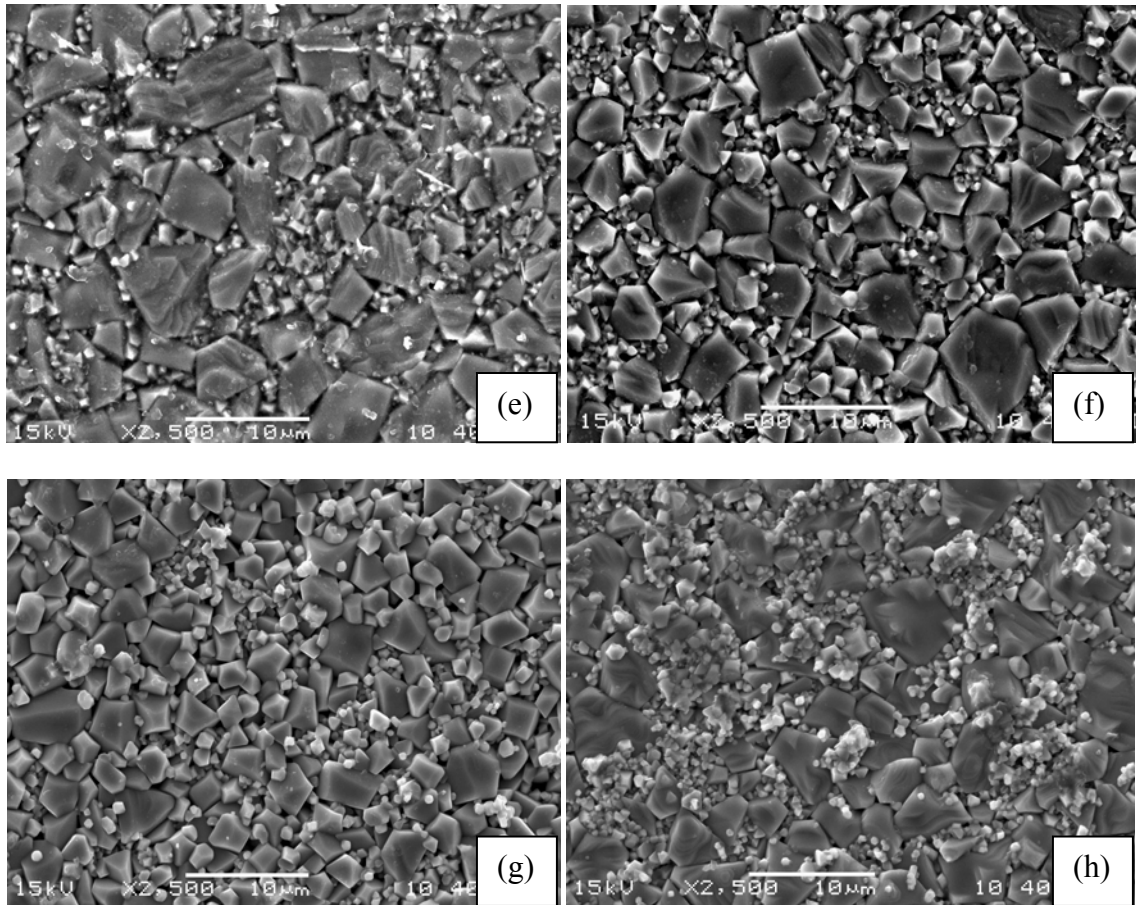
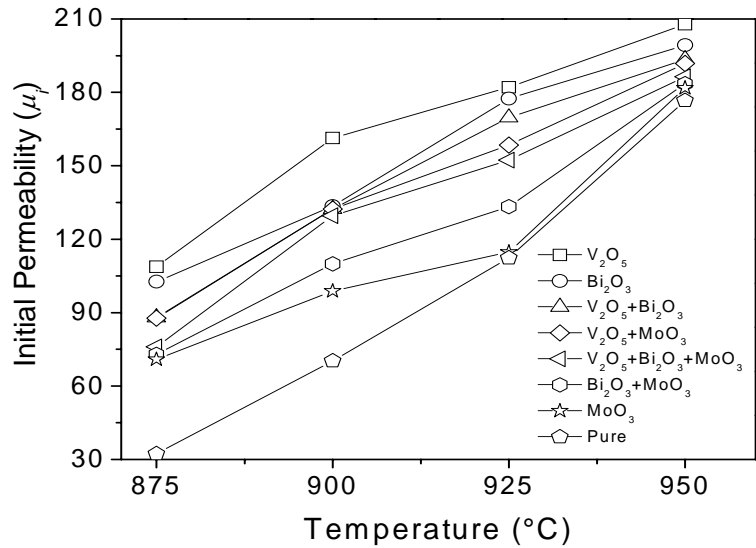


**Fig. 4.50.** SEM photographs of sintered  $(\text{Ni}_{0.25}\text{Cu}_{0.2}\text{Zn}_{0.55})\text{Fe}_2\text{O}_4$  ferrite doped with sintering additives like e)  $\text{V}_2\text{O}_5$  plus  $\text{Bi}_2\text{O}_3$ , f)  $\text{V}_2\text{O}_5$  plus  $\text{MoO}_3$ , g)  $\text{Bi}_2\text{O}_3$  plus  $\text{MoO}_3$  and h)  $\text{V}_2\text{O}_5$  plus  $\text{Bi}_2\text{O}_3$  plus  $\text{MoO}_3$ .

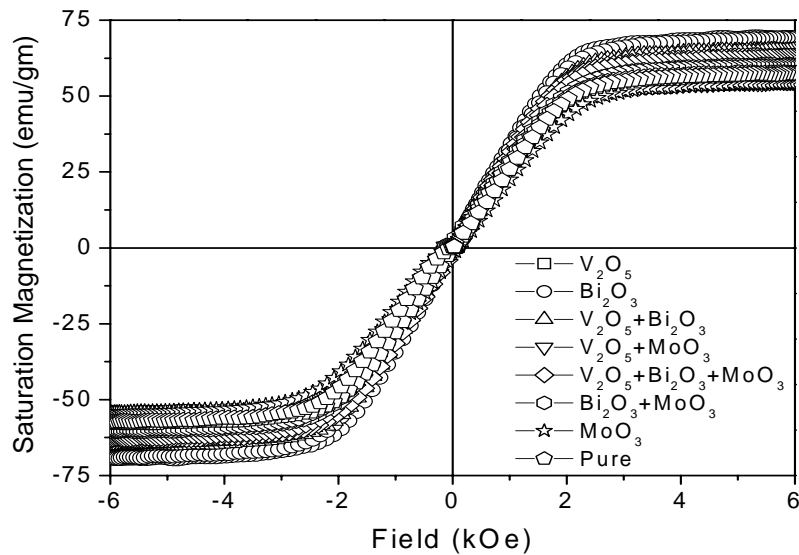
Fig. 4.52 shows the hysteresis loop of sintered  $(\text{Ni}_{0.25}\text{Cu}_{0.2}\text{Zn}_{0.55})\text{Fe}_2\text{O}_4$  ferrites sintered at  $950^\circ\text{C}$  with different additives. The saturation magnetization of additive modified ferrites was higher than un-doped specimen that might be due to higher density and therefore higher permeability of the modified ferrites.

Table 4.14 shows the resistivities of different additives modified  $(\text{Ni}_{0.25}\text{Cu}_{0.2}\text{Zn}_{0.55})\text{Fe}_2\text{O}_4$  ferrite those sintered at  $900^\circ\text{C}$  for 4 hrs. Resistivity is governed by grain boundary glassy phase. Undoped specimen showed highest resistivity due to the absence of glassy phase and  $\text{V}_2\text{O}_5$  added specimen showed the highest resistivity compared with other additives. Fig. 4.53 shows the frequency dependency of AC resistivity for different compositions sintered at  $950^\circ\text{C}$  for 4 hrs. The resistivity of all the

compositions decreases with the increase in frequency. The resistivity was primarily dependent on the frequency which is inversely proportional. That is why resistivity decreases with the increase in frequency. Fig. 4.54 shows the magnetic loss of the ferrite. The losses decreased with increasing frequency which could be explained by equation (4.5).



**Fig. 4.51.** Variation of permeability with sintering temperature of different additives modified  $(\text{Ni}_{0.25}\text{Cu}_{0.2}\text{Zn}_{0.55})\text{Fe}_2\text{O}_4$  ferrites.



**Fig. 4.52.** Magnetic hysteresis loop of  $(\text{Ni}_{0.25}\text{Cu}_{0.2}\text{Zn}_{0.55})\text{Fe}_2\text{O}_4$  ferrite sintered at 950°C with different additives.

**Table 4.14** Resistivities of  $(\text{Ni}_{0.25}\text{Cu}_{0.2}\text{Zn}_{0.55})\text{Fe}_2\text{O}_4$  ferrite with sintering temperature  $900^\circ\text{C}$  for different additives modified specimens.

Composition	Resistivity ( $\times 10^6 \text{ohm-cm}$ ) at $900^\circ\text{C}$
Pure	0.47
$\text{V}_2\text{O}_5$	0.97
$\text{Bi}_2\text{O}_3$	0.07
$\text{MoO}_3$	0.36
$\text{V}_2\text{O}_5 + \text{Bi}_2\text{O}_3$	0.11
$\text{V}_2\text{O}_5 + \text{MoO}_3$	0.11
$\text{Bi}_2\text{O}_3 + \text{MoO}_3$	0.24
$\text{V}_2\text{O}_5 + \text{Bi}_2\text{O}_3 + \text{MoO}_3$	0.13

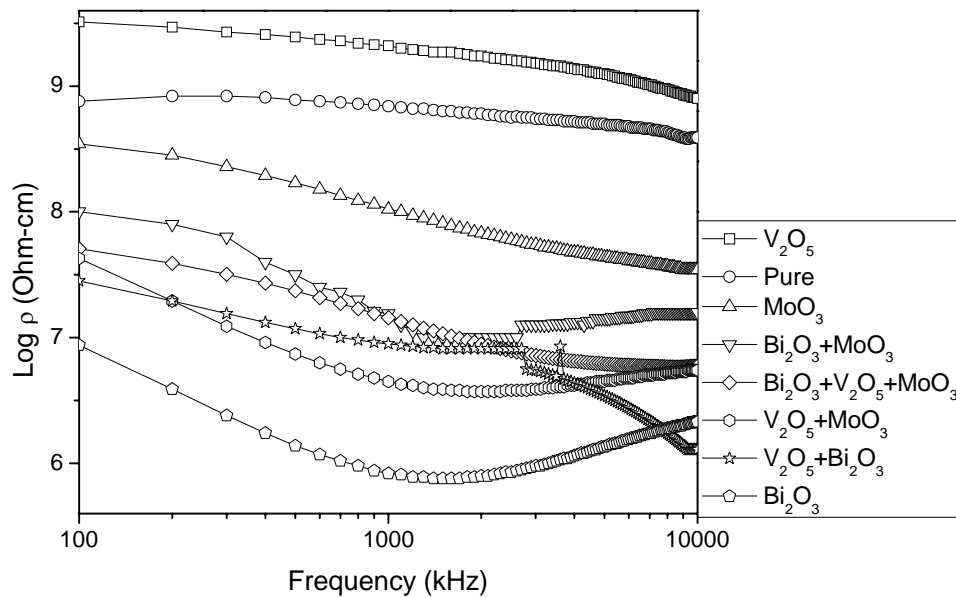


**Fig. 4.53.** AC resistivity as a function of frequency in  $(\text{Ni}_{0.25}\text{Cu}_{0.20}\text{Zn}_{0.55})\text{Fe}_2\text{O}_4$  ferrite (Sintered at  $950^\circ\text{C}$  for 4 hrs) with different additives.

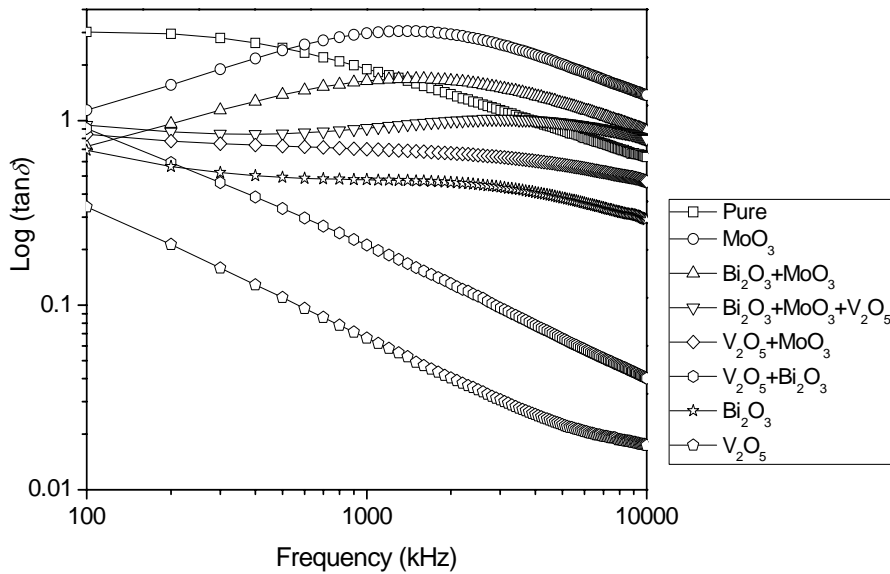


**Fig. 4.54.** Magnetic loss as a function of frequency in  $(\text{Ni}_{0.25}\text{Cu}_{0.20}\text{Zn}_{0.55})\text{Fe}_2\text{O}_4$  ferrite (Sintered at  $950^\circ\text{C}$  for 4 hrs) with different additives.

### 4.5.3 Summary

Effect of sintering additives on densification behaviors and electromagnetic properties of NiCuZn ferrites were studied. The results showed that small amount of additives was able to enhance the densification.  $\text{V}_2\text{O}_5$  sintering aid exhibited better densification behavior among all sintering aids with an onset sintering temperature of  $825^\circ\text{C}$ . In binary systems ' $\text{V}_2\text{O}_5$  plus  $\text{Bi}_2\text{O}_3$ ' showed better densification. Better densification had also resulted improved electromagnetic properties of the  $\text{V}_2\text{O}_5$  modified ferrites.



# *Chapter V*

## *Conclusions and Future Work*

## 5.1 Conclusions

The present work was focused on the effect of different substitutions and sintering aids on electromagnetic properties of NiCuZn ferrites.  $(\text{Ni}_{0.8-x}\text{Cu}_{0.2}\text{Zn}_x)\text{Fe}_2\text{O}_4$  ferrites with  $0.45 \leq x \leq 0.6$  compositions were studied to optimize Zn concentration. The effects of  $\text{Mg}^{2+}$  substitution for  $\text{Ni}^{2+}$  and  $\text{La}^{3+}$ ,  $\text{Sm}^{3+}$  substitutions for  $\text{Fe}^{3+}$  on the electromagnetic properties of the ferrites were investigated. The effects of sintering aids  $\text{V}_2\text{O}_5$ ,  $\text{Bi}_2\text{O}_3$  and  $\text{MoO}_3$  on the densification kinetics and electromagnetic properties of the ferrites were also investigated.

The significant findings of this work are as follows:

- 1) Nano crystalline NiCuZn ferrite powder was successfully synthesized by the ignition of gel precursor upon heating at  $200^\circ\text{C}$ .
- 2) Auto combustion process resulted in the formation of nano-sized (19-22 nm), highly reactive (specific surface area-  $40\text{-}50 \text{ m}^2/\text{gm}$ ) and crystalline spinel ferrite. The ferrite powders showed good sinterability at around  $<950^\circ\text{C}$ .
- 3)  $(\text{Ni}_{0.25}\text{Cu}_{0.2}\text{Zn}_{0.55})\text{Fe}_2\text{O}_4$  composition was optimized based on good permeability as well as resistivity. The composition showed an initial permeability of about 111 and the resistivity of about  $8.9 \text{ M}\Omega\text{-cm}$  at 100 kHz with frequency stability up to 10 MHz.
- 4) The bulk density and grain size were increased with increasing Mg substitution for Ni in the ferrite.  $(\text{Ni}_{0.07}\text{Mg}_{0.18}\text{Cu}_{0.2}\text{Zn}_{0.55})\text{Fe}_2\text{O}_4$  composition showed highest permeability, good AC resistivity and lowest relative loss factor. Increased permeability might be attributed to the decrease in magnetostriction constant with Mg addition.
- 5) The La substitution for Fe in the ferrite mainly produced secondary phase  $\text{LaFeO}_3$ . Bulk density and grain size of the ferrite were increased with increasing La substitution. The composition  $(\text{Ni}_{0.25}\text{Cu}_{0.2}\text{Zn}_{0.55})\text{La}_{0.025}\text{Fe}_{1.975}\text{O}_4$  showed best electromagnetic properties. Increased initial permeability might be due to

compressive stress present in the sintered samples. The La solubility in the ferrite lattice was found to be very low ( $\sim 0.1$  atom/unit cell). The AC resistivity of the composition was also increased, which might be due to the lowering of  $\text{Fe}^{2+}$  ion concentration.

- 6) Sm substitution for Fe also produced secondary phase  $\text{SmFeO}_3$  in the ferrite. Bulk density and grain size of the ferrites were increased with increasing Sm substitution. A significant increase in initial permeability was found at small fraction of Sm substitution at  $x = 0.05$ . The nominal composition  $(\text{Ni}_{0.25}\text{Cu}_{0.2}\text{Zn}_{0.55})\text{Sm}_{0.05}\text{Fe}_{1.95}\text{O}_4$  showed the best electromagnetic properties with an increase in initial permeability that might be due to compressive stress present in sintered specimens.
- 7)  $\text{V}_2\text{O}_5$ ,  $\text{Bi}_2\text{O}_3$  and  $\text{MoO}_3$  sintering additives were investigated for their behavior on  $(\text{Ni}_{0.25}\text{Cu}_{0.2}\text{Zn}_{0.55})\text{Fe}_2\text{O}_4$  ferrite densification.  $\text{V}_2\text{O}_5$  exhibited better densification behavior among all sintering aids with an onset sintering temperature of  $\approx 825^\circ\text{C}$ . Better densification has also resulted improved electromagnetic properties of the  $\text{V}_2\text{O}_5$  added ferrites.

## 5.2 Scope for Future Work

With the advent of nano technology, a tremendous surge in research on miniaturization and high efficiency electronic devices is on rise. These modern devices exclusively need soft magnetic materials as its basic magnetic component. Soft ferrite materials are extensively used in inductors which form a basic requirement in high technology areas. NiCuZn ferrites adequately suit these demands and are considered to shape the future of advanced technology.

The scopes of the future works are proposed as:

- a) The structural origin of the phenomena; enhanced electromagnetic properties in  $(\text{Ni}_{0.07}\text{Mg}_{0.18}\text{Cu}_{0.2}\text{Zn}_{0.55})\text{Fe}_2\text{O}_4$  ferrite, will be investigated through Rietveld analysis.

- b) To investigate the effects of La substitution for Fe on the electromagnetic properties of  $(\text{Ni}_{0.07}\text{Mg}_{0.18}\text{Cu}_{0.2}\text{Zn}_{0.55})\text{Fe}_2\text{O}_4$  ferrite and its fundamental aspect.
- c) To investigate the effect of sintering aids on the properties of  $(\text{Ni}_{0.07}\text{Mg}_{0.18}\text{Cu}_{0.2}\text{Zn}_{0.55})\text{Fe}_2\text{O}_4$ ,  $(\text{Ni}_{0.25}\text{Cu}_{0.2}\text{Zn}_{0.55})\text{La}_{0.025}\text{Fe}_{1.975}\text{O}_4$  and  $(\text{Ni}_{0.25}\text{Cu}_{0.2}\text{Zn}_{0.55})\text{Sm}_{0.05}\text{Fe}_{1.95}\text{O}_4$  ferrites.
- d) To investigate the mechanism of sintering for different sintering aids.
- e) Fabrication and characterizations of multilayer chip inductor using improved NiCuZn ferrites as stated.

## REFERENCES

---

1. A. Goldman, "Recent Advances in Ferrite Materials Technology," in *Modern Ferrite Technology*, Van Nostrand Reinhold, New York, (1990).
2. T. Krishnaveni, B. R. Kanth, V. S. R. Raju, S. R. Murthy, *J. All. Compd.* 414 (1-2) (2006) 282.
3. R. J. Charles, A. R. Achuta, U. S. Patent No. 4966625 (1990).
4. N. Taguchi, T. Yamaguchi, Y. Okino, H. Kishi, *Proceedings of the 8th International Conference on Ferrites*, Kyoto, Japan (2000) 1122.
5. J. H. Nam, H. H. Jung, J. Y. Shin, J. H. Oh, *IEEE Trans. Magn.* 31 (6) (1995) 3985.
6. L. Mingyue, *Proceedings of the 8th International Conference on Ferrites*, Kyoto, Japan (2000) 1151.
7. T. Nakamura, *J. Magn. Magn. Mater.* 168 (1997) 285.
8. H. I. Hsiang, W. C. Liao, Y. J. Wang, Y. F. Cheng, *J. Magn. Magn. Mater.* 24 (7) (2004) 2015.
9. J. H. Jean, C. H. Lee, W. S. Kou, *J. Am. Ceram. Soc.* 82 (2) (1999) 343.
10. J. Z. Msomi, T. Moyo, T. B. Doyle, *J. Magn. Magn. Mater.* 310 (2007) 2534.
11. D. Stoppels, *J. Magn. Magn. Mater.* 160 (1996) 323.
12. O. F. Caltun, L. Spinu, Al. Stancu, L. D. Thung, W. Zhou, *J. Magn. Magn. Mater.* 242–245 (2002) 160.
13. J. Y. Hsu, W. S. Ko, H. D. Hen, C. J. Chen, *IEEE Trans. Mag.* 30 (6) (1994) 4875.
14. J. Y. Hsu, H. C. Lin, H. D. Shen, C. J. Chen, *IEEE Trans. Mag.* 33 (5) (1997) 3325.
15. C. Miao, J. Zhou, X. Cui, X. Wang, Z. Yue, L. Li, *Mat. Sci. Engg. B* 127 (2006) 1.
16. M. Yan, J. Hu, *J. Magn. Magn. Mater.* 305 (1) (2006) 171.
17. M. Fujimoto, *J. Am. Ceram. Soc.* 77 (11) (1994) 2873.
18. A. Barba, C. Clausell, C. Feliu, M. Monzo, *J. Am. Ceram. Soc.* 87 (4) (2004) 571.
19. H. M. Sung, C. J. Chen, W. S. Ko, H. C. Lin, *IEEE Trans. Magn.* 30 (6) (1994) 4906.
20. H. Su, H. Zhang, X. Tang, X. Xiang, *J. Magn. Magn. Mater.* 283 (2004) 157.
21. N. R. Reddy, M. V. Ramanaa, G. Rajithaa, E. Rajagopala, K.V. Sivakumara, V. R. K. Murthy, *J. Magn. Magn. Mater.* 292 (2005) 159.

22. G. Goev, V. Masheva, L. Ilkov, D. Nihtianova, M. Mikhov, Proceedings of the fifth General Conference of the Balkan Physical Union BPU-5 (2003) 687.
23. M. Paulus, Ceramics Materials Science Research, VOL II, Edited by H. Palmour, R.F. Davis and T.M. Hare, Plenum Press, New York (1978) 7.
24. K. C. Patil, S. S. Manoharan, D. Gajpathy, "Preparation of high density ferrites," in Handbook of Ceramics and Composites, vol. 1, New York: Marcel Decker (1990) 469.
25. W. C. Hsu, S. C. Chena, P. C. Kuo, C. T. Lie, W. S. Tsai, Mat. Sci. Engg. B 111 (2004) 142.
26. I. Z. Rahman, T. T. Ahmed, J. Magn. Magn. Mater. 290–291 (2005) 1576.
27. S. Modak, M. Ammar, F. Mazaleyrat, S. Das, P. K. Chakrabarti, J. All. Compd. 473 (1-2) (2009) 15.
28. S. A. Ghodake, U. R. Ghodake, S. R. Sawant, S. S. Suryavanshi, J. Magn. Magn. Mater. 305 (1) (2006) 110.
29. S. Zahi, M. Hashim, A. R. Daud, Mat. Lett. 60 (2006) 2803.
30. S. Yan, J. Geng, L. Yin, E. Zhou, J. Magn. Magn. Mater. 277 (1-2) (2004) 84.
31. J. H. Nam, S. J. Park, W. K. Kim, IEEE Trans. Magn. 39 (5) (2003) 3139.
32. Z. Yue, J. Zhou, L. Li, H. Zhang, Z. Gui, J. Magn. Magn. Mater. 208 (2000) 55.
33. Z. Yue, L. Li, J. Zhou, H. Zhang, Z. Gui, Mat. Sci. Engg. B 64 (1999) 68.
34. Z. Yue, L. Li, J. Zhou, H. Zhang, Z. Gui, J. Magn. Magn. Mater. 233 (2001) 224.
35. K. O. Low, F. R. Sale, J. Magn. Magn. Mater. 246 (2002) 30.
36. J. G. Koh, J. Kore. Phys. Soc. 44 (6) (2004) 1504.
37. Z. Yue, J. Zhou, L. Li, X. Wang, Z. Gui, Mat. Sci. Engg. B 86 (2001) 64.
38. E. Rezlescu, N. Rezlescu, P. D. Popa, J. Magn. Magn. Mater. 290–291 (2005) 1001.
39. R. V. Mangalaraja, S. Ananthakumar, P. Manohar, F. D. Gnanam, Mat. Sci. Engg. A 355 (2003) 320.
40. A. C. F. M. Costa, E. Tortella, M. R. Morelli, R. H. G. A. Kiminami, J. Magn. Magn. Mater. 256 (2003) 174.
41. C. C. Hwang, J. S. Tsai, T. H. Huang, Mat. Chem. Phys. 93 (2005) 330.
42. N. Das, D. Bhattacharya, A. Sen, H. S. Maiti, Cera. Intern. 35 (2009) 21.
43. J. Smit, H. P. J. Wijn, Ferrites, John Wiley & Sons, New York (1959).

44. K.O. Low, F. R. Sale, *J. Magn. Magn. Mater.* 256 (2003) 221.
45. M. A. Ahmed, E. Ateia, L. M. Salah, A. A. E. Gamal, *Mat. Chem. Phys.* 92 (2005) 310.
46. G. L. Sun, J. B. Li, J. J. Sun, X. Z. Yang, *J. Magn. Magn. Mater.* 281 (2004) 173.
47. M. Ajmal, A. Maqsood, *J. All. Compd.* 460 (2008) 54.
48. S. A. Jadhav, *Mat. Chem. Phys.* 65 (2000) 120.
49. A. M. Shaikh, C. M. Kanamadi, B. K. Chougule, *Mat. Chem. Phys.* 93 (2005) 548.
50. T. K. Gupta, R. L. Coble, *J. Am. Ceram. Soc.* 51 (1968) 521.
51. R. L. Coble, T. K. Gupta, G. C. Kuczynski, N. A. Hroton, C. F. Gibbon (Eds.), *Sintering and Related Phenomena*, Gordon and Breach, New York (1967) 423.
52. D. Hoeffgen, H. Hopper, I. Monch, *Ber Dt. Keram. Ges.* 55 (1978) 216.
53. J. J. Shrotri, S. D. Kulkarni, C. E. Deshpande, A. Mitra, S. R. Sainkar, P. S. Anil Kumar, S. K. Date, *Mat. Chem. Phys.* 59 (1999) 1.
54. O. F. Caltun et al. *IEEE Trans. Magn.* 37 (4) (2001) 2353.
55. M. Yan, J. Hu, W. Luo, W. Y. Zhang, *J. Magn. Magn. Mater.* 303 (1) (2006) 249.
56. M. C. Dimri, A. Verma, S. C. Kashyap, D. C. Dube, O. P. Thakur, C. Prakash, *Mat. Sci. Engg. B* 133 (2006) 42.
57. N. Rezlescu, E. Rezlescu, P. D. Popa, M. L. Craus, L. Rezlescu, *J. Magn. Magn. Mater.* 182 (1998) 199.
58. E. Rezlescu, N. Rezlescu, P. D. Popa, L. Rezlescu, C. Pasnicu, M. L. Craus, *Mat. Res. Bull.* 33 (6) (1998) 915.
59. S. M. Hoque, Md. A. Choudhury, Md. F. Islam, *J. Magn. Magn. Mater.* 251 (2002) 292.
60. M. M. Haque, M. Huq, M. A. Hakim, *Mat. Chem. Phys.* 112 (2008) 580.
61. D. Banerjee, D. Bahadur, K. G. Suresh, A. K. Nigam, *Physica B* 378–380 (2006) 1091.
62. Z. Yue, J. Zhou, Z. Gui, L. Li, *J. Magn. Magn. Mater.* 264 (2003) 258.
63. B. Li, Z. X. Yue, X. W. Qi, J. Zhou, Z. L. Gui, L. T. Li, *Mat. Sci. Engg. B* 99 (2003) 252.
64. N. Chu, X. Wang, Y. Liu, H. Jin, Q. Wu, L. Li, Z. Wang, H. Ge, *J. All. Compd.* 470 (1-2) (2009) 438.

65. X. W. Qi, J. Zhou, Z. Yue, Z. L. Gui, L. T. Li, *J. Magn. Magn. Mater.* 251 (2002) 316.
66. A. Bhaskar, B. R. Kanth, S. R. Murthy, *J. Magn. Magn. Mater.* 283 (2004) 109.
67. A. R. Bueno, M. L. Gregori, M. C. S. Nobrega, *Mat. Chem. Phys.* 105 (2007) 229.
68. A. B. V. Groenou, J. H. N. Creyghton, J. G. M. D. Lau, *J. Phys. Chem. Solids.* 35 (1974) 1081.
69. T. Y. Byun, S. C. Byeon, K. S. Hong, *IEEE Trans. Magn.* 35 (5) (1999) 3445.
70. J. Kulikowski, A. Bienkowski, *J. Magn. Magn. Mater.* 41 (1984) 63.
71. J. Xiang, X. Shen, X. Meng, *Mat. Chem. Phys.* 114 (1) (2009) 362.
72. E. Rezlescu, L. Sachelarie, P. D. Popa, N. Rezlescu, *IEEE Trans. Magn.* 36 (6) (2000) 3962.
73. M. Kaiser, *J. All. Compd.* 468 (1-2) (2009) 15.
74. Y. Zhong , L. Zhongwen , C. Shengming, S. Yuerning , S. Ke, *Rare Metals* 25 Spec. Issue (2006) 584.
75. A. M. E. Raj, T. Som, V. Ganesan, M. Jayachandran, G. Selvan, V. Swaminathan, C. Sanjeeviraja, *Nuclear Instruments and Methods in Physics Research B* 266 (2008) 2564.
76. V. A. M. Brabers, A. A. Hirsch, W. C. V. Vleuten, P. V. Doremalen, *IEEE Trans. Magn.* 14 (5) (1978) 895.
77. S. A. Mazen, A. E. A. E. Rahiem, B. A. Sabrah, *J. Mat. Sci.* 23 (1988) 2917.
78. D. M. Liu, *J. Mat. Sci.* 29 (1994) 1507.
79. A. Naknao, I. Nakahata, T. Murse, *J. Jpn. Soc. Powder Powder Metall.* 48 (2) (2001) 131.
80. M. Jain, S. B. Majumder, R. S. Katiyar, A. S. Bhalla, *Mat. Lett.* 57 (2003) 4232.
81. D. N. Bhosale, N. D. Choudhari, S. R. Sawant, P. P. Bakare, *J. Magn. Magn. Mater.* 173 (1997) 51.
82. D. N. Bhosale, S. R. Sawant, S. A. Gangal, R. R. Mahajan, P. P. Bakare, *Mat. Sci. Engg. B* 65 (1999) 79.
83. M. A. E. Hiti, *J. Magn. Magn. Mater.* 192 (1999) 305.
84. N. Rezlescu, E. Rezlescu, C. Pasnicu, M. L. Craus, *J. Phys. Condens. Matter* 6 (1994) 5707.



85. S. Solyman, *Cera. Intern.* 32 (2006) 755.
86. A. A. Sattar, K. M. El-Shokrofy, *J. Phys.* IV C1 (1997) 245.
87. M. A. Ahmed, N. Okasha, M. M. E. Sayed, *Cera. Intern.* 33 (1) (2007) 49.
88. N. Bogoroditzkll, V. V. Pasyukov, R. R. Basili, Y. M. Volokobinskll, *Sov. Phys. Doklady* 10 (1965) 85.
89. N. Rezlescu, E. Rezlescu, *Solid State Commun.* 88 (2) (1993)139.
90. S. E. Jacobo, S. Duhalde, H. R. Bertorello, *J. Magn. Magn. Mater.* 272–276 (2004) 2253.
91. L. Zhao, Y. Cui, H. Yang, L. Yu, W. Jin, S. Feng, *Mat. Lett.* 60 (2006) 104.
92. L. Zhao, H. Yang, X. Zhao, L. Yu, Y. Cui, S. Feng, *Mat. Lett.* 60 (2006) 1.
93. N. Rezlescu, E. Rezlescu, P. D. Popa, L. Rezlescu, *J. All. Compd.* 275-277 (1998) 657.
94. M. A. Ahmed, E. Ateia, F. M. Salem, *Physica B* (2008) (Accepted).
95. J. Sun, J. Li, G. Sun, *J. Magn. Magn. Mater.* 250 (2002) 20.
96. A. C. F. M. Costa, M. R. Morelli, R. H. G. A. Kiminami, *J. Mat. Sci.* 39 (2004) 1773.
97. A. A. Sattar, A. H. Wafik, K. M. E. Shokrofy, M. M. E. Tabby, *Phys. Stat. Sol. (a)* 171 (1999) 563.
98. M. H. Mahmoud, A. A. Sattar, *J. Magn. Magn. Mater.* 277 (2004) 101.
99. J. Y. Hsu, W. S. Ko, C. J. Chen, *IEEE Trans. Magn.* 31 (6) (1995) 3994.
100. P. J. V. Zagg, *J. Magn. Magn. Mater.* 315 (1999) 196.
101. T. Nakamura, *J. Magn. Magn. Mater.* 168 (1997) 265.
102. R. Lebourgeois, C. L. Fur, M. Labeyrie, M. Pate, J. P. Ganne, *J. Magn. Magn. Mater.* 160 (1996) 329.
103. R. Lebourgeois, S. Duguey, J. P. Ganne, J. M. Heintz, *J. Magn. Magn. Mater.* 312 (2007) 328.
104. O. Mirzaee, M. A. Golozar, A. Shafyei, *Mat. Charact.* 59 (2008) 638.
105. O. Mirzaee, A. Shafyei, M. A. Golozar, H. Shokrollahi, *J. All. Compds.* 461 (2008) 312.
106. S. E. Seo, J. H. Oh, *IEEE Trans. Magn.* 35 (5) (1999) 3412.
107. M. Gu, G. Liu, *J. All. Compds.* 475 (1-2) (2009) 356.
108. S. F. Wang, Y. R. Wang, T. C. K. Yang, C. F. Chen, C. A. Lu, C. Y. Huang, J.

- Magn. Magn. Mater. 220 (2000) 129.
109. J. Jeong, H.Y. Han, C.B. Moon, J. Mat. Sci. Mat. In Elect. 15 (5) (2004) 303.
  110. H. Su, H. Zhang, X. Tang, Mat. Sci. Engg. B 117 (2005) 231.
  111. K. Kawano, N. Sakurai, S. Kusumi, H. Kishi, J. Magn. Magn. Mater. 297 (2006) 26.
  112. L. B. Kong, Z. W. Li, G. Q. Lin, Y. B. Gan, Acta Materialia 55 (2007) 6561.
  113. K. S. Park, J. H. Nam, J. H. Oh, J. Magn. Magn. Mater. 226-230 (2001) 1415.
  114. H. Su, H. Zhang, X. Tang, Y. Shi, J. All. Compds. 468 (1-2) (2009) 290.
  115. Y. H. Wang, S. F. Wang, Int. J. Inorg. Mat. 3 (2001) 1189.
  116. M. D. Nersesyan, A. G. Peresada, A. G. Merzhanov, Int. J. SHS 7 (1998) 60.
  117. S. R. Jain, K. C. Adiga, Combustion and Flame 40 (1981) 71.
  118. B. D. Cullity, 'Elements of X-Ray Diffraction', 2nd Ed, Addison-Wesley. INC (1978).
  119. S. Upadhyay, O. Parkash, D. Kumar, J. All. Compd. 432 (2007) 258.
  120. H. M. Rietveld, J. Appl. Cryst. 2 (1969) 65.
  121. R. A. Young, Rietveld Method, International Union of Crystallography, Oxford University Press (1996).
  122. M. I. Rosales, M. P. Cuautle, V. M. Castano, J. Mat. Sci. 33 (1998) 3665.
  123. D. C. Jiles, D. L. Atherton, J. Magn. Magn. Mater. 61 (1-2) (1986) 48.
  124. J. F. Janak, J. Appl. Phys. 34 (4) (1963) 1119.
  125. D. Park, Phys. Rev. 97 (1) (1955) 60.
  126. R. C. Buchanan, Ceramic Materials for Electronics, Marcel Dekker Inc. New York, (1991) 35.
  127. Y. P. Fu, K. Y. Pan, C. H. Lin, Mat. Lett. 57 (2002) 291.
  128. S. H. Vajargah, H. R. M. Hosseini, Z. A. Nemati, J. All. Compds. 430 (2007) 339.
  129. K. H. Wu, W. C. Huang, J. Solid State Chem. 177 (2004) 3052.
  130. N. S. Gajbhiye, U. Bhattacharya, V. S. Darshane, Thermochim. Acta. 264 (1995) 219.
  131. A. Chakraborty, P. S. Devi, H. S. Maiti, Mat. Lett. 20 (1994) 63.
  132. P. Yadoji, R. Peelamedu, D. Agrawal, R. Roy, Mat. Sci. Engg. B 98 (2003) 269.
  133. C. R. Foschini, L. Perazolli, J. A. Varela, J. Mat. Sci. 39 (2004) 5825.
  134. R. Valenzuela, 'Magnetic Ceramics', National University of Mexico (1994).

135. Y. Bai, J. Shou, Z. Gui, Z. Yue, L. Li, *J. Magn. Magn. Mater.* 264 (2003) 44.
136. L. Neel, *Physica* 15 (1949) 225.
137. A. Znidarsic, M. Drofenik, *IEEE Trans. Magn.* 32 (3) (1996) 1941.
138. Ž. Cvejić, S. Rakić, S. Jankov, S. Skuban, A. Kapor, *Processing and Application of Ceramics* 2 (1) (2008) 53.
139. H. Su, H. Zhang, X. Tang, B. Liu, Z. Zhong, *J. All. Compds.* (2008) (Accepted).
140. E. W. Gorter, *Philips Res. Rep.* 9 (1954) 295.
141. [http://www.ing.unitn.it/\\_maud](http://www.ing.unitn.it/_maud).
142. B. D. Cullity, *Introduction of Magnetic Materials*, Addison-Wesley Publishing Company, Indiana (1972).
143. J. F. Wang, C. B. Ponton, R. Grossinger, I. R. Harris, *J. All. Compds.* 369 (2004) 170.
144. S. F. Wang, Y. R. Wang, T. C. K. Yang, P. J. Wang, C. A. Lu, *J. Magn. Magn. Mater.* 217 (2000) 35.
145. M. Pal, P. Brahma, D. Chakravorty, *J. Magn. Magn. Mater.* 152 (1996) 370.
146. R. M. German, *Sintering Theory and Practice*, John Wiley & Sons, Inc. (1996) 225.

## *Publications resulting from the Ph. D. Work*

---

- 1) **P. K. Roy**, J. Bera, “*Effect of Mg substitution on electromagnetic properties of  $(Ni_{0.25}Cu_{0.20}Zn_{0.55})Fe_2O_4$  Ferrite prepared by auto combustion method*”, **Journal of Magnetism and Magnetic Materials** 298 (1) (2006) 38-42.
- 2) **P. K. Roy**, J. Bera, “*Enhancement of the magnetic properties of Ni-Cu-Zn ferrites with the substitution of small fraction lanthanum for iron*”, **Materials Research Bulletin** 42 (2007) 77–83.
- 3) **P. K. Roy**, J. Bera, “*Characterization of nanocrystalline Ni-Cu-Zn ferrite powders synthesized by sol-gel auto-combustion method*”, **Journal of Materials Processing Technology** 197 (2008) 279–283.
- 4) **P. K. Roy**, B. B. Nayak, J. Bera, “*Study on electro-magnetic properties of La substituted Ni-Cu-Zn ferrite synthesized by auto-combustion method*”, **Journal of Magnetism and Magnetic Materials** 320 (2008) 1128–1132.
- 5) **P. K. Roy**, J. Bera, “*Electromagnetic properties of samarium substituted Ni-Cu-Zn ferrite prepared by auto combustion method*”, **Journal of Magnetism and Magnetic Materials** 321 (4) (2009) 247-251.
- 6) **P. K. Roy**, J. Bera, “*Effect of  $Bi_2O_3$ ,  $V_2O_5$ , and  $MoO_3$  addition on densification behaviors and electro-magnetic properties of  $(Ni_{0.25}Cu_{0.20}Zn_{0.55})Fe_2O_4$  Ferrite*” (To be communicated).

## *Research Presentation*

---

- 1) **P. K. Roy**, J. Bera, “*Preparation and characterization of Mg-Cu-Zn ferrite nanocrystalline powder by auto-combustion of nitrate-citrate gels.*” A National Level Student’s Technical Symposium (Confluence 2K4) during 10-11<sup>th</sup> Jan 2004 at NIT Rourkela, Rourkela, INDIA.
- 2) **P. K. Roy**, J. Bera, “*Synthesis and electromagnetic properties of La substituted Ni-Cu-Zn ferrite prepared by auto combustion method.*” Indo–Singapore

Symposium on Advanced Functional Materials (AFMS-06) during 24-26<sup>th</sup> February 2006 at IIT Bombay, Mumbai, INDIA.

- 3) J. Bera, **P. K. Roy**, “*Micro-structural Characterization of La Substituted Ni-Cu-Zn Ferrites Prepared by Auto-Combustion Method*” National Seminar on Advances in Electro-ceramics (NASE-2006) during 5-6<sup>th</sup> may 2006 at DRDO, Pune, INDIA.
- 4) **P. K. Roy**, J. Bera, “*Enhancement of the Properties of Mg substituted nanocrystallite Ni-Cu-Zn Ferrite prepared by auto combustion method*” National Seminar on Advances in Electro-ceramics (NASE-2006) during 5-6<sup>th</sup> may 2006 at DRDO, Pune, INDIA.
- 5) **P. K. Roy**, J. Bera, “*Effect of Zn addition on electro-magnetic properties of nanocrystalline Ni-Cu-Zn ferrite powders by sol-gel auto-combustion method.*” International Symposium for Research Scholars on Metallurgy, Materials Science & Engineering (ISRS-2006) during 18-20 Dec 2006 at IIT Madras, Chennai, INDIA.

## Curriculum Vitae

### **Pradip Kumar Roy**

S/O Mr. Bechu Ram Roy,

Village & P.O.- Sunur, District-Burdwan, W.B.-713125, INDIA.

**Phone No:** +91-342-2323453 (R), +91-9969460580 (M)

**Email:** pradip.nitrkl@gmail.com



**Date of Birth:** 19.07.1980

**Education:** Ph.D. (Submitting), B. Tech. (Ceramic Engg.)

**Research Interest:** Magnetic Ceramic, Ferroelectric Relaxor Ceramic, Electro-Ceramic, Bio-Ceramic, Refractory.

**Technical Exposure:** Publication: **8**, Patent: **5**, Conference: **13**

**Work Experience:** Presently working as a **Deputy Manager-Technology** in R&D at Crompton Greaves Ltd. Mumbai from 5<sup>th</sup> march 2007 onwards.

### **Publications:**

- 1) **P. K. Roy**, J. Bera, “*Formation of SrTiO<sub>3</sub> from Sr-oxalate and TiO<sub>2</sub>*”, **Materials Research Bulletin** 40 (2005) 599-604.
- 2) J. Bera, **P. K. Roy**, “*Effect of Grain Size on Electromagnetic Properties of (Ni<sub>0.7</sub>Zn<sub>0.3</sub>)Fe<sub>2</sub>O<sub>4</sub> Ferrite*”, **Physica B** 363 (2005) 128-132.
- 3) **P. K. Roy**, J. Bera, “*Effect of Mg substitution on electromagnetic properties of (Ni<sub>0.25</sub>Cu<sub>0.20</sub>Zn<sub>0.55</sub>)Fe<sub>2</sub>O<sub>4</sub> Ferrite prepared by auto combustion method*”, **Journal of Magnetism and Magnetic Materials** 298 (1) (2006) 38-42.
- 4) **P. K. Roy**, J. Bera, “*Enhancement of the magnetic properties of Ni-Cu-Zn ferrites with the substitution of small fraction lanthanum for iron*”, **Materials Research Bulletin** 42 (2007) 77-83.
- 5) **P. K. Roy**, J. Bera, “*Characterization of nanocrystalline Ni-Cu-Zn ferrite powders synthesized by sol-gel auto-combustion method*”, **Journal of Materials Processing Technology** 197 (2008) 279-283.
- 6) **P. K. Roy**, B. B. Nayak, J. Bera, “*Study on electro-magnetic properties of La substituted Ni-Cu-Zn ferrite synthesized by auto-combustion method*”, **Journal of Magnetism and Magnetic Materials** 320 (2008) 1128-1132.
- 7) **P. K. Roy**, J. Bera, “*Electromagnetic properties of samarium substituted Ni-Cu-Zn ferrite prepared by auto combustion method*”, **Journal of Magnetism and Magnetic Materials** 321 (4) (2009) 247-251.
- 8) **P. K. Roy**, V. Singal, “*Synthesis & Characterization of Combustion Synthesized Nano ZnO Powders for Varistor Ceramics*”, **Materials Characterization** (Communicated).

### **Professional Membership:**

- Studentship member of Indian Ceramic Society [M. No. ES 181].
- Life time member of Materials Research Society of India (MRSI) [M No. LMB 882].